THESIS FOR THE DEGREE OF DOCTOR OF PHILOSOPHY

Effects of Gamma Radiation and Gamma-Induced Species on Water Chemistry, Polymers and Fe-, Ni- and Zr-Based Alloys

Luca Gagliani

Department of Chemistry and Chemical Engineering

CHALMERS UNIVERSITY OF TECHNOLOGY

Department of Chemistry

School of Engineering Sciences in Chemistry, Biotechnology and Health

KTH ROYAL INSTITUTE OF TECHNOLOGY

Gothenburg, Sweden 2026

Effects of Gamma Radiation and Gamma-Induced Species on Water Chemistry, Polymers and Fe-, Ni- and Zr-Based Alloys

Luca Gagliani

© Luca GAGLIANI, 2026
ISBN: 978-91-8103-473-8

Doktorsavhandlingar vid Chalmers Tekniska Högskola och Kungliga Tekniska Högskola
TRITA-CBH-FOU-2026:37
Ny serie nr: 5930
ISSN: 0346-718X
DOI: https://doi.org/10.63959/chalmers.dt/5930

Department of Chemistry and Chemical Engineering
Chalmers University of Technology
SE-412 96 Gothenburg
Sweden
Telephone: +046 (0)31-772 1000

Cover:
Chrono amperometry measurements of AISI 316L steel in 0.15 mM H_2O_2, 0.125 M Na_2SO_4 electrolytic solution under intermittent γ irradiation at different dose rates. From top to bottom: 0.25 Gy/s (blue), 0.46 Gy/s (red) and 0.57 Gy/s (green).

Printed by:
Chalmers Digitaltryck
Gothenburg, Sweden 2026

Effects of Gamma Radiation and Gamma-Induced Species on Water Chemistry, Polymers and Fe-, Ni- and Zr-Based Alloys

Luca Gagliani

Department of Chemistry and Chemical Engineering - Chalmers University of Technology
Department of Chemistry, School of Engineering Sciences in Chemistry, Biotechnology and Health - KTH Royal Institute of Technology

Abstract

Nuclear energy is expected to play an important role in the transition toward low-carbon energy systems. Light Water Reactors (LWRs) dominate the global nuclear fleet, and their safe, reliable, and long-term operation depends on understanding the interactions between radiation, water chemistry, and structural materials that govern corrosion and material degradation.
This thesis investigates the effects of direct gamma irradiation and gamma-induced radiolysis on polymers, aqueous systems, and metallic alloys relevant to LWR operation. Particular attention is given to hydrogen peroxide and other reactive species produced during water radiolysis and their interactions with materials commonly present in reactor systems and laboratory irradiation experiments. The results demonstrate that material interfaces strongly influence the chemistry of irradiated aqueous systems. Investigations of polymer sealing materials revealed that hydrogen peroxide accumulation depends significantly on material choice, highlighting how experimental design and material selection can affect radiation chemistry measurements and contribute to reproducibility challenges. Studies of reactor-relevant alloys further showed that hydrogen peroxide accumulation depends on alloy composition and is governed primarily by radiation-induced processes in solution. Surface analyses indicated only minor modifications of oxide films during irradiation, suggesting that changes in water chemistry are linked more closely to species released into solution than to extensive alterations of alloy surfaces under the investigated conditions. In situ electrochemical measurements under intermittent gamma irradiation revealed an immediate dose-rate-dependent response associated with radiolytically generated reactive species. The results distinguished the roles of short-lived radicals and longer-lived oxidants, identifying hydrogen peroxide as the primary driver of the longer-term electrochemical evolution of the investigated alloy surface. Overall, this thesis shows that the behaviour of irradiated aqueous systems is governed by the interplay between radiation, water chemistry, and material interfaces. The findings contribute to a deeper understanding of radiation chemistry and corrosion-related phenomena in LWR environments and provide guidance for the design and interpretation of future irradiation experiments.

Keywords: Gamma radiation, Hydrogen peroxide, Polymer degradation, Electrochemistry, Radiolysis

Effects of Gamma Radiation and Gamma-Induced Species on Water Chemistry, Polymers and Fe-, Ni- and Zr-Based Alloys

Luca Gagliani

Department of Chemistry and Chemical Engineering - Chalmers University of Technology
Department of Chemistry, School of Engineering Sciences in Chemistry, Biotechnology and Health - KTH Royal Institute of Technology

Sammanfattning

Kärnenergi förväntas spela en viktig roll i omställningen till energisystem med låga koldioxidutsläpp. Lättvattenreaktorer (Light Water Reactors, LWR) dominerar den globala kärnkraftsflottan, och deras säkra, tillförlitliga och långsiktiga drift är beroende av en god förståelse av de interaktioner mellan strålning, vattenkemi och konstruktionsmaterial som styr korrosion och materialdegradering. Denna avhandling undersöker effekterna av direkt gammastrålning och gammastrålningsinducerad radiolys på polymerer, vattenbaserade system och metalliska legeringar som är relevanta för drift av lättvattenreaktorer. Särskild uppmärksamhet ägnas åt väteperoxid och andra reaktiva specier som bildas vid vattenradiolys samt deras interaktioner med material som vanligtvis förekommer i reaktorsystem och i laboratoriebaserade bestrålningsexperiment. Resultaten visar att materialgränsytor har ett starkt inflytande på kemin i bestrålade vattenbaserade system. Studier av polymera tätningsmaterial visade att ackumuleringen av väteperoxid i hög grad beror på materialvalet, vilket belyser hur experimentell utformning och materialval kan påverka mätningar inom strålningskemi och bidra till utmaningar kopplade till reproducerbarhet. Undersökningar av reaktorrelevanta legeringar visade vidare att ackumuleringen av väteperoxid beror på legeringens sammansättning och i huvudsak styrs av strålningsinducerade processer i lösningen. Ytanalyser indikerade endast mindre förändringar i oxidfilmerna under bestrålning, vilket tyder på att förändringar i vattenkemin är närmare kopplade till arter som frigörs till lösningen än till omfattande förändringar av legeringsytorna under de undersökta förhållandena. Elektrokemiska in situ-mätningar under intermittent gammastrålning visade en omedelbar dosrathastighetsberoende respons associerad med radiolytiskt genererade reaktiva specier. Resultaten särskilde rollerna hos kortlivade radikaler och mer långlivade oxidationsmedel och identifierade väteperoxid som den huvudsakliga drivkraften bakom den långsiktiga elektrokemiska utvecklingen hos den undersökta legeringsytan. Sammanfattningsvis visar denna avhandling att beteendet hos bestrålade vattenbaserade system styrs av samspelet mellan strålning, vattenkemi och materialgränsytor. Resultaten bidrar till en djupare förståelse av strålningskemiska och korrosionsrelaterade fenomen i lättvattenreaktormiljöer samt ger vägledning för utformning och tolkning av framtida bestrålningsexperiment.

Nyckelord: Gammastrålning, Väteperoxid, Polymernedbrytning, Elektrokemi, Radiolys.

List of Publications and Manuscripts

This thesis is based on the following papers and manuscripts:

Paper I

L. Gagliani, C. Ekberg, M. Jonsson "How Septum Materials Affect H_2O_2 Accumulation under Gamma-Irradiation of Water in Sealed Vials: A Comparative Study on Polysiloxane Rubber, PTFE, and Aluminum", Radiation Physics and Chemistry, 238, 1 2026.

Contribution: Main author, conceptualization, experimental work and analysis of data.

Paper II

L. Gagliani, C. Ekberg, M. Jonsson, "Study of H_2O_2 Production and Consumption in γ-Irradiated Aqueous Systems in Contact with Zircaloy, Inconel, and AISI Alloys. An Electrochemical Approach", The 23rd International Conference on Water Chemistry in Nuclear Reactor Systems (NPC 2025), Paper 1279, September 2025, Busan, South Korea.

Contribution: Main author, conceptualization, experimental work and analysis of data.

Paper III (Submitted)

L. Gagliani, F. Petersson, C. Ekberg, M. Jonsson, "Impact of Alloy Composition on the Steady-State Concentration of Hydrogen Peroxide in Water under Gamma Irradiation", Journal of Nuclear Materials, 2026.

Contribution: Main author, conceptualization, experimental work and analysis of data.

Paper IV (Submitted)

L. Gagliani, C. Ekberg, M. Jonsson, "In Situ Electrochemical Investigation of 316L Alloy under Intermittent Gamma Irradiation in Water Solutions – Direct Assessment of the Relative Impact of Radiolytic Oxidants", Radiation Physics and Chemistry, 2026.

Contribution: Main author, conceptualization, experimental work and analysis of data.

List of abbreviations

The following abbreviations are used throughout the thesis.

AI	Artificial Intelligence
AISI	American Iron and Steel Institute
ASTM	ASTM International
BWR	Boiling Water Reactor
CA	Chronoamperometry
CAD	Computer-Aided Design
CE	Counter Electrode
CILC	CRUD-Induced Localized Corrosion
CIPS	CRUD-Induced Power Shift
CPE	Constant Phase Element
CRUD	Chalk River Unidentified Deposits
DC	Direct Current
EC	Electrochemical
EIS	Electrochemical Impedance Spectroscopy
FDM	Fused Deposition Modeling
FFT	Fast Fourier Transform
FP	Fission Product
GCR	Gas-Cooled Reactor
HWR	Heavy Water Reactor
IAEA	International Atomic Energy Agency
ICP-MS	Inductively Coupled Plasma Mass Spectrometry
LET	Linear Energy Transfer
LSV	Linear Sweep Voltammetry
LWR	Light Water Reactor
MOX	Mixed Oxide Fuel
NPP	Nuclear Power Plant
NRC	Nuclear Regulatory Commission
OCP	Open Circuit Potential
PEEK	Polyether Ether Ketone
PIB	Polyisobutylene
PMMA	Polymethyl Methacrylate
PTFE	Polytetrafluoroethylene
PWR	Pressurized Water Reactor
PWSCC	Primary Water Stress Corrosion Cracking
RE	Reference Electrode
RPV	Reactor Pressure Vessel
SCE	Saturated Calomel Electrode
SDG	Sustainable Development Goal
SEM	Scanning Electron Microscopy
UK	United Kingdom
UNS	Unified Numbering System
WE	Working Electrode
XPS	X-ray Photoelectron Spectroscopy

Table of Contents

1 Introduction 1

2 Background 5

2.1 Light Water Reactor (LWR) Systems 5

2.1.1 Pressurized Water Reactor (PWR) 5

2.1.2 Boiling Water Reactor (BWR) 6

2.2 Radiolysis of Water and Chemistry of Water in LWRs 7

2.3 Consequences of Water Radiolysis in LWRs 9

2.4 Effect of γ Irradiation on Polymers 10

3 Methods 13

3.1 The Triiodide (Ghormley) Method 13

3.2 Fundamentals of Electrochemistry 13

3.2.1 Electrochemical Analysis Techniques 14

3.2.1.1 Open Circuit Potential 14

3.2.1.2 Linear Voltammetry 15

3.2.1.3 Potentiostatic Amperometry (Chronoamperometry) 16

3.2.1.4 Electrochemical Impedance Spectroscopy 16

3.2.1.4.1 EIS Data Representation 17

3.2.1.4.2 Surface Oxide Thickness Calculation from EIS Data 18

4 Experimental 21

4.1 Materials 21

4.1.1 Alloys 21

4.1.2 Containers for Irradiation and Hydrogen Peroxide Reactivity Studies 22

4.1.3 Solutions for Irradiation and Hydrogen Peroxide Reactivity Studies 22

4.2 Setup for γ Irradiation 22

4.3 H_2O_2 Concentration Measurements 23

4.4 Electrochemical Setup and Parameters 24

4.4.1 Electrolytic Solutions 24

4.4.2 Radiation-Resistant Reference Electrode 24

4.4.3 Counter Electrode 26

4.4.4 Radiation Resistant Electrochemical Cell 26

5 Results and Discussion 29

5.1 Impact of Septum Materials on the Accumulation of Hydrogen Peroxide under γ Irradiation of Sealed Vials 29
5.1.1 Accumulation of Hydrogen Peroxide under γ Irradiation 29
5.2 Impact of Alloy Composition on the Steady-State Concentration of Hydrogen Peroxide under γ Irradiation in Water 35
5.2.1 Hydrogen Peroxide Accumulation under γ Irradiation 35
5.2.2 Influence of Pre-Oxidation on Hydrogen Peroxide Accumulation under γ Irradiation 36
5.2.3 Hydrogen Peroxide Reactivity towards Alloys in Normal Conditions 37
5.2.4 Surface Investigation after Irradiation and Exposure to Hydrogen Peroxide 38
5.2.4.1 Scanning Electron Microscopy 38
5.2.4.2 X-Ray Photoelectron Spectroscopy 40
5.2.4.3 Electrochemical Impedance Spectroscopy 44
5.2.4.4 Analysis of Metal Ions in the Aqueous Phase 47
5.3 In-Situ Electrochemical Investigation of 316L in Water Solutions under Intermittent γ Irradiation 50
5.3.1 Oxidative Response under Intermittent γ Irradiation at Different Dose-Rates 50
5.3.2 Effect of Intermittent γ Irradiation on Hydrogen Peroxide Build-up and Corrosion Potential 54
5.3.3 Surface Modification after γ Irradiation and Hydrogen Peroxide Addition 59
6 Conclusion 65
Acknowledgements 67
References 69
Appendix A – Surface Investigation Techniques 79
Scanning Electron Microscopy 79
X-ray Photoelectron Spectroscopy 79
Appendix B – Solubilised Elements Investigation 81
Inductively Coupled Plasma Mass Spectroscopy 81

1 Introduction

The accelerating impact of climate change, including rising global temperatures, increased frequency of extreme weather events, and the continued melting of ice caps, have intensified international efforts to decarbonize energy systems which still rely heavily on fossil fuels[1]. In parallel, global electricity demand rises at its fastest pace, as a result of economic development, digitalization and the electrification of transport and industry [2]. Latest figures calculate a year-on-year electricity demand growth close to 4%[2]. Recently, the United Nations shared in reports that AI alone accounts for 1.5% of the world energy demand and it may double before 2030, producing emissions comparable to a medium-size industrialized country such as the UK[3]. Within this context, nuclear power remains a fundamental low-carbon electricity source with a total of 417 operating plants worldwide[4], offering reliable electricity production that can complement intermittent renewable energy sources in support of long-term decarbonization objectives[5].

Sweden is undergoing a similar transition. The country's electricity system is expected to face substantial growth in demand over the coming decades, driven in particular by industrial electrification and broader societal transformation. Recent projections indicate that Swedish industrial electricity demand alone may increase by 88 TWh by 2035[6]. Such a demand cannot be satisfied by renewables alone and, in 2023, Sweden changed its target of producing 100% renewable energy by 2040 with the target of becoming 100% fossil-free. While Vattenfall, owner of the existing nuclear facilities in Ringhals and Forsmark, have announced ambitions to extend reactor operation to 80 years[7], the government has manifested the will of building new nuclear capacity, in the form of both multiple small modular reactors and large units, with a national objective of bringing the equivalent of two large-scale reactors online by 2035 and up to ten new reactors by 2045[8], [9]. Since the entry into force of the new state-aid act in August 2025[10], [11], several companies have applied for building permits and financial support, indicating that nuclear power will continue to play a central role in Sweden's future electricity supply[9].

The long-term operation of nuclear power plants relies on the structural integrity and performance of materials exposed to some of the most demanding environments encountered in engineered systems. Throughout decades of service, reactor components are subjected to elevated temperatures, high pressures, intense radiation fields, and chemically reactive aqueous environments. In light-water reactors, materials in contact with the primary coolant typically experience temperatures approaching 350 °C, pressures up to 16 MPa, and continuous exposure to neutron and gamma radiation. Moreover, the continuous recirculation of water, together with steam flows and boiling contributes further to corrosion, deformations and vibrations as well. Under these conditions, interactions occur between the coolant, the radiation field, and structural materials, influencing both the degradation of materials and the transport of corrosion products throughout the system.

Among the most important consequences of ionizing radiation in water-cooled reactors is the radiolysis of water. The interaction between radiation and water generates a wide range of highly reactive transient and molecular species, including hydrated electrons (e_{aq}^-), hydrogen

atoms (H•), hydroxyl radicals (HO•), hydrogen peroxide (H_2O_2), molecular hydrogen (H_2), and oxygen (O_2). The concentrations of these species depend strongly on the radiation field (dose rate and linear energy transfer), temperature, pressure, and water chemistry. Their intrinsic reactivities (rate constants) are mainly temperature-dependent, but the overall impact of radiolysis on corrosion is governed by the steady-state concentrations of the reactive species under given reactor conditions.Radiolytic products alter the local chemical and electrochemical environment at metal surfaces and can significantly affect corrosion kinetics, oxide stability, elemental dissolution, and the speciation, and thereby transport and deposition of corrosion products throughout the reactor coolant circuit by changing oxidation states and solubilities of metal ions and coupling with mass-transport processes.

The interaction between radiolysis products and structural alloys is particularly important because corrosion-related phenomena remain among the principal degradation mechanisms affecting nuclear systems. Materials commonly employed in reactor environments, such as zirconium alloys, nickel-based alloys, stainless steels, and chromium-rich corrosion-resistant materials, can undergo significant modifications of their surface oxides and corrosion behaviour when exposed to radiation-induced oxidizing species. Understanding the mechanisms governing these interfacial reactions is therefore essential for predicting material performance, optimizing water chemistry strategies, mitigating dose build-up, and supporting lifetime extension programmes for existing nuclear reactors.

Despite decades of research, experimental investigations of radiation-assisted corrosion remain challenging. Access to irradiation facilities is limited, experiments are time-consuming and costly, and the simultaneous influence of temperature, pressure, water chemistry, irradiation, and material composition complicates the interpretation of results[12], [13]. Consequently, significant interest has emerged in the development of laboratory-scale methodologies capable of reproducing key radiation-induced effects without requiring continuous irradiation[12], [14]. Such approaches facilitate mechanistic studies and accelerate materials testing while substantially reducing experimental complexity and cost.

Among the various species generated during water radiolysis, hydrogen peroxide has frequently been employed as a chemical surrogate for radiolysis owing to its relative stability and strong oxidizing character. Corrosion studies have therefore used H_2O_2 additions to simulate irradiated environments[15], [16]. However, the extent to which hydrogen peroxide alone can reproduce the behaviour observed under actual irradiation remains an open scientific question. Unlike chemically added H_2O_2, which introduces a single oxidant, γ-irradiation continuously generates both oxidizing and reducing radiolysis products in water. These species react with each other and with the surface through multiple coupled pathways, leading to time and dose rate-dependent interfacial chemistry. In particular, transient species such as hydroxyl radicals may participate directly in surface reactions affecting passive film stability, localized dissolution and redox or catalytic reaction at the alloy surface. As a result, the representativeness of H_2O_2-only testing for predicting corrosion processes in nuclear reactor environments remains insufficiently established, with discrepancies between simulated and actual irradiation conditions[17].

The aim of this work is to investigate whether it is feasible to accurately reproduce, on a laboratory scale and without irradiation, the same conditions and effects on selected alloys as those in an actual reactor environment by focusing on the γ-induced radiolysis vs H_2O_2 effect on planar specimens. Given the multitude of variables at play, extensive investigations are indispensable to establish a firm basis for consistent, reliable, and reproducible outcomes. Accordingly, the materials, methods, and equipment employed are systematically examined with the aim of developing a robust experimental procedure aligned with the project's objectives. This is of critical importance because radiation influences not only the samples, encompassing both liquid and solid phases subjected to irradiation, but also the containers and ancillary equipment, making it essential to disentangle their respective contributions. By probing the interplay between γ-irradiation, γ-induced radiolysis and H_2O_2 effects on surfaces, this project yields insights into how different materials are affected by gamma radiation and, reciprocally, how they shape the chemistry of water radiolysis.

The present research contributes to the achievement of the United Nations Sustainable Development Goals, most notably SDG 6 (Clean Water and Sanitation), SDG 7 (Affordable and Clean Energy), SDG 9 (Industry, Innovation and Infrastructure), and SDG 13 (Climate Action). Through the investigation of radiation-induced processes and the development of experimental methodologies for their simulation, this work supports the safe operation, lifetime extension, and future deployment of nuclear power plants. As nuclear energy constitutes an important low-carbon component of the global electricity mix, enhanced understanding of material degradation mechanisms contributes to maintaining reliable electricity production while supporting long-term decarbonization and climate-mitigation objectives. In addition, improved knowledge of material degradation and plant safety contributes to minimizing the risk of accidental release of radioactive contaminants into aquatic environments. The research also indirectly supports future applications of nuclear energy for large-scale desalination, which may contribute to improving access to freshwater in water-stressed regions.

2 Background

2.1 Light Water Reactor (LWR) Systems

Light Water Reactors (LWRs) represent the most widely deployed type of nuclear reactor for energy production worldwide. According to the International Atomic Energy Agency (IAEA), at the time of writing this thesis, 360 of the 417 operational nuclear reactors globally are LWRs, of which 308 are Pressurized Water Reactors (PWRs) and 45 are Boiling Water Reactors (BWRs)[18]. In Sweden, six reactors are currently in operation: two PWRs at the Ringhals Nuclear Power Plant (NPP), and four BWRs at the Forsmark and Oskarshamn sites[19], [20], [21]. In contrast to other reactor types, such as Heavy Water Reactors (HWRs) and Gas-Cooled Reactors (GCRs), LWRs utilize ordinary water (H_2O) simultaneously as coolant and neutron moderator. Their relative simplicity, favourable fuel availability, and well-established coolant chemistry have contributed to their widespread adoption. The first LWR constructed for civilian power generation was Westinghouse's PWR at Shippingport, which commenced operation in 1957, followed by General Electric's Dresden-1, the first operational BWR, in 1960. As of now, 70 more LWRs (67 PWRs and 3 BWRs) are under construction wordwide[18].

LWRs operate on the working principle of nuclear fission, where a fissile solid fuel in the form of pellets (generally uranium oxide, UO_2 or mixed-oxide fuel, MOX) is loaded in zirconium alloy rods spaced by metallic spacers and surrounded by coolant, i.e., water. Only a relatively small fraction of the fuel is fissile (i.e, can split into two smaller elements upon being hit by a thermal neutron), with the majority being fissionable (i.e., can only be split by fast neutrons or absorb a neutron and convert into a fissile one such as U^{238} becoming Pu^{239}). Upon thermal neutron collision, the fissile nuclide can split into two (or more) fragments, called fission products (FPs), releasing an average of 2 to 3 neutrons and energy in the form of heat, as in the example reaction given in **Equation 1**.

Equation 1: $$n_0^1 + U_{92}^{235} \rightarrow Te_{52}^{132} + Zr_{40}^{101} + 3n_0^1 + heat$$

The water surrounding each fuel rod and interposing between them will hence collect the produced heat and moderate (i.e., slow down) the released neutrons, which will eventually lead to further fission events or breed more fissile fuel from fissionable nuclei. The hot water will then indirectly (e.g., PWRs) or directly (e.g., BWR) activate steam turbines to convert the heat into electricity. In the subchapters below, a brief explanation of the differences between BWR and PWR will follow.

2.1.1 Pressurized Water Reactor (PWR)

In a Pressurized Water Reactor (PWR), the coolant in the closed primary circuit (i.e., the reactor core, reactor pressure vessel (RPV), primary piping, and steam generator tubes) is maintained in the liquid phase throughout normal operation. To prevent bulk boiling at the elevated coolant temperatures encountered during power operation (typically in the range of 320-350 °C), the primary system is operated at pressures of approximately 150-160 bar[22]. Neutron moderation is provided by the light water coolant itself, while reactivity control is achieved through a combination of soluble neutron absorber (boric acid, H_3BO_3, dissolved in the primary coolant)

and solid control rods, which in PWRs are inserted from the top of the RPV. The heated primary coolant is circulated by reactor coolant pumps to the steam generators, where thermal energy is transferred across tube walls to a secondary water circuit that is permitted to boil and generate steam for the turbine–generator set. As illustrated in **Figure 1**, the primary coolant is then returned to the RPV, completing the loop. This two-circuit configuration confines activated corrosion products and other radionuclides to the primary circuit, thereby maintaining a radioactivity-free secondary system and turbine hall under normal operating conditions.

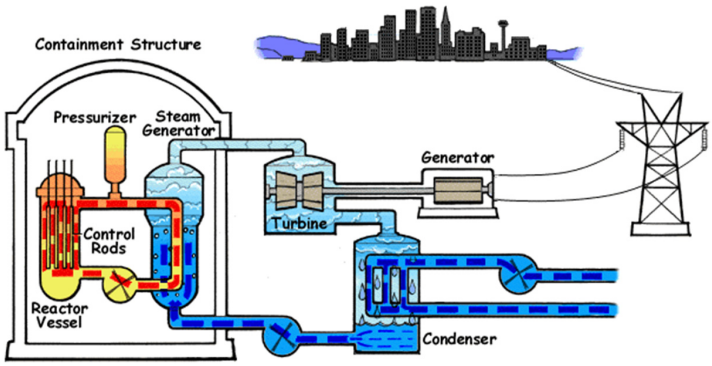


Figure 1: Schematic representation of a PWR reactor and its main constituents, from the U.S. NRC website [23].

2.1.2 Boiling Water Reactor (BWR)

In a Boiling Water Reactor (BWR), the primary coolant typically reaches temperatures in the range of 270-290 °C and is maintained at substantially lower pressures than in a PWR, on the order of 70 bar. These conditions permit bulk boiling within the reactor pressure vessel (RPV), so that the core is cooled by a two-phase mixture of liquid water and steam [22]. Short-term control of fission reactions is, in part, provided by changes in void fraction: as the power level and local heat generation increase, a larger fraction of the coolant is converted to steam, reducing the moderator density and thus the neutron moderation capability of the water. Early BWR designs employed an indirect cycle, in which steam generated in the RPV drove turbines via a secondary closed loop and heat exchangers, in a configuration somewhat analogous to PWRs. Such approach has since been abandoned in favour of direct-cycle designs. In modern BWRs, the steam produced in the RPV is dried and filtered, then expanded directly through the turbines before being condensed, purified, pre-heated and returned to the RPV as feedwater, as schematized in **Figure 2**. Because the steam entering the turbine originates directly from the reactor core, the risk of radioactive contamination/spill can be judged as sensibly greater than for PWRs, with short-lived activation products (e.g., N^{16}), being normally carried to the turbines hall, therefore contributing to higher radiation levels.

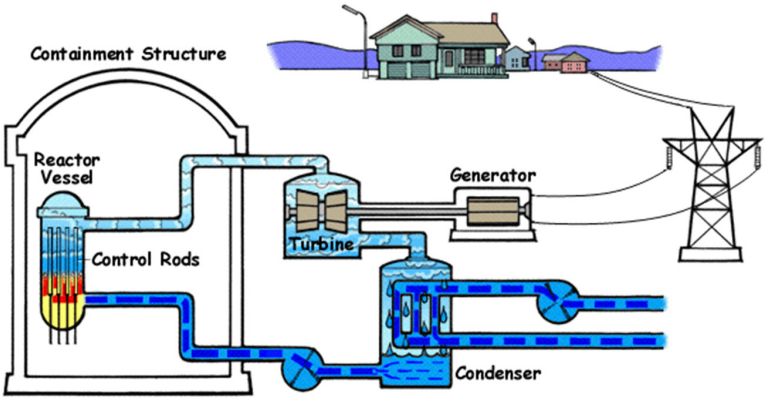


Figure 2: Schematic representation of a BWR reactor and its main constituents, from the U.S. NRC website[23].

The exception for the dual use of water as both coolant and moderator in BWRs is represented by the RBMK reactor units. Such a design was ideated in Russia, and several NPPs were built in the Soviet Union exclusively. The main design difference of RBMKs is that the moderation is provided by graphite bars and only the cooling of the core is done by water, which circulates in separate cooling channels.

2.2 Radiolysis of Water and Chemistry of Water in LWRs

Radiolysis of water consists in the decomposition of its molecules due to the interaction with ionising radiation. Ionising radiation, such as electrons, neutrons, X-rays, gamma- and alpha-radiation, can excite and ionise molecules along its path. The density of energy deposition along this path is quantified by the linear energy transfer (LET), defined as the average energy deposited per unit track length (typically in keV μm^{-1}). Low-LET radiation (e.g., gamma radiation, fast electrons) deposits energy sparsely, whereas high-LET radiation (e.g., α-particles, heavy ions) deposits it densely. In light-water reactors (LWRs), the dominant contributors to water radiolysis are gamma photons and neutrons. Owing to their limited range in water, alpha and beta particles can significantly contribute to radiolysis only in the immediate vicinity of their source, that is, in the event of direct fuel–coolant contact (e.g., following cladding failure or an incident) or through interactions between activated corrosion products and the coolant. As presented in **Figure 3**, the radiolytic event can be visualised in three stages, differentiated by the time scale[24].

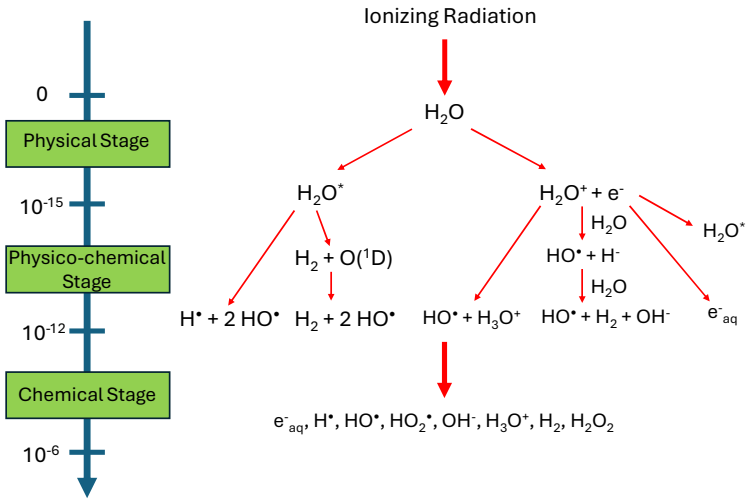


Figure 3: Main reactions involved in the radiolysis of water, Inspired by "Water Radiolysis: Influence of Oxide Surfaces on H_2 Production under Ionizing Radiation", S. Le Caër, 2011[25].

During the first stage (i.e., physical stage, 0-10^{-15}s) excited (H_2O^*) and ionized (H_2O^+) water molecules originate from the interaction with the ionizing radiation[24]. In the second stage (i.e., physicochemical stage, 10^{-15}-10^{-12}s) different processes such as ion-molecule reaction, dissociative relaxation, dissociation of excited states into ionic/radical fragments, , solvation of electrons and hole diffusion, (just to name a few) take place. The third stage (i.e., chemical stage, 10^{-12}-10^{-6}s) is characterized by the species reacting with each other within the tracks and/or with the surrounding molecules so far unaffected by the irradiation. Thus, the products in the tracks diffuse to the surroundings leading to further chemical reactions. For low-LET radiation, (i.e., γ-radiation) recombination's contribution is therefore irrelevant after 10^{-6}s.

The yields of water-radiolysis products have been extensively investigated and are known to depend on several factors, including the type and energy of the radiation, the elapsed time after the initial radiation event, solution pH, and the nature and concentration of dissolved solutes. Being most of the radiolysis products very reactive/unstable (e.g., radicals, solvated electrons), they will rapidly disappear. The primary oxidative radiolysis products in gamma-irradiated water are then hydrogen peroxide (H_2O_2), the hydroxyl radical (HO•) and to some extent also the hydroperoxyl radical (HOO•), even if in negligible quantities. Molecular oxygen (O_2) is subsequently formed as a secondary oxidative radiolysis product through reactions involving these primary radiolytic species.

Under continuous γ-irradiation, low but steady-state concentrations of hydrogen (H_2) and hydrogen peroxide (H_2O_2) are established because of a dynamic equilibrium between their radiolytic production and consumption. Their consumption occurs primarily through reactions with hydrogen (H•) and hydroxyl (HO•) radicals, as first described by Allen[26] and represented in **Equation 2** and **Equation 3**.

Equation 2: $HO\cdot + H_2 \rightarrow H_2O + H\cdot$

Equation 3: $H\cdot + H_2O_2 \rightarrow H_2O + HO$

As a matter of design, BWRs need very pure water to work flawlessly and avoid issues such as the buildup of deposits on the heat exchangers and turbine blades or selective corrosion phenomena. The principal impurities that may be introduced into the reactor feedwater, typically at trace levels, include iron, nickel, chromium, chloride, and silica. Consequently, stringent water chemistry control measures are implemented, including the use of ion-exchange systems to remove contaminants from the condensate stream. However, only dissolved species can be effectively removed, since suspended solids are generally deposited on the surfaces of the primary system. To protect the surfaces of the primary system from the uptake of contaminants and activated products (e.g., Co^{60}) and add some corrosion resistance, zinc and sometimes noble metals are added to the reactor core water [22].

On the other hand, PWRs require a more complex balance of additives in the coolant of the primary circuit. In fact, the moderation and control of the core activity is split between the control rods (for the short-term activity changes) and dissolved H_3BO_3 (for the long-term activity changes). While the addition of boric acid is necessary as a neutron moderator, this induces a lowering of the pH of the coolant, possibly causing both selective dissolution of elements from the RPV and the deposition of the same on the fuel rods in substantial amounts, with repercussions on the contamination build-up within the primary circuit. To balance the pH of the primary coolant, alkali agents such as lithium hydroxide (LiOH) and potassium hydroxide (KOH) are used. Over the years, evidence has been collected that operating PWRs at slightly basic pH values (i.e., pH 7.4) is beneficial for corrosion protection[22]. However, high pH values are again detrimental for the fuel assembly corrosion and primary water stress corrosion cracking (PWSCC), which seem to be accelerated by elevated Li^+ concentrations in the primary coolant. Since Li^7 is nevertheless produced in the primary coolant by neutron capture and subsequent alpha particle emission by B^{10}, it is preferred over potassium.

2.3 Consequences of Water Radiolysis in LWRs

During LWR operation, primary and therefore secondary products of water radiolysis will accumulate in the irradiated coolant. As listed in **2.2.**, the primary products more relevant from a corrosion point of view are the HO•, H_2 and H_2O_2 and O_2 as secondary product. Of these, in PWR systems, O_2 is regarded as the most dangerous since able to accelerate Zircaloy corrosion, followed by H_2O_2 (due to its major instability at high temperatures) and H_2. To contain dioxygen buildup, H_2 is injected into the primary coolant[27].

The maximum concentration of O_2 allowed in the primary coolant is usually 0.01 ppm, and a hydrogen-to-oxygen ratio of at least 240 (about 1 mg/kg) is required to maintain such a condition[22]. However, H_2 addition also brings drawbacks, and its concentration cannot exceed 4 mg/kg due to the risks associated with hydrogen uptake in the RPV, especially by the Zircaloy fuel cladding. Hydrogen uptake is known to induce alloy embrittlement and hence an increased risk of failures in the long term.

Similarly to PWRs, in BWRs dioxygen and dihydrogen are unwelcome products of water radiolysis. However, the different designs and cooling principles (i.e., liquid vs liquid + steam) lead to a different approach. The vigorous boiling of the primary coolant during operation tends to strip the water of the radiolytically produced gases, preventing their recombination and

hence extinguishing the formation of secondary products. Due to the partitioning of gases between liquid and steam, the latter contains up to 10^2 more O_2 and H_2, which are therefore transported to the turbines and the condenser. There, they will be recombined into water through a catalytic process. In addition, liquid-steam partitioning promotes the local enrichment and precipitation of corrosion products on fuel-cladding surfaces[28]. As these deposits accumulate and evolve into porous CRUD layers, neutron activation of incorporated nickel and cobalt species produces radionuclides such as Co^{60}, transforming the deposits into localized sources of elevated γ-radiation fields. The presence of CRUD on the fuel rods also acts as a thermal resistance layer, affecting the transfer of heat from the fuel to the primary coolant. These conditions further promote both precipitation (due to rapid solute concentration in microlayers) and adhesion of dissolved species.

Under high flux operation and especially during power maneuvers, localized boiling can happen also in PWR with analogous outcomes[29]. Moreover, the PWR coolant being rich in boron (as boric acid), boiling enriches boron in the microlayer close to the fuel rods, enabling boron incorporation within the CRUD. This is the origin of the axial CRUD-Induced Power Shift (CIPS) and CRUD-Induced Localized Corrosion (CILC), in which boron-rich crud locally depresses neutron flux and alters thermal-hydraulic fields, further reinforcing the conditions that promote crud deposition[30].

Hydrogen peroxide, which is an oxidant stronger than dioxygen (the Standard Reduction Potential vs SHE is +1.78 for H_2O_2 and +1.23 V for O_2[31]), is present in concentrations similar to dioxygen in the BWR coolant, despite the sampling systematically showing lower concentrations (and thus higher apparent O_2) due to the catalytic decomposition of the same along the sampling line[32]. However, in addition, dihydrogen is also injected into the coolant of BWRs as a further means to control the level of oxidants of peroxide.

2.4 Effect of γ Irradiation on Polymers

Since the early 1950s, it has been well-known by the scientific community that polymers undergo large changes in their physical properties when exposed to even relatively low doses of radiation[33], [34], [35], [36]. During irradiation, two main types of alterations take place: cross-linking and degradation. Both phenomena alter the molecular weight of the affected polymers and are propagated by the formation of radicals, driving further reactions[37]. The predominant type of degradation depends on factors such as polymer structure and irradiation conditions. As a rule of thumb, the polymers with a structure $-CH_2-CHR-$ (e.g., polyethylene, polystyrene and polyacrylonitrile) tend to be mostly affected by cross-linking. On the other hand, polymers containing quaternary carbons or labile side groups such as polyisobutylene (PIB), polymethylmethacrylate (PMMA) and polytetrafluoroethylene (PTFE) typically exhibit degradation commonly attributed to the higher stability of the radicals formed and the associated lower bond dissociation energies, which favour disproportionation and chain-scission reactions over cross-linking [38], [39], [40]. Both types of deterioration affect the mechanical strength of the materials.

During cross-linking, the average molecular weight of the polymeric chain increases due to the bonding of multiple polymeric chains, creating a three-dimensional network. Cross-linking

reduces the solubility of the polymeric chains and alters melting behaviour. As the cross-linked network grows, polymers reach a "gel point," beyond which they become insoluble. The dose required to achieve gel formation depends on the polymer's initial molecular weight and the cross-linking yield (i.e., the number of cross-links formed per 100 eV absorbed). During degradation, the molecular weight is reduced due to the scission of the polymeric chain. Factors like the polymer's initial molecular weight, the irradiation temperature and oxygen availability are particularly relevant for this type of deterioration. In this thesis two polymers have been investigated in particular: PTFE and polysiloxanes (silicone rubber).

Despite its thermal and chemical stability, PTFE degrades readily under ionizing radiation, releasing fluorinated gases (some of which are corrosive) and forming unsaturated fluorocarbon species. Radiation-induced chain scission generates radicals on the polymer backbone, which undergo β-scission and related reactions to produce volatile perfluorinated fragments and unsaturated structures such as –CF=CF– and –CF=CF_2 groups within the remaining polymer[41], [42]. The evolution of these reactive gases is linked to the breakdown of the polymer backbone and contributes to oxidative processes if oxygen is later introduced into the irradiated material.

Polysiloxanes, or silicones, exhibit notable cross-linking upon irradiation, with yields ranging from 2.5 to 4.5 cross-links per 100 eV absorbed[43], [44]. This cross-linking improves the mechanical strength and elasticity of silicone rubbers, which are widely used in radiation-rich environments[45], [46]. Unlike many organic polymers, polysiloxanes show little tendency to form unsaturated C=C structures or to undergo pronounced colour changes during irradiation, in part because of the high stability of their silicon–oxygen backbone and the different nature of the radiation-induced radicals.

Gaseous byproducts, including hydrogen, methane, and ethane, are released during the process[44], [47]. Additionally, polysiloxanes containing phenyl groups demonstrate enhanced radiation resistance compared to dimethyl-substituted silicones due to the stabilising effect of the aromatic rings[45], [46].

3 Methods

3.1 The Triiodide (Ghormley) Method

The triiodide method is a widely used analytical technique in radiation chemistry for detecting and quantifying hydrogen peroxide (H_2O_2), a radiolytic product formed during the irradiation of water and aqueous solutions, as presented in Chapter 2.2. This method leverages the reactivity of H_2O_2 with iodide ions (I^-) under acidic conditions to produce triiodide ions (I_3^-), which can be measured spectrophotometrically due to their distinct absorbance peak. The chemical reactions involved in the method are shown in **Equation 4** and **Equation 5**.

Equation 4: $$H_2O_2 + 2I^- + 2H^+ \rightleftharpoons I_2 + 2H_2O$$

Equation 5: $$I_2 + I^- \rightleftharpoons I_3^-$$

The triiodide ion (I_3^-), is characterized by a strong yellow-orange colour and by measuring the absorbance at a wavelength of 350 nm, the concentration of H_2O_2 can be accurately determined in accordance with Lambert-Beer's law for the correlation of the absorbance of a diluted solution with the concentration of the solute, as shown in **Equation 6**.

Equation 6: $$A = \mathcal{E} \cdot C \cdot l$$

Where A is the absorbance of the sample, $\mathcal{E}$ is the molar absorption coefficient, in $M^{-1}cm^{-1}$ and l is the optical path length.

3.2 Fundamentals of Electrochemistry

Electrochemical measurements are performed in an electrochemical cell. In a three-electrode configuration, the setup consists of the following main components:

- Working electrode (WE)
- Counter electrode (CE)
- Reference electrode (RE)
- Electrolyte
- Potentiostat

The sample under study serves as the working electrode, and its potential is measured or controlled with respect to the reference electrode. The reference electrode is typically Ag/AgCl (3 M KCl) or a saturated calomel electrode (SCE); its potential remains essentially constant under the experimental conditions (i.e., it behaves as a non-polarizable electrode).

The third electrode in this circuit is the counter electrode. It is usually made of an inert material with respect to the electrolyte in use, such as graphite or platinum, and its role is to close the circuit by supplying or accepting electrons to/from the working electrode. Reactions occurring at the working and counter electrodes involve oxidation and reduction, depending on the applied potential and the experimental conditions.

When the working electrode is polarized in the anodic direction (i.e., at a more positive potential than its open-circuit potential, OCP, whose measurement and meaning will be discussed in **Chapter 3.2.1.1**), oxidation reactions occur, releasing electrons that are transported to the counter electrode, where a cathodic reaction takes place. Conversely, if the working electrode is polarized in the cathodic direction (more negative than its OCP), reduction reactions occur at the working electrode, which accepts electrons from the counter electrode. The flow of electrons involved in these reactions constitutes an electrical current, which reflects the rate of the electrochemical process.

To close the circuit and allow current to flow, the three electrodes are immersed in an electrolytic solution. Dissolved ions enable conduction through ionic movement, while electrons do not travel through the bulk solution. These ions may act solely as charge carriers, or they may participate in chemical reactions at the electrode surfaces. Therefore, the choice of electrolyte must be made carefully to prevent, limit, or account for any bias that such side reactions may introduce into the measurements.

Potential and current can be monitored, recorded, and/or imposed using a potentiostat. This instrument can be operated in DC (direct current) or AC (alternating current) mode. In DC mode, the electrochemical response of the system is time-resolved: either the potential (e.g., linear voltammetry and chronopotentiometry) or the current (e.g., linear and cyclic amperometry, chronoamperometry) is recorded as a function of time, while the other variable (current or potential, respectively) is varied in steps, pulses, or sweeps. When an AC investigation is performed (e.g., electrochemical impedance spectroscopy, EIS), the electrochemical response is recorded as a function of frequency, which corresponds to the frequency of the small sinusoidal perturbation superimposed on the applied potential or current.

The specific electrodes, electrolytes, and potentiostatic techniques used in each experiment are detailed in the following sections.

3.2.1 Electrochemical Analysis Techniques

3.2.1.1 Open Circuit Potential

The open-circuit potential (OCP), also referred to as the corrosion potential or free potential, is a fundamental electrochemical parameter that provides insight into the equilibrium potential of a working electrode in the absence of any externally applied current. This unperturbed potential reflects the balance of electrochemical reactions occurring at the electrode–electrolyte interface.

The OCP is measured by immersing the working electrode in the electrolyte, allowing the system to stabilize, and recording the potential as a function of time versus the reference electrode. A stable OCP indicates that the system has reached a dynamic steady state (mixed-potential condition) in which the net current is zero, although individual anodic and cathodic reactions may still proceed. Under these conditions, the electrode/solution interface can be considered in a quasi-equilibrium with the solution and the gases dissolved in it.

The OCP is widely used to assess the corrosion behaviour of metals: a more negative OCP generally indicates a higher thermodynamic tendency for oxidation (and thus corrosion),

whereas a more positive OCP may suggest the formation of a protective film (e.g., passivation). By monitoring the OCP over time, the development of oxides, passivation layers, or corrosion at the electrode/electrolyte interface can be studied, as these processes shift the equilibrium state of the material due to the formation of a new surface in contact with the solution.

Factors such as the alloy composition, surface finish and roughness, and the pre-existence of an oxide layer may affect the measured OCP. In addition, the type of electrolyte (e.g., pH, presence of halide ions), the temperature, and the availability of oxygen can strongly influence the measurements. It is also crucial to allow the system to stabilize for a sufficient time before recording the OCP. Depending on the factors mentioned above, OCP stabilization may take from a few minutes up to several hours. The choice of an appropriate stabilization time before initiating new surface reactions (e.g., corrosion or oxide-layer formation) must therefore be carefully determined.

3.2.1.2 Linear Voltammetry

Linear sweep voltammetry (LSV) is an electrochemical technique used to study redox processes, electrochemical kinetics, and reaction mechanisms at electrode surfaces. In LSV, the potential of the working electrode is linearly swept with time at a fixed scan rate (in mV s^{-1}) from an initial potential to a final potential selected by the user. During the sweep, the current resulting from oxidation or reduction reactions at the working electrode surface is recorded. LSV experiments are typically initiated after the OCP has stabilized, starting the sweep from a potential close to the OCP

The current–potential response provides critical information about the electrochemical behaviour of the system, such as corrosion rates, passivation behaviour, oxidation and reduction reactions associated with changes in the material or in the electrolyte, and even catalytic activity. The recorded current is plotted as a function of the applied potential, yielding a voltammogram. When the current is recorded in a potential range close to the OCP and the logarithm of the absolute current is plotted vs the applied potential, the resulting Tafel plot is especially useful for the evaluation of corrosion rates.

As for OCP, factors such as surface roughness and cleanliness, material composition, temperature, and the type of electrolyte significantly affect the observed electrochemical response. In addition, the selected scan rate plays an important role: a faster scan rate can reveal kinetic limitations, whereas a slower scan rate allows the system to approach near-equilibrium conditions.

3.2.1.3 Potentiostatic Amperometry (Chronoamperometry)

In contrast to LSV, potentiostatic amperometry (or chronoamperometry, CA) involves holding the working electrode at a constant potential with respect to the reference electrode for the duration of the measurement, while the resulting current (typically associated with oxidation or reduction processes) is monitored as a function of time. This time-dependent current response provides information about electrode surface reactions, diffusion dynamics, and adsorption–desorption phenomena, as well as changes in electrolyte composition.

CA is commonly used to study corrosion inhibition mechanisms and passivation behaviour by observing how the current stabilizes or decays under constant-potential conditions. By analysing the current–time response, charge-transfer-limited and diffusion-limited processes can be distinguished, and surface adsorption or desorption of ions and molecules, as well as catalytic processes at the electrode surface, can be investigated. As with OCP and LSV, CA measurements are also sensitive to sample surface finish, electrolyte chemistry, and other experimental conditions.

3.2.1.4 Electrochemical Impedance Spectroscopy

Electrochemical Impedance Spectroscopy (EIS) is an AC technique in which a sinusoidal alternating current perturbation is applied at a specific potential to the system under investigation. As the name implies, the measured quantity is the impedance response of the working electrode. *Impedance* (Z) is analogous to *resistance* (R) in DC systems but describes the opposition to alternating current flow. While *resistance* is defined as the ratio of *potential difference* (E) to *current* (i), *impedance* accounts for the frequency-dependent nature of both current and potential in AC systems. The *frequency* (ω) is expressed as angular frequency in rad/s, equivalent to $2\pi f$ or Hertz (Hz). As previously anticipated, the electrical potential of the working electrode is measured or applied with respect to the potential of a reference electrode, for example, an Ag/AgCl electrode. During potentiostatic EIS the applied potential perturbation can be described as in **Equation 7**.

Equation 7: $$E(t) = E_0 cos(\omega t)$$

Where E_o is the *amplitude* of the overimposed sinusoidal wave, ω is the *angular frequency*, t is *time* and the term ωt is the *phase of the waveform*. The resulting *current response*, *i(t)*, oscillates at the same *frequency* of the input but exhibits a phase shift (ϕ), known as the *phase angle*, as represented in **Equation 8.**

Equation 8: $$i(t) = i_0 cos(\omega t - \phi)$$

The measured *current amplitude* (i_0) is inversely proportional to the system's electrochemical impedance at that specific frequency

During EIS measurements, the sinusoidal signal amplitude remains constant while the frequency is varied logarithmically, typically from 1 MHz to 10 mHz. The potentiostat software processes the potential and current data vs time using Fast Fourier Transform (FFT) to extract the potential magnitude vs frequency and current magnitude vs frequency,

respectively. The magnitude of the *impedance*, $|Z|$, is equal to the *potential* amplitude E_o divided by the *current* amplitude i_0 as shown in **Equation 9**.

Equation 9: $$|Z| = \frac{E_0}{i_0}$$

3.2.1.4.1 EIS Data Representation

EIS data are commonly displayed as Bode or Nyquist plots. Bode plots show the *impedance* magnitude ($|Z|$) and *phase angle* (ϕ) as functions of *frequency* on a dual-axis graph, as shown in **Figure 4**.

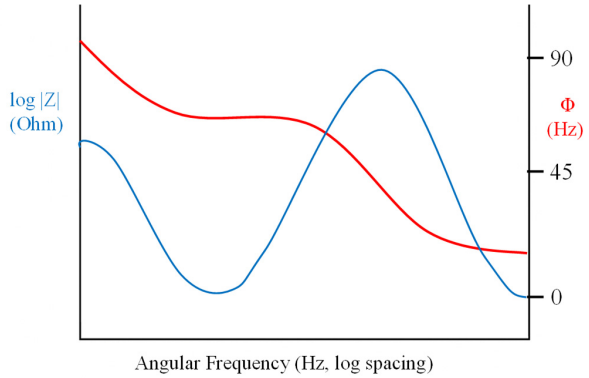


Figure 4: Example of a Bode plot [48]

Nyquist plot, the *impedance magnitude* $|Z|$ can be intended as a vector characterized by a module equal to $|Z|$ and an angle that is *phase angle* φ, as in **Figure 5A**. Cartesian coordinates may be used by breaking down the vector module ($|Z|$) into its x and y components[48], as presented in **Figure** 5**b**.

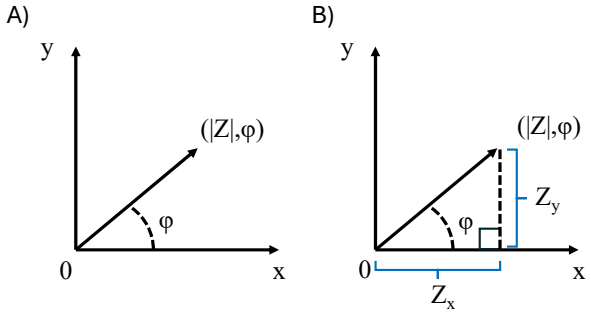


Figure 5: A) Representation of Z in polar coordinates, B) x and y components of Z.

Concerning **Figure 5b**, using trigonometry, it is possible to define the x and y components of Z, respectively Z_x and Z_y, as a function of the *module* and the *phase angle*, as reported in **Equation 10**, **Equation 11** and **Equation 12**.

Equation 10: $$Z_x = |Z| \cos \phi$$

Equation 11: $$Z_y = |Z| \sin \phi$$

Equation 12: $$|Z| = \sqrt{(Z_x)^2 + \left(Z_y\right)^2}$$

The obtained x and y components of the impedance's magnitude are addressed as *real impedance* Z_r (also, Z^I) and *imaginary impedance* Z_i (also, Z^{II}), respectively. The reason is due to the mathematical treatment of the polar representation of the *impedance* with Euler's formula to describe them using complex coordinates. However, the trigonometrical simplifications reported above lead to the same conclusion and suffice for the aim of this introduction to EIS measurements. Plotting on the x-axis the *real impedance* Z_r (or Z^I) and on the y-axis the negative *imaginary impedance* $-Z_i$ (Z^{II}), the Nyquist plot (**Figure 6**) is finally obtained[48].

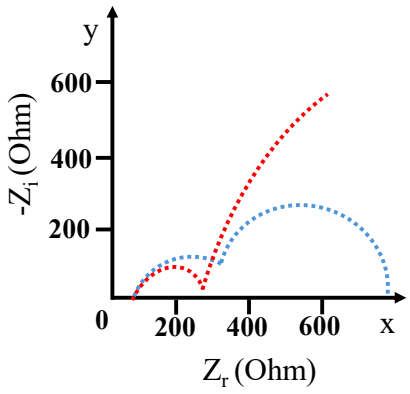


Figure 6: Examples of a Nyquist plot.

The reason why the Z_i are represented inverted is that the large majority of all Z_i are negative and doing so, it is possible to represent them in the first quadrant of the Cartesian plot.

3.2.1.4.2 Surface Oxide Thickness Calculation from EIS Data

Besides the real and imaginary components of the impedance, EIS measurements can provide other useful information that can be exploited for further calculations. Some, as shown in **Figure 7**, are immediately accessible or require minor data manipulation and fitting.

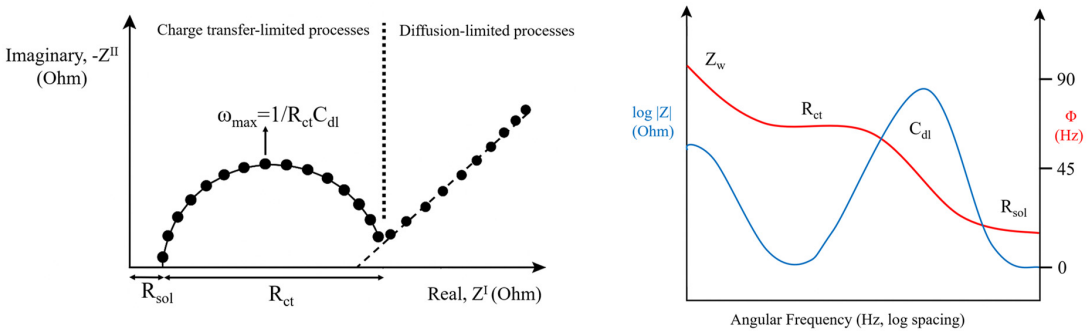


Figure 7: On the left: Nyquist plot. On the right: Bode plot. ω is the *angular frequency* ($2\pi f$), R_{ct} is the *charge-transfer resistance*, R_s is the *resistance of the solution*, C_{dl} is the *double-layer capacitance*, and Z_w is *infinite diffusion*.

Other characteristics of the investigated samples require some more calculations, such as the thickness of the superficial oxide scale, that can be calculated using the parallel capacitor approximation, as in **Equation 13**:

Equation 13: $$Scale\ Thickness = \frac{A \cdot \varepsilon_0 \cdot \varepsilon_{oxide}}{C_{real}}$$

Where A is the *geometric area* of the sample, in m^2, exposed to the electrolyte (i.e., the WE). $\mathcal{E}_0$ and $\mathcal{E}_{oxide}$ are the *electrical permittivity* (i.e., dielectric constant) values in the vacuum and in the oxide, respectively and C_{real} is the *capacitance* of the sample, which can be obtained with different methods. If the electrochemical process associated with the oxide layer is fully resolved in the EIS spectra, the *frequency-dependent real capacitance*, C_{real}, (**Equation 14**) can be used to estimate the oxide thickness [49]. Consequently, well-defined and complete capacitive arcs are required in the Nyquist representation to ensure that the oxide-related response can be clearly distinguished from other electrochemical processes. In addition, because the characteristic frequency of the oxide response may vary between samples, C_{real} should be evaluated at the characteristic frequency of each individual sample. Comparison of capacitance values obtained at a common frequency may otherwise introduce systematic errors in the calculated oxide thicknesses.

Equation 14: $$C_{real} = \frac{Z_{im}}{2\pi f\left(\left(Z_{real} - R_{sol}\right)^2 - \left(Z_{im}\right)^2\right)}$$

In **Equation 14**, the *frequency-dependent capacitance* of the sample (C_{real}, in Farad) is calculated from the values of Z_{im}, Z_{real} (in Ohm, respectively Z^{II} and Z^{I}) at that specific frequency and the *resistance of the electrolyte solution* (R_{sol}, in Ohm), while f is the *specific frequency* for which the *capacitance* is calculated (in Hertz).

Alternatively, the capacitance used for the oxide thickness calculation can be obtained from equivalent circuit fitting of the EIS data. The impedance spectra are fitted using an electrical circuit that describes the electrochemical processes occurring at the electrode/electrolyte interface and the quality of the fitting is verified through the X^2 and *normalized* X^2 values, respectively shown in **Equation 15** and **Equation 16**.

Equation 15) $$X^2 = \sum_{i=1}^{N} \left(\frac{|Z_{exp,i} - Z_{fit,i}|^2}{w_i^2}\right)$$

Equation 16) $$X^2_{normalized} = X^2 / |X^2|$$

Where Z_{exp} is the actual measured impedance, Z_{fit} is the calculated impedance and w is a *weighing factor*, equal to 1 if absolute or $w=|Z|$ if weighed on the actual impedance value to reduce the weight of large Z and improve the fitting quality for smaller impedance values.

Once good fitting is obtained, the parameters associated with the oxide layer are extracted. When a constant phase element (CPE) is used to account for non-ideal capacitive behaviour, an effective capacitance can be calculated from the fitted CPE parameters and subsequently employed for thickness estimation. If the oxide-related electrochemical process is fully resolved in the EIS spectrum, the real capacitance can be calculated using the Brug relation

(**Equation 17**), which converts the fitted CPE parameters into an effective capacitance through the associated resistance values, including the charge-transfer resistance (R_{ct}).

Equation 17) $$C_{eff} = (QR_{ct}^{1-n})^{1/n}$$

Where C_{eff} is the effective capacitance, Q and n are the fitted CPE parameters, and $R_{ct}$is the resistance associated with the same CPE branch. However, when the complete electrochemical process is not resolved within the investigated frequency range, R_{ct}cannot be determined reliably and the Brug relation cannot be applied. In such cases, if the CPE exponent (n) is sufficiently close to unity, indicating nearly ideal capacitive behaviour, the CPE coefficient (Q) can be approximated as the capacitance ($C_{real} \approx Q$) and used directly in the oxide thickness calculation. Compared with the frequency-dependent capacitance approach, equivalent circuit fitting provides a capacitance value associated with the complete oxide-related time constant and is generally less sensitive to the choice of a specific frequency. Nevertheless, the accuracy of the calculated oxide thickness remains dependent on the quality of the fit and the validity of the selected equivalent circuit model.

Estimates of the oxide layer thickness presented in this thesis have been calculated from the electrical permittivity values available in literature and summarized in **Table 1**.

Table 1: Oxides considered for the calculations of the surface scale thickness and their electrical permittivity

Oxide	Electrical Permittivity (F)	Source
Cr_2O_3	11.8-13.3	[50]
ZrO_2	11-15	[51], [52], [53]
NiO	11-12	[54]

However, it has to be noted that none of the investigated alloys exclusively form a singular type of oxide on their surface, but rather mixed oxides and hydroxides or chromium- and/or nickel-rich spinels supported by chromia. This simplification of the actual composition of the surface scale is a necessary step due to the lack of data and complexity of compositions.

4 Experimental

4.1 Materials

4.1.1 Alloys

All alloys investigated in this study, except AISI 441, were provided by Westinghouse Electric Company LLC® (Västerås, Sweden). The AISI 441 alloy was supplied by Alleima®, (Sandviken, Sweden). The nominal chemical compositions of the tested alloys are given in **Table 2**.

Table 2: Elemental composition of the investigated alloys in weight percentage (%^{wt}), according to ASTM standards[55], [56], [57], [58]. Reported values are maximum allowable quantities.

	AISI 441 (UNS S44100) (%^{wt})	**Inconel 718 (UNS N07718)** (%^{wt})	**Inconel X-750 (UNS N07750)** (%^{wt})	**Zircaloy-2 (UNS R60802)** (%^{wt})
Fe	Bal.	Bal.	5.0 – 9.0	0.07 - 0.2
Ni	1	50 - 55	70	0.03 - 0.08
Zr	-	-	-	Bal.
Cr	17.5 - 19.5	17 - 21	14 - 17	0.05 - 0.15
Nb	0.9	4.75 - 5.50	0.7 - 1.2	-
Mo	-	2.8-3-3	-	-
Ti	0.1 - 0.5	0.65-1.15	2.25 - 2.75	-
Mn	1	0.35	1	-
Sn	-	-	-	1.2 - 1.7
Co	-	-	1	1
Cu	-	0.30	0.5	-
Al	-	0.2 - 0.8	0.4 - 1.0	-
Si	1	0.35	0.5	-
N	0.03	-	-	-
S	0.03	0.15	0.01	-
C	0.03	0.08	0.08	-
B	-	0.006	-	-

The materials were supplied as foils with thicknesses ranging from 0.2 to 0.8 mm, the foils were cut using a manual sheet-metal guillotine. The dimensions chosen for the coupons were different depending on the experimental use: 2 x 1 cm for the studies of alloy composition impact on the steady-state concentration of hydrogen peroxide under gamma irradiation in water (**Chapter 5.2.**), and 3 x 1 cm for the electrochemical response under intermittent γ irradiation (**Chapter 5.3.**). For all the coupons, edges were ground with 1200-grit SiC abrasive paper (Struers®) to remove any burrs. Throughout this thesis, samples prepared according to this procedure are referred to as **as-received**. For selected experiments, all surfaces of the coupons were additionally ground using 500-grit (**Chapter 5.2.**), 1200-grit (**Chapter 5.3.**) and SiC abrasive paper (Struers®). Samples subjected to this treatment are hereafter referred to as **ground** samples. Before testing, all the samples were cleaned in an ultrasonic bath with acetone (Sigma-Aldrich®) for 10 min, followed by ethanol (Sigma-Aldrich®) for 10 min; this cleaning cycle was repeated twice.

4.1.2 Containers for Irradiation and Hydrogen Peroxide Reactivity Studies

The investigations presented in **Chapter 5.1.** and **Chapter 5.2.** were conducted using hydrolytic glass vials (Genetec®, articles 20090873 and 18090864) with a nominal volume capacity of 20 ml. Three types of septa were evaluated: (1) a 1.5 mm thick white silicone rubber septum (55 Shore A hardness) with a red PTFE lining (Genetec®, article 18032063), (2) a 3 mm thick translucent blue silicone septum (45 Shore A hardness) with a white PTFE lining (Genetec®, article 20030163), and (3) a 3 mm thick white silicone septum (50 Shore A hardness) with an aluminium foil lining (Genetec®, article 20030327). For clarity, these septa are identified throughout the following graphs as Septa 1, 2, and 3, respectively. The septa were mounted in either 18 mm magnetic universal screw caps with a central opening or 20 mm aluminium crimp caps with a central opening, as appropriate.

4.1.3 Solutions for Irradiation and Hydrogen Peroxide Reactivity Studies

The water used for all the investigations described in **Chapter 5.1.** and **Chapter 5.2.** was Milli-Q® water produced with in-house equipment. For the investigations involving the use of H_2O_2 solutions, to avoid the presence of stabilizers, hydrogen peroxide was produced radiolytically in house from ultrapure water (by Co^{60} irradiation in the irradiator reported above) and then diluted to achieve the concentration of 0.15 mM. For the studies involving higher concentrations of H_2O_2, solution were prepared from dilution of a 15 $\%^{wt}$ solution of H_2O_2 free of stabilisers sourced from Nouryon. All samples involved in the investigations presented in **Chapter 5.1.** and **Chapter 5.2.** were sealed under an ambient atmosphere once filled with 15 ml of solution.

4.2 Setup for γ Irradiation

Irradiations discussed in **Chapter 5.1** and **5.2** were performed by placing the samples in the exposure chamber of a shielded irradiator (Gammacell 220, Atomic Energy Canada Limited®) equipped with 12 GIK-7-4 type cobalt-60 sources. Prior to each irradiation campaign, the γ-dose rate was measured by chemical dosimetry (Fricke dosimetry) in different locations of the irradiation chamber and for different irradiation times to ensure that homogeneous irradiation of the samples was achieved. Given the half-life of Co^{60} of 5.2714 years, during the

experimental activities described in this thesis, the dose rate of the source decreased due to Co-60 natural decay ($t_{1/2} = 5.2712\ years$)[59]. The dose rate was measured to be ~1 Gy/s (~3.6 kGy/h) when the studies on the impact of septum materials on the accumulation of hydrogen peroxide under gamma irradiation of sealed vials started (**Chapter 5.1.**). The dose rate was then measured to be ~0.91 Gy/s (~3.27 kGy/h) and ~0.67 Gy/s (~2.47 kGy/h) for the studies on the impact of alloy composition on the steady-state concentration of hydrogen peroxide under gamma irradiation in water (**Chapter 5.2.**). For the studies on the electrochemical response under intermittent γ irradiation (**Chapter 5.3.**), The γ-dose rate was modulated by using none, one or two lead semi-cylindrical shields adjacent to the inner walls of the irradiation chamber. The resulting γ-dose rate was measured to be ~0.57, ~0.46 and ~0.25 Gy/s for the three shielding configurations (i.e., no shield, one shield, two shields, ~2.06, ~1.66 and ~0.9 kGy/h, respectively). In the experiments, the received doses of the samples were tuned by varying the irradiation time, knowing the dose rate in the irradiation chamber. During the experimental campaigns that extended for longer periods of time, the irradiation times were also adapted to the reduced activity of the source over time, to compensate for that, if not differently specified (see **Chapter 5.1.** and **Chapter 5.2.**).

The intermittent irradiation described in **Chapter 5.3.** was achieved by lowering and lifting the irradiation chamber at time intervals (i.e., circa 120 s) by manually operating the control switches. The manual operation, combined with the occasional malfunction of the chamber-position safety sensors (i.e., microswitches installed at the upper limit of the chamber travel path and on the hatch), resulted in variation in the duration of the irradiation cycles. Each irradiation cycle started and ended in the cold position and consisted of six irradiation sessions, separated by five rest periods of equal duration.

4.3 H_2O_2 Concentration Measurements

The H_2O_2 concentration was assessed by the triiodide method: 1 M potassium iodide solution (Sigma-Aldrich®) was freshly prepared and mixed with a pH 4.65 acetate buffer (Sigma-Aldrich®) solution spiked with ammonium molybdate tetrahydrate (Sigma-Aldrich®) and milli-Q water immediately before adding the sample in a volumetric ratio of 1:1:18:0.5 This precaution was taken to prevent ageing phenomena that could potentially alter the experimental results. For the same reason, absorbance measurements were performed shortly after their preparation. The photometric measurements were performed using a Varian® Lambda 25 and a VWR UV3000 UV-Vis spectrophotometer. The absorbance extinction coefficient for I_3^- was experimentally derived, measuring the absorbance of different dilutions of known amounts of H_2O_2 (Eka® HP). The H_2O_2 solutions used for calibration were also titrated with potassium permanganate ($KMnO_4$, Sigma Aldrich®) with a software-controlled titrator (Titrando 907, Metrohm®). The Absorption extinction coefficient of I_3^- at 350 nm was calculated to be $2.38 \cdot 10^4\ l\ mol^{-1}\ cm^{-1}$, well in agreement with various published values ranging between $2.32 \cdot 10^4\ l\ mol^{-1}\ cm^{-1}$[60] and $2.40 \cdot 10^4\ l\ mol^{-1}\ cm^{-1}$[61]. Absorbance measurements were performed at 350nm in single-beam mode, manually subtracting the absorbance of the blank sample before data plotting. The same 1 cm-path quartz cuvette was used for all the measurements.

For the samples subject to multiple sampling, at precise time (dose) intervals during the irradiation, 1 ml disposable syringes (disposable luer-slip two-parts tuberculin syringe, Fisher Scientific®) equipped with disposable 25 x 0.5 mm needles (Braun®) were inserted through the septa to withdraw a volume of the irradiated solution. The collected volume, between 0.1 and 0.2 ml, was transferred into a microtube (Eppendorf Snap Cap, 1 ml) and then used for H_2O_2 concentration measurements.

4.4 Electrochemical Setup and Parameters

The electrochemical measurements presented in this work have been performed with a SP300 potentiostat-galvanostat manufactured by BioLogic®. The instrument was controlled by a computer, through the Biologic software suite EC-lab, the same software was used for equivalent circuit fitting. All experiments were performed at ambient temperature and atmosphere.

4.4.1 Electrolytic Solutions

The EIS measurements presented in **Chapter 5.2.** were performed in 1%^{wt} sodium sulfate solution (Na_2SO_4, 70 mM). The Electrochemical investigations under intermittent γ irradiation presented in **Chapter 5.3.** were performed in three different electrolytic solutions.

1) Air-saturated water solution containing 70 mM Na_2SO_4.
2) Air-saturated water solution containing 0.15 mM H_2O_2 and 0.125 M Na_2SO_4 (Sigma Alrich®). For the experiments where the concentration of H_2O_2 in the electrolytic solutions was further increased, a 15 %^{wt} solution of H_2O_2 (Nouryon®) was used to spike the solutions.
3) Air-saturated water solution containing 0.15 mM H_2O_2, 0.125 M Na_2SO_4 and 0.2 M t-BuOH. (Sigma Alrich®). For the experiments where the concentration of H_2O_2 in the electrolytic solutions was further increased, a 15 %^{wt} mM solution of H_2O_2 (Nouryon®) was used to spike the solutions.

The formulation of the electrolytic solutions 2 and 3 were chosen in order to achieve good electrical conductivity using a known inert electrolyte, Na_2SO_4, and match the hydrogen peroxide content that would be radiolytically produced by γ irradiation of the solutions, so that to minimize the larger OCP drift that would be otherwise caused by its rapid increase in a solution originally containing none.

4.4.2 Radiation-Resistant Reference Electrode

It is known from the literature that Ag/AgCl electrodes perform satisfactorily under gamma irradiation, even at high temperature and pressure[62]. However, commercial reference electrodes have multiple parts (e.g., frit, frit connection, upper seal, etc.) made of polymers and resin. During the preliminary test of the setup, criticalities have arisen with different commercial electrodes. Unstable potentials, poor or intermittent electrical connection, and spikes in the current were indications that the polymeric parts of the RE were degrading due to irradiation and compromising the functionality of the electrodes themselves. A full-glass electrode, shown in **Figure 8**, was then assembled in-house.

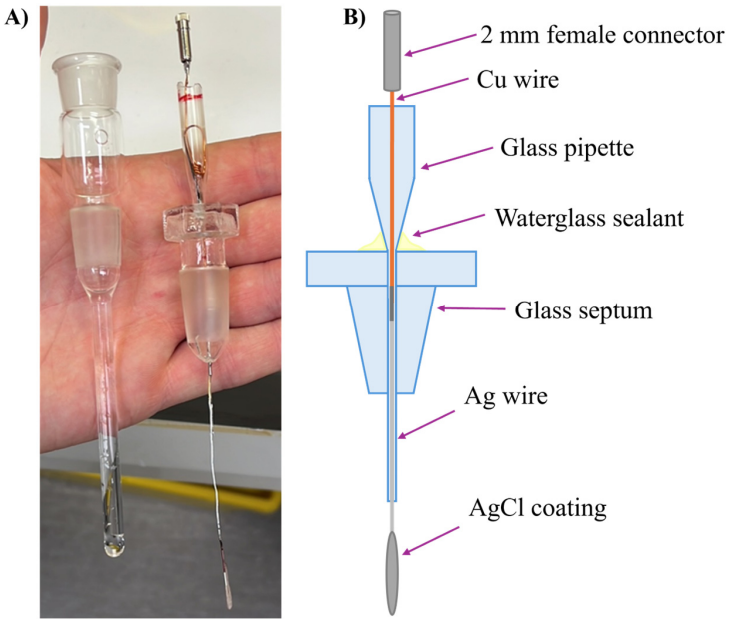


Figure 8: A) Self-assembled, full glass, Ag/AgCl electrode. Left: glass tube bridge, later filled with 3 M KCl solution. On the right: the inner structure with the AgCl-covered silver filament. B) Schematic representation of the reference electrode.

A silver filament covererd with AgCl was inserted into a shortened glass Pasteur pipette, leaving the portion covered in AgCl deposit protruding out of it. A copper wire of suitable diameter had one extremity covered in tin and inserted from the larger opening of the glass pipette until in contact with the Ag filament. A gas-fired blow torch was then used to melt the glass and seal the two wires in it, soldering the two at the same time. The as-obtained core was then inserted through a glass stopper (carefully drilled with a Dremel® tool and diamond bits) of dimensions suitable to fit in a glass bridge tube. The opening at the bottom of the stopper was sealed melting once more the glass with the torch. The upper opening, since not supposed to be in contact with any liquid, was sealed using a sodium trisilicate (water glass, $(NaOH)_x(Na_2SiO_3)_y{\cdot}_zH_2O$) solution. Finally, a 2 mm plug connector (Hirsher®) was soldered at the end of the copper wire, and the glass bridge tube was filled with a 3M KCl (Sigma Aldrich) solution. The assembled RE was tested vs a new RE (modular reference system, Ag/AgCl, 6.0724.140, Metrohm®) and proved its reliability, with a maximum discrepancy of 0.3 mV. The electrode was therefore used extensively for EC investigation under γ irradiation not reported in this thesis, proving its reliability.

The electrochemical measurements presented in **Chapter 5.3.** were performed with a miniaturized reference electrode built upon order by Redox.me® on the conceptual design of the electrode described above. In the new electrode, the outer structure in contact with the electrolytic solution (i.e, frit and bridge) was made of glass. Polyetheretherketone (PEEK) and Kapton® were used for the cap (working also as a connector shroud) and seal, respectively (i.e., polymers known for being radiation resistant and prone to low gas emissions[63]. The actual electrode was still an Ag/AgCl filament in 3 M KCl solution, while a stainless steel screw drilled with a 2 mm hole in diameter acted as connector for the potentiostat cable.

4.4.3 Counter Electrode

As the rest of the EC cell, the reference and counter electrodes are also irradiated during the measurements. During preliminary tests, the Pt counter electrode left submerged in a 0.1 mM non-stabilised H_2O_2 solution alone reduced its concentration by 13% in 3 h. The same test, repeated under irradiation, highlighted how the hydrogen peroxide concentration build-up due to radiolysis was slowed down, arguably due to the catalytic consumption of H_2O_2 on the Pt surface, further enhanced by its mesh structure. Further tests using a graphite rod have shown no alteration of H_2O_2 concentration over the same period and H_2O_2 build-up rate close to the reference sample under irradiation. Graphite was then the material of choice for the CE.

4.4.4 Radiation Resistant Electrochemical Cell

The EIS measurements of **Chapter 5.2**. were carried out in a custom-made well-type electrochemical cell, as represented in **Figure 9.** This specific cell design allows for testing of only one side of the sample, avoiding interferences from the edges and the back side of it, facilitating the control of the active area.

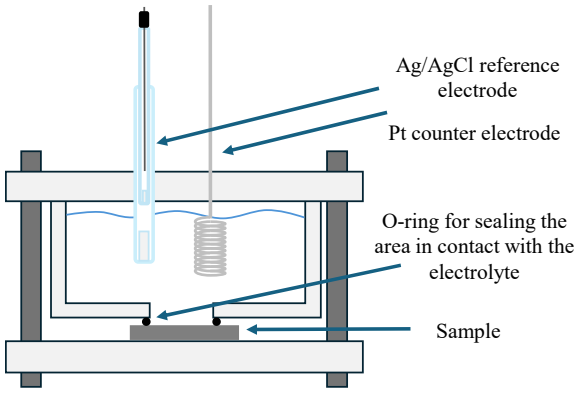


Figure 9: Cross-section of the custom-made electrochemical cell used for the EIS investigation of the samples.

However, the investigation of samples during irradiation requires specific precautions to prevent or limit possible biases and produce reliable, consistent measurements. First, all the materials of the electrochemical cell must be radiation-resistant. This is to prevent contamination of the electrolytic solution with the byproduct of materials' degradation under irradiation. Therefore, the EC cell presented above was dismissed, due to the perturbations that both the sealing O-ring and the PTFE walls could have had.

The use of a glass beaker was therefore preferred for EC measurements reported in **Chapter 5.3**. In order to perform an electrochemical measurement, the electrolyte must be in contact only with the surface of the WE, and not the electrical contacts (e.g., crocodile clamp, copper wires, etc.) used to connect it the EC setup. Given the availability of a Filament Deposition Modelling (FDM) 3D printer, an inexpensive electrode holder in a CAD software (SolidWorks 2021, Dassault Systèmes®) was designed to be placed it on top of the beaker, as shown in **Figure 10**. The holder, printed in commercially available modified Polylactic Acid (Creality® Ender PLA+) is characterised by three equidistant, circumferential holes. Such

holes are thought to accommodate adaptors (3D-printed too) to firmly keep in position the three electrodes, whatever their size or shape.

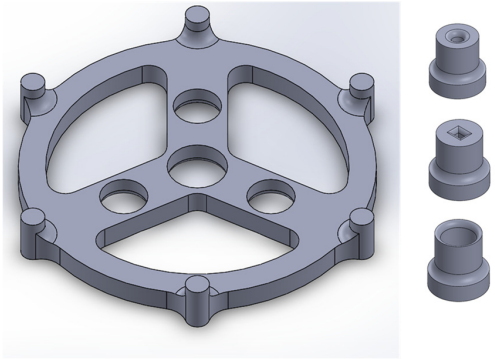


Figure 10: CAD model of the electrode holder and the adaptors. On the righthand side of the picture, from top to bottom: adaptor for the CE, adaptor for the WE and adaptor for the RE.

To control the WE surface area exposed to the electrolytic solution, and therefore electrochemically active, the adaptor for the WE was crossed by a copper strip of section 2 x 1 mm. A 2 mm connector was the extremity of the copper strip protruding above the EC cell. The extremity protruding the inner volume of the beaker (now turned into an EC cell) was instead bent into an "S" shape, to securely clamp the sample acting as WE, while simultaneously providing excellent electrical contact. The sample-WE (of 3 x 1 cm) was then submerged into the solution only for 2 cm, which translate in an active area of 4.3 cm^2 (2 cm^2 per side plus 0.25 cm^2 from the sum of the edges, given the sample thickness of 0.6 mm). The appearance of the as-obtained EC cell is shown in **Figure 11**

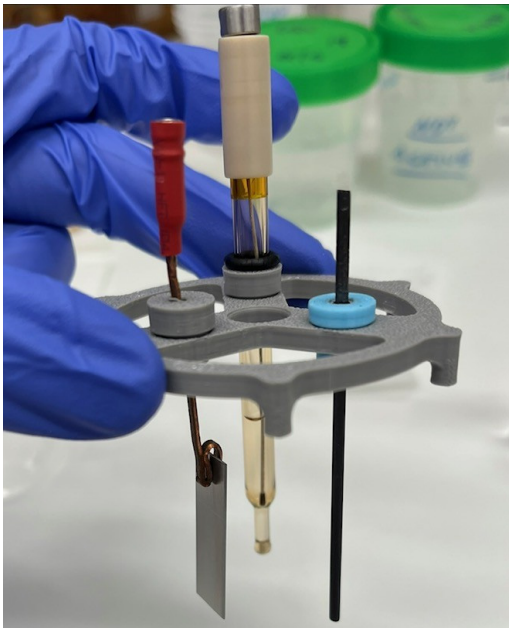


Figure 11: Appearance of the 3D-printed EC cell electrode holders quipped with the three adaptors accommodating the WE (left), the RE (center) and the CE (right).

4.4.5. Electrochemical Measurements Sequence and Parameters

The EIS measurements in **Chapter 5.2.** were performed at the OCP potential, previously measured until stabilization, in the range of frequencies between 1 MHz and 30 mHz. The amplitude of the superimposed sinusoidal excitation was 10 mV.

The electrochemical measurements presented in **Chapter 5.3.** were performed in series. Before each electrochemical characterization sequence on a sample, the system was left untouched for 1.5 h while monitoring the open circuit potential, in order to achieve a, pseudo-stable equilibrium state. Following the waiting period, measurements were performed in the following order: Electrochemical Impedance Spectroscopy (EIS) at the measured OCP, Linear Sweep Voltammetry (LSV), OCP, Chrono Amperometry (CA) or OCP during intermittent irradiation, OCP, EIS, LSV and OCP again.. EIS measurements were carried out in the range from 1 MHz to 300 mHz, with an applied signal amplitude of 10 mV. LSV measurements were performed from -100 mV to +100 mV with respect to the measured OCP at a scan rate of 1 mV/s. EIS and LSV measurements were used to investigate the properties of the sample before and after irradiation or chemical addition of H_2O_2. To verify that the settings chosen for each step were not altering the sample, compromising the validity of the following measurements, preliminary OCP and LSV measurements were also performed before/after each step independently. During certain runs (i.e., for dose rates of 0.25 and 0.46 Gy/s). EIS and LSV measurements were excluded. During the tests involving chemical addition of H_2O_2 instead of intermittent irradiation, OCP measurements were performed instead of CA. During the CA measurements, the WE was kept at the last stable OCP potential measured before the chrono amperometry and contextual γ irradiation. A schematic representation of the measurements sequence is shown in **Figure 12**.

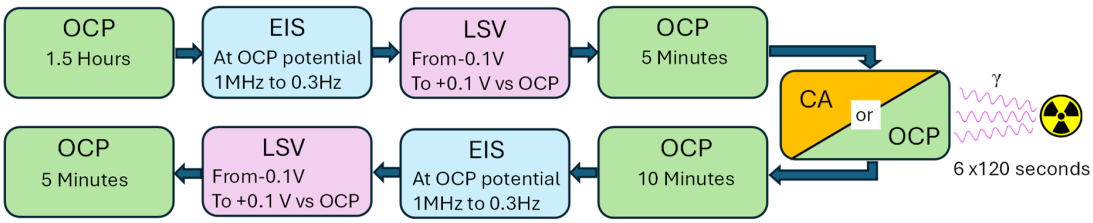


Figure 12: Schematic representation of the electrochemical measurements and their order in each investigation cycle in Chapter 5.3.

5 Results and Discussion

5.1 Impact of Septum Materials on the Accumulation of Hydrogen Peroxide under γ Irradiation of Sealed Vials

5.1.1 Accumulation of Hydrogen Peroxide under γ Irradiation

The H_2O_2 concentration measured in aqueous solutions contained in glass vials irradiated up to 250 kGy is plotted vs the received dose in **Figure 13**. The vials were sealed by three different types of septa (i.e., white silicone rubber/red PTFE, blue silicone rubber/white PTFE and white silicone rubber/Al lining). Both sides of the septa were tested facing the headspace, for a total of six samples that were irradiated simultaneously. During irradiation, the vials were kept in upright position, preventing the direct contact of the solutions with the septa.

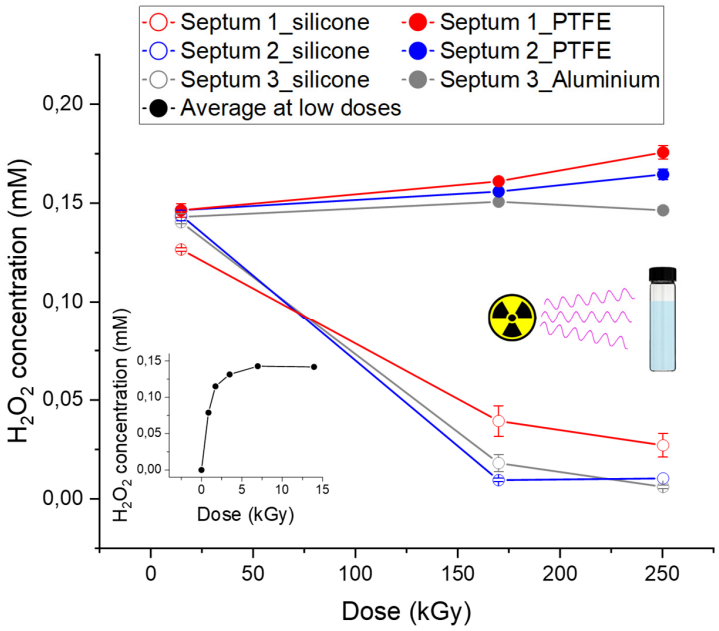


Figure 13: Measured H_2O_2 concentration versus received dose for the six irradiated samples, three for each type of septa facing the vial (septum 1, red: red PTFE/ white silicone rubber, septum 2, blue: PTFE/blue silicone rubber and septum 3, grey: aluminium/white silicone rubber). Hydrogen peroxide concentration measurements were performed at 14.8, 170 and 250 kGy received dose intervals. In the inset: the median of the H_2O_2 concentration measured at lower doses (between 0 and 13.9 kGy). In the inset: average H_2O_2 concentration versus received dose for the six irradiated samples in the range 0–15 kGy

The measured concentrations of hydrogen peroxide in the six samples are comparable up to an absorbed dose of 14.8 kGy, as visible in **Figure 13**. At 250 kGy, however, the samples can be clearly categorized into two distinct groups based on their H_2O_2 content. Specifically, the samples sealed with aluminium (Al) and polytetrafluoroethylene (PTFE) linings in contact with the headspace have H_2O_2 concentrations ranging from 0.16 to 0.19 mM. In contrast, samples sealed with silicone rubber septa have markedly lower concentrations, approximately

0.02 mM, representing only 10.5% to 12.5% of the concentrations observed in samples sealed with Al and PTFE septa. These findings indicate that the divergence in H_2O_2 accumulation begins to emerge between 14.8 and 170 kGy, with no appreciable differences detected at lower doses (0–14.8 kGy).

To determine whether the observed variations are attributable solely to the sealing material or also to its exposure to the gaseous headspace, a second series of experiments was conducted in which the vials were inverted. This configuration placed the septa in direct contact with the aqueous solution while isolating the gaseous headspace from the sealing material, which was instead in contact with the glass. The results of these inverted-vial experiments are presented in **Figure 14**. Throughout the entire duration of this series, the vials were maintained in the inverted position to ensure continuous contact between the sealing septa and the contained solution.

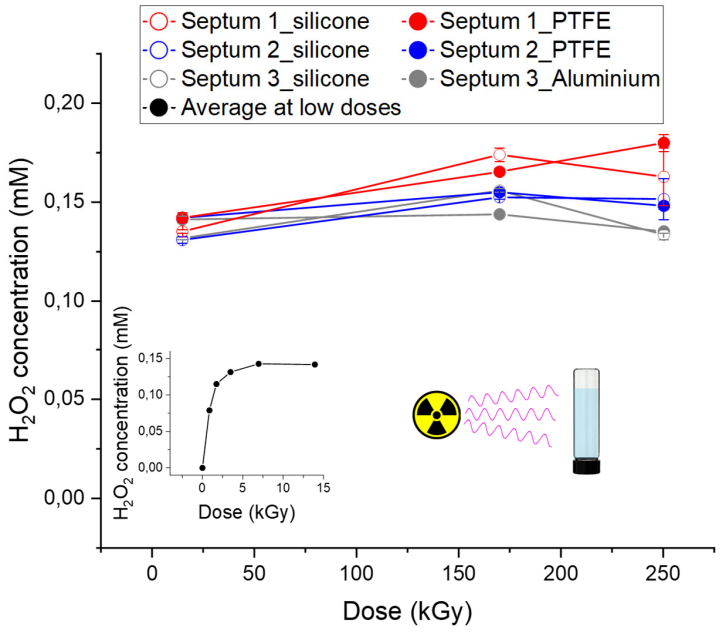


Figure 14**:** H_2O_2 concentration versus absorbed dose for the six irradiated samples, two for each type of septa facing the vial (septum 1, red: red PTFE/ white silicone rubber, septum 2, blue: PTFE/blue silicone rubber and septum 3, grey: aluminium/white silicone rubber). Hydrogen peroxide concentration measurements were performed at 14.8,170 and 250 kGy. Samples were kept in the upside-down position for the whole duration of the experiment. In the inset: average H_2O_2 concentration versus received dose for the six irradiated samples in the range 0–15 kGy.

As can be seen in **Figure 14**, when the vials are placed upside-down and the materials are in direct contact with the solution, the difference observed in **Figure 13** is no longer present. Hence, the impact of silicone in contact with the inner environment of the vials is only seen when it is in contact with the headspace.

5.1.2. Reactivity of Hydrogen Peroxide towards Septa Materials in Normal Conditions

Subsequently, the H_2O_2 concentration (originally equal to 0.15 mM at the start of the experiment) was monitored in the absence of γ-radiation after 28 days, to explore the hydrogen peroxide reactivity towards the investigated septa materials. The results are presented in **Figure 15.**

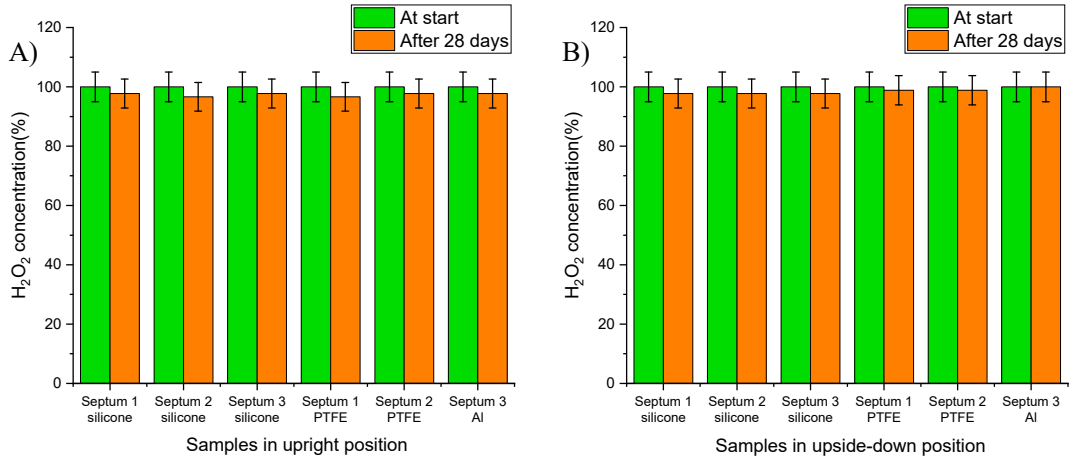


Figure 15: A) Relative H_2O_2 concentration of the six investigated samples, three for each kind of septa kept in the upright position for the entire duration of the test. B) Relative H_2O_2 concentration of the six investigated samples, kept in the upside-down position for the entire duration of the test. Vials were filled with 0.15 mM H_2O_2. In green, the H_2O_2 concentration was measured at the beginning of the test. In orange, the H_2O_2 concentration was measured after 28 days.

Over the investigated period of 28 days, none of the septa, either kept in the upright or upside-down position, exhibited any significant reactivity towards H_2O_2, as clearly shown in **Figure 15**. A minimal decrease in hydrogen peroxide content is however expected, given the inherent instability of H_2O_2 and the lack of preservatives. Therefore, it is evident that the phenomena observed in **Figure 13** and **Figure 14** cannot be simply attributed to the reactivity of H_2O_2 toward the tested materials.

5.1.3. The Role of Septum Materials - Discussion

As shown in the previous subchapters, the discrepancy between H_2O_2 concentrations in vials where silicone is facing the inside as compared to where Al or PTFE is facing the inside is only observed when silicone is in contact with the gaseous head space (**Figure 13**). In addition, H_2O_2 does not display any reactivity towards any of the materials used in this study (**Figure 15**).

Polymers are known to undergo γ-radiation-induced modification (ionization and bond scission leading to radical formation, scission, cross-linking and crystallisation, to name a few), resulting in alteration of chemical and mechanical properties[64]. In polysiloxanes (silicone polymers), the impact of irradiation depends on the received dose rate and the availability of oxygen and water[65], [66], [67]. The same parameters also affect the release of radiolytic gases in terms of relative composition and intensities [65], [66], [67]. Among the radiolytic gases released by silicones, the most common are CO_2, CH_4 and H_2[65], [66], with carbon dioxide being the most abundant gaseous product if oxygen is available during irradiation[66]. The proposed mechanism involves radical reactions or oxidation of the methyl group of polysiloxane, as discussed by Wang et al[67]. According to the figure published by B. Liu et al[65], silicone encapsulant irradiated under a nitrogen atmosphere at a dose rate of 0.85 Gy/s mostly releases CH_4 and H_2, with a gas yield of about 0.02 μmol s^{-1} per gram of polymer, which corresponds to a surprisingly high G-value of 20 μmol/J.

Similarly to silicone, polytetrafluorethylene (PTFE) is strongly affected by γ-radiation and is known for releasing radiolytic gases such as SiF_4, CF_4, C_nF_{n+2}, C_3F_8[68], [69] and even HF[70]. Aluminium is expected to be reactive towards the radiolytic oxidants and produce Al_2O_3.
The H_2O_2 reactivity test presented in **Figure 15** clearly shows that direct reactions between H_2O_2 and the different materials tested in this work are not the reason for the observed discrepancy. The fact that the H_2O_2 concentration is more or less the same when Aluminium is facing the system (direct contact with solution or head space, **Figure 14** and **Figure 13**) as when PTFE is facing the system (direct contact with solution or head space, **Figure 14** and **Figure 13**) indicates that gas release from the irradiated PTFE does not affect the H_2O_2 concentration up to 250 kGy. The fact that when silicone is facing the solution (**Figure 14**), the H_2O_2 concentration is more or less the same as when Aluminium is facing the solution or the head space (**Figure 14** and **Figure 13**), implies that gas release from the irradiated silicone rubber is not the reason for the observed discrepancy when silicone is facing the head space. Gas release from both PTFE and silicone rubber should mainly be attributed to direct effects (i.e., the radiation energy is absorbed directly by the material) and be independent of whether the material is in contact with the solution or the head space. Upon gamma-irradiation, PTFE will form radicals along the polymeric chain ($-CF_2-\dot{C}F-CF_2-$, R•) and at the termination of it ($\dot{C}F_2-CF_2-$, P•)[71]. Other studies have found PTFE yields for R• and P• radicals in a ratio up to 10:1[72], presumably due to the recombination of the broken C-C bonds due to cage effects[71]. In presence of humid air (i.e., oxygen and water), γ-irradiation induces chain scissions, leading to the formation of both chain ($-CF_2-CFOO\dot{}-CF_2-$) and terminal ($-CF_2-CFOO\dot{}$) peroxyl radicals[70], [73], [74] in a ratio close to 1:1[73]. Both fluoroalkyl and peroxyl radicals along the main polymeric chain have been reported to be rather stable at temperatures

below 100ºC[73]. The degree of crystallization in irradiated PTFE has been reported to increase with the received dose, limiting chain movement and therefore further stabilizing the radicals[75].
Upon gamma irradiation, silicones will undergo crosslinking, going through the formation of -Si-CH_2•, and -Si• [75], [76], [77], producing H_3C• as well, as reported by Menhofer and Heusinger. The presence of oxygen is known to interfere heavily with the crosslinking process[78], reducing the crosslinking yield by a factor 3 under electron irradiation[76]. In presence of air, -SiCH_2•, and -Si• are expected to react with oxygen to form their peroxyl derivatives, which in turn hinder the crosslinking process[35], [79]. A number of studies reported that both crystallization rate and crystallinity degree are negatively affected by irradiation, with 1 MGy dose eliminating crystallization, as a result of crosslinking[77], [80], [81].

It is generally known that permeability, diffusivity and solubility of gases in polymers are affected by the degree of crystallinity. In fact, diffusion and permeation coefficients decrease significantly in crystallised polymers compared to amorphous ones, and oxygen solubility is reduced in crystalline regions[82]. Polymer chains are tightly and ordinately packed in crystalline regions, forming finite volumes where gas passage of molecules is hindered, therefore limiting diffusion and dissolution[83]. In addition to the differences in crystallization behaviour when exposed to ionizing radiation, PTFE and silicone rubber are characterised by intrinsically different oxygen permeability coefficients, with PDMS being up to 10^2 times more permeable than PTFE. At 35 °C, oxygen permeability values are reported as $2.28 \cdot 10^{-5}$[84] and $2.68 \cdot 10^{-3}$[85] mol m/(m² s Pa) for PTFE and PDMS, respectively, while their corresponding diffusivity values are $2.2 \cdot 10^{7}$[84] and $3.4 \cdot 10^{7}$ cm²/s[85].
As seen above, both PTFE and PDMS form radicals under irradiation that are reactive towards O_2 thus enabling consumption of O_2 in the headspace. While the reactivity of the radicals formed upon irradiation towards O_2 is similar for both materials, the significant difference in oxygen permeability and diffusivity, both intrinsic and irradiation-induced, govern the rate at which O_2 can diffuse through the polymer and replenish the consumed oxygen. This results in different O_2 consumption dynamics and consequently different concentration evolution profiles.

In the experiments performed in **Chapter 5.1.1.**, 15 ml of air-saturated water is irradiated with 5 ml head space of air. At room temperature, the amount of molecular oxygen (O_2) in the head space is more than ten times higher than the amount of molecular oxygen in the solution. Given the difference in volume, the concentrations differ by a factor of 30. This implies that the rate of reaction between the radicals formed in the polymer and O_2 will be much higher when the head space is in contact with the silicone rubber compared to when the aqueous solution is in contact with the silicone rubber, not including the impact of viscosity which will further enhance the difference. A more rapid consumption of O_2 from the head space will lead to depletion of O_2 in the solution as the equilibrium between the gas phase and the liquid must be maintained.

This, in turn, could explain the lower concentrations of radiolytically produced H_2O_2 accumulated in irradiated solutions exposed to PDMS, since O_2 is the most important precursor

for H_2O_2 formation under gamma irradiation in air-saturated aqueous solution, according to the mechanism presented in **Equations 18-21**.

Equation 18) $e_{aq}^- + O_2 \rightarrow O_2^-\bullet$

Equation 19) $H^+ + O_2^-\bullet \rightarrow HOO\bullet$

Equation 20) $H\bullet + O_2 \rightarrow HOO\bullet$

Equation 21) $HOO\bullet + HOO\bullet \rightarrow H_2O_2 + O_2$

Where H• is one of the products of water radiolysis, which would otherwise contribute to H_2O_2 degradation[26], as presented in **Equation 22**.

Equation 22) $H\bullet + H_2O_2 \rightarrow H_2O + HO\bullet$

In oxygen-free aqueous solutions, H_2O_2 is primarily formed from recombination of hydroxyl radicals in the early stages of radiolysis. The yield of this reaction is relatively low in gamma-radiolysis [86].
When the silicone rubber is facing the solution, as in **Figure 14**, the rate of reaction between O_2 and the radicals in the polymers is significantly lower (due to a lower O_2 concentration and increased diffusion resistance in the aqueous phase), and the significantly larger amount of O_2 in the head space will rapidly compensate for any consumption in the liquid phase. To the best of our knowledge, C-centered radicals do not display significant reactivity towards water unless the water has been activated through the formation of a complex where the bond dissociation enthalpy of the O-H bond can be significantly reduced. In fact, there are numerous studies of alkyl radical reactivity towards other solutes in aqueous solution where reactions with the solvent are not considered to be of significance. Indeed, certain alkyl radicals could be protonated in water to produce the corresponding radical cation, provided the pH is low enough. However, in our system we do not see that we have the conditions required for such reactions. Hence, reaction with O_2 is the most probable reaction for C-centered radicals formed also in contact with the aqueous phase. Given reduced reaction rate with O_2 present in the aqueous phase, it is plausible that cross-linking is favoured.

The experiments presented in this work have all been conducted at a constant dose rate. However, it is quite probable that the dose rate will have an impact on the radiation-induced process in the silicone rubber as well as in the PTFE. This would probably be reflected by a change in steady-state concentrations of H_2O_2 in the aqueous phase. At higher dose rate, the concentration of C-centered radicals in the irradiated silicone rubber will be higher, which most probably will result in a higher fraction of radical-radical reactions compared to reactions between radicals and O_2. This would reduce the consumption of O_2 at a given dose and thereby reduce the impact on H_2O_2.

5.2 Impact of Alloy Composition on the Steady-State Concentration of Hydrogen Peroxide under γ Irradiation in Water

5.2.1 Hydrogen Peroxide Accumulation under γ Irradiation

Hydrogen peroxide concentration was measured for the irradiated solutions containing the alloys in both as received (A) and ground condition (B) at dose intervals of 0, 0.085, 0.6, 1.2, 1.7 and 2.2 MGy (**Figure 16**) and after a received dose of 2.2 MGy (**Figure 17**).

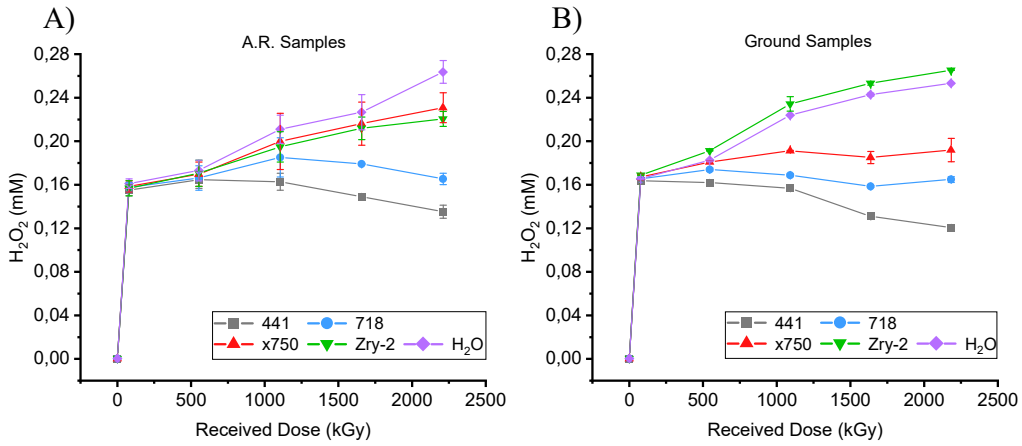


Figure 16: Hydrogen peroxide concentration measured for the investigated alloys in both A) as received and B) ground conditions irradiated in pure water as a function of dose. The first point refers to the hydrogen peroxide concentration prior to irradiation. The "reference" sample is pure water with no addition of alloys for both the sets of experiments.

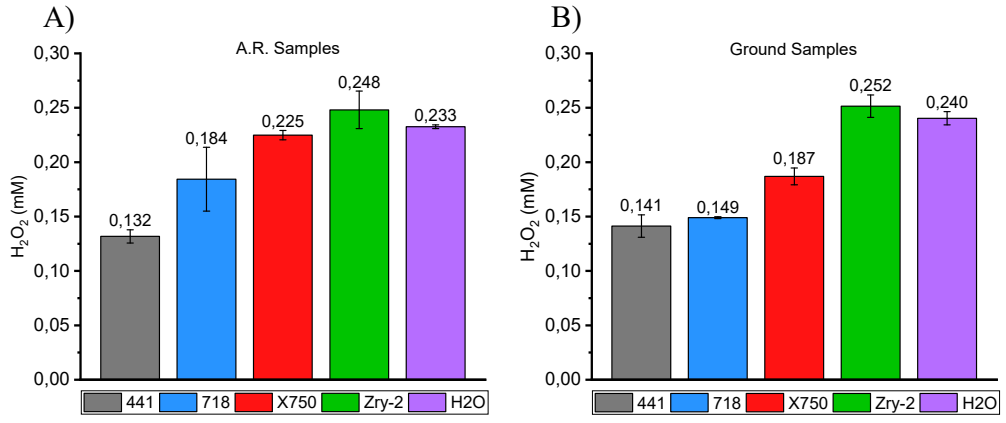


Figure 17: Hydrogen peroxide concentration measured for the five investigated alloys in both A) as received and B) ground conditions and bare water after a total received dose of 2.2 MGy.

As presented in **Figure 16A** and **Figure 16B**, the hydrogen peroxide levels in the solutions follow different trends, depending on the composition of the alloy submerged in them during irradiation. In particular, the ferritic stainless steel AISI 441 sample (in grey) reached a

remarkably low H_2O_2 concentration (i.e., 40 to 50% less) compared to the pure water acting as a reference (in purple) in both as received (**Figure 16A** and **Figure 17A**) and ground conditions (**Figure 16B** and **Figure 17B**). Inconel 718 (in blue), while reaching higher concentrations compared to AISI 441, only reaches a fraction of the H_2O_2 concentration measured for reference in both sets of experiments. Inconel X-750 and Zircaloy-2 behaved similarly to each other when tested in as received conditions and differently once ground. In general, it seems that the H_2O_2 concentration increases in a similar way up to 0.6 MGy in all the investigated solutions and then takes different paths depending on the material submerged in the solution. Some solutions (e.g., the reference and Zircaloy-2) display further increase in hydrogen peroxide concentration while others display mildly (i.e., Inconel 718) to consistently strongly decreasing concentrations (i.e., AISI 441) beyond 0.6 MGy. Inconel X-750 exhibits both tendencies depending on its surface finishing: as received samples further increase hydrogen peroxide content, while ground samples seem to reach a lower, steady state concentration, as confirmed by both multiple (**Figure 16**) and single received dose measurements (**Figure 17**). The observed results could potentially be attributed to several factors. Multiple sampling from the same vial can lead to alterations of the atmosphere in the head space of the vials. However, the good agreement between the results presented in **Figure 16** (multiple sampling) and **Figure 17** (single sampling) implies that alteration of the head space atmosphere is not a major issue. It has also been shown that the silicone rubber of the septa exposed to the inner environment of the vial through the opening in the Al lining made by the needle, can influence the H_2O_2 concentration at doses higher than 70 kGy [87]. As the same type of septum was used in all experiments, the impact of the septum should be the same for all vials. By grinding the surface of the samples, the protective oxide layer is removed and a different surface composition may be exposed to the solution. Interestingly, for both the Inconel 718 and the Inconel X-750 alloy samples H_2O_2 concentrations were negatively affected by the grinding process.

5.2.2 Influence of Pre-Oxidation on Hydrogen Peroxide Accumulation under γ Irradiation

To investigate whether a greater thickness of the oxide scale could influence the hydrogen build-up under irradiation, samples of AISI 316L alloy have been heat-treated in a tube furnace in air atmosphere at 800° C for different time extents, leading to different oxide thicknesses and, conceivably, surface morphology and chemical compositions too. Subsequently, the samples have been submersed in water and irradiated with gamma radiation. H_2O_2 concentrations were measured at a received dose of 1 MGy and are shown in **Figure 18**.

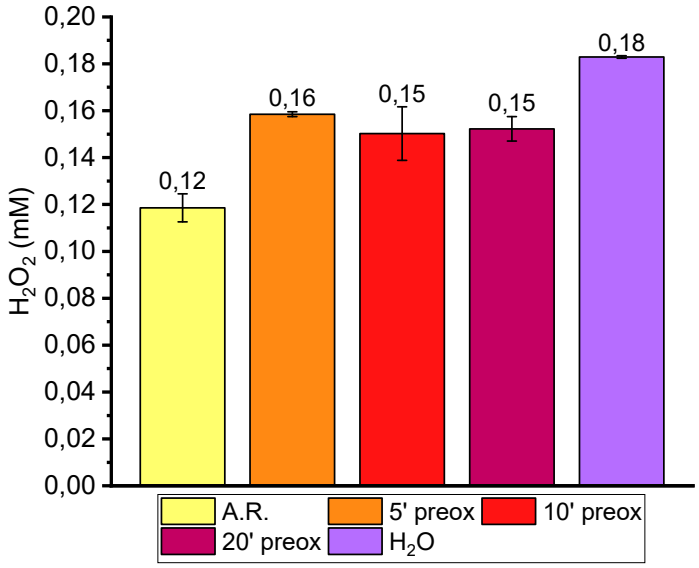


Figure 18: H_2O_2 concentration, in mM, of the irradiated water solution containing AISI 316L alloy samples, as received and pre-oxidized at 800 °C for 5, 10 and 20 minutes. The samples identified as "H_2O" refer to the vials containing only water; no alloy coupons were submerged in the solution. The received dose at the time of the sampling was 1 MGy.

As visible in **Figure 18**, the thermal treatment, and hence the progressively increasing thickness of the oxide scale, seems not to affect the long-term hydrogen peroxide concentration, with the three samples achieving very similar values. However, despite the comparable surface to volume ratios, the amount of H_2O_2 found in the solution hosting the as-received sample is 25 % less than for the pre-oxidised samples. This unexpected trend suggests a possible correlation between the thickness of the surface oxide and/or composition/morphology and their influence on H_2O_2 accumulation under irradiation.

5.2.3 Hydrogen Peroxide Reactivity towards Alloys in Normal Conditions

In order to assess the impact of a direct reaction between H_2O_2 and the surfaces of the materials under study, an experiment investigating the stability of a 0.15 mM H_2O_2 solution in contact with the alloy samples was conducted using the same surface area to solution volume ratio as in the irradiations. The hydrogen peroxide concentration for each vial was measured after 1 month, corresponding to the maximum irradiation time of the samples in **Figure 16** and **Figure 17**. The measured H_2O_2 concentrations after the one-month stability experiments for both as received (A) and ground (B) samples are presented in **Figure 19**.

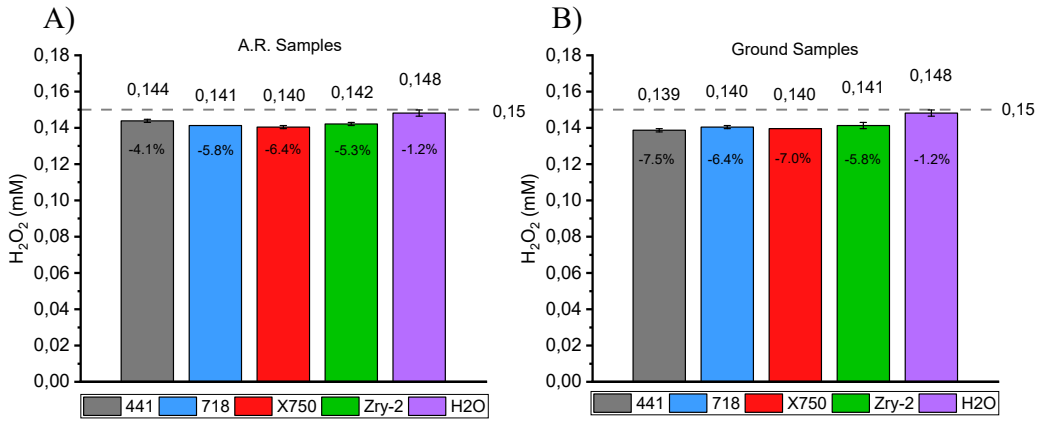


Figure 19: Hydrogen peroxide concentration measured for the originally 0.15 mM solution in contact for a month with A) as received and B) ground samples. The values within the columns refer to their change (in %) with respect to the starting concentration. The reference solution did not contain any alloy.

As can be seen in **Figure 19**, neither as received (**Figure 19A**) nor ground samples (**Figure 19B**) display any significant reactivity towards H_2O_2. Admittedly, the H_2O_2 concentration is reduced in all solutions and it is clear that the reduction is more significant in the vials containing a metal foil compared to the pure aqueous reference solutions. This may simply be due to a slightly larger solid surface area to solution volume ratio in the vials containing the metal foils. The composition of the alloy does not appear to affect the consumption of H_2O_2 in these tests. Hence, the trends observed in **Figure 16** and **Figure 17** cannot be attributed to the direct reaction between H_2O_2 and the alloy surfaces.

5.2.4 Surface Investigation after Irradiation and Exposure to Hydrogen Peroxide

5.2.4.1 Scanning Electron Microscopy

As shown in **Figure 19**, we know that H_2O_2 reactivity without irradiation is very low. However, we cannot assume yet that the behaviour of hydrogen peroxide is the same also under irradiation. Therefore, SEM investigations were performed on both as-received and subsequently irradiated samples to assess the effect of gamma irradiation and exposure to water radiolysis products on the surface of the alloys. The samples depicted in **Figure 20-23** are the same object of the irradiation and subsequent H_2O_2 measurements of **Figure 17A**. Considering the volume of the irradiated water samples, the final concentrations of H_2O_2 (presented in **Chapter 5.2.1.**), and assuming that the difference, relative to the reference, was consumed in surface oxidation reactions on the alloys, the resulting oxide scale thickness would be expected to range from a few hundred nanometers to approximately one micrometer. This broad range is attributed to simplifications in the calculation, variability in the measured H_2O_2 concentrations, and assumptions regarding the composition of the oxide scale.

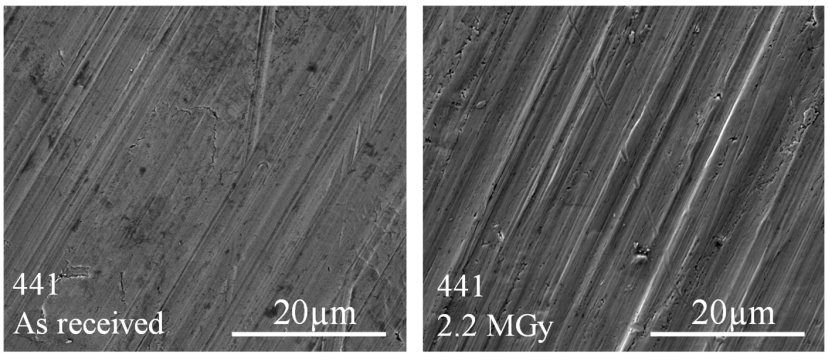


Figure 20: Surface SEM micrograph of A) as received, not irradiated and B) as received, irradiated AISI 441 samples.

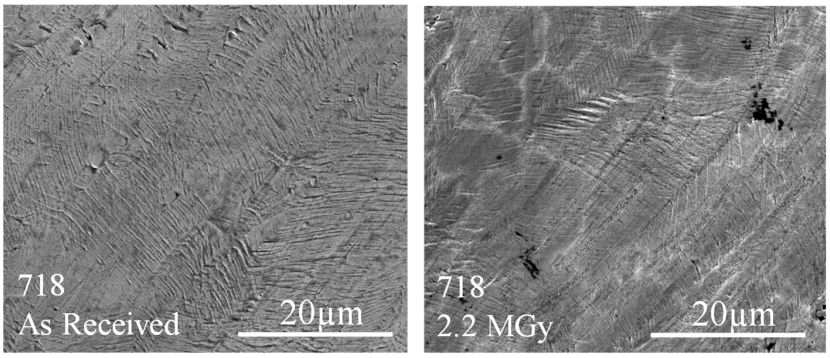


Figure 21: Surface SEM micrograph of A) as received, not irradiated and B) as received, irradiated Inconel 718 samples.

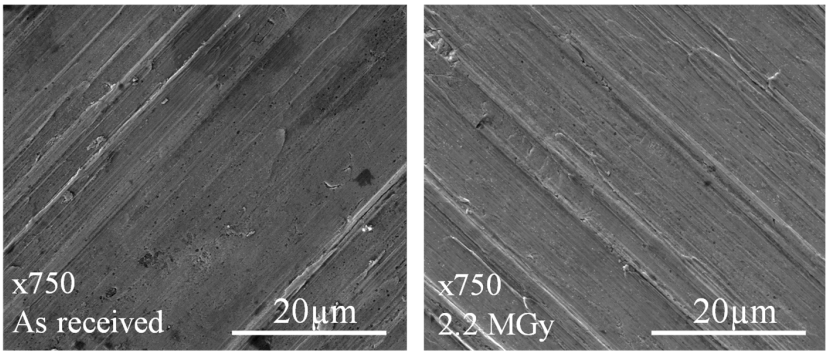


Figure 22: Surface SEM micrograph of A) as received, not irradiated and B) as received, irradiated Inconel X-750 samples.

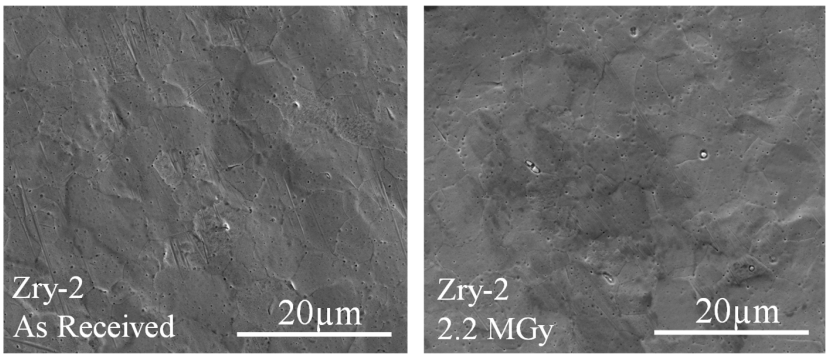


Figure 23: Surface SEM micrograph of A) as received, not irradiated and B) as received, irradiated Zircaloy-2 samples.

As visible in all the SEM micrographs presented above, the surface of the alloys seems unaffected by the irradiation and the simultaneous exposure to the product of water radiolysis. Features such as the ridges resulting from the surface finishing of the alloys (**Figure 20-23**) and even grain boundaries (**Figure 23**) are visible on the samples both before and after irradiation. Such features are not compatible with the expected oxide, calculated according to the abovementioned reasoning. Only a few minor differences are identifiable between micrographs and could be justified by the normal differences among areas of the same sample (especially considering their "as-received" condition), slightly different setting of the instrument and so forth.

However, it is not possible to exclude that the treatment has altered the oxide thickness on a scale below the appreciation threshold granted by SEM investigation of the surface (e.g., in the order of a few nanometers). For such a reason, a complementary investigation of the samples has been performed with XPS and EIS, which allows a greater sensitivity to the very surface of the samples.

5.2.4.2 X-Ray Photoelectron Spectroscopy

To explore the impact of radiolysis on the surfaces of the samples, XPS was performed on as received samples before γ-irradiation (acting as references), on samples irradiated while submerged in water up to 2.2 MGy and after being submerged in a 1 mM H_2O_2 solution for 28 days. X-ray photoelectron spectroscopy is a surface-sensitive technique that probes the top ~5-10 nm of a material by measuring the kinetic energy of photoelectrons emitted upon X-ray irradiation. It provides quantitative elemental composition and chemical-state information. In this work, the coexistence of metallic and oxidic signals in the XPS spectra was used to infer that the surface oxide layer was substantially thinner than the typical interaction depth. The collected XPS spectra are shown in **Figure 24-27**, grouped by type of material. Each column of spectra belongs to a different sample, and each row investigates the strongest core levels of a different element. From the high-resolution XPS spectra of AISI 441 samples presented in **Figure 24**, the three samples have in common a thin surface oxide layer. Signals of metallic Fe and Cr are distinctly discernible, accounting for between 18 and 24 % of total signals for each element. The as-received and H_2O_2-submerged samples' peak counts differ by less than

1% for both Fe and Cr, while the irradiated sample is characterized by slightly higher iron oxide content (i.e., 3%). The limited depth (i.e., from 5 to 10 nm) of the interaction volume scrutinized by XPS investigation, and the minimal differences between samples suggest that the surface oxide layers are comparably thin, with differences well below 1 nm.

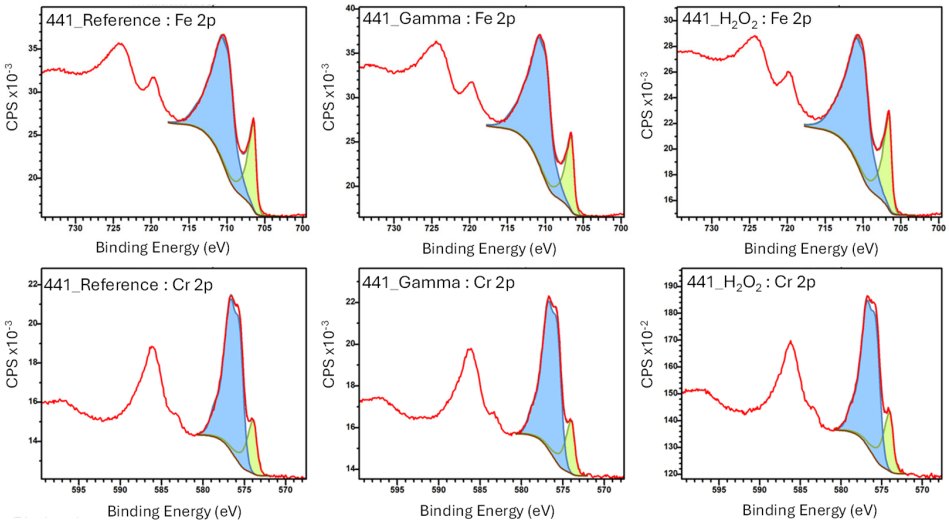


Figure 24: High resolution XPS spectra of AISI 441 samples. From right to left: as-received, irradiated up to 2.2 MGy in water and submersed for 28 days in a 1 mM solution of H_2O_2. The fitting of the 2p peaks for iron in its metallic state (green) and in the form of oxides (blue) in presented in the upper row. The fitting of the 2p peaks for chromium in its metallic state (green) and in the form of oxide and hydroxide (blue) is presented in the bottom row.

The XPS spectra of Inconel 718 samples, presented in **Figure 25**, highlight similar features among the gamma irradiated and H_2O_2 solution-submerged samples, while differing slightly from the reference sample.

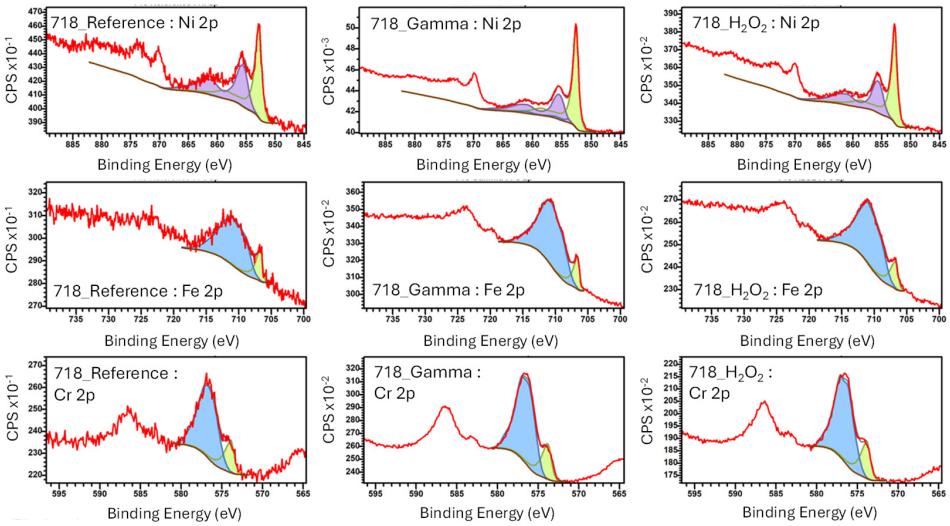


Figure 25: High resolution XPS spectra of Inconel 718 samples. From right to left: as-received, irradiated up to 2.2 MGy in water and submersed for 28 days in a 1 mM solution of H_2O_2. The fitting of the 2p peaks for nickel in its metallic state (green) and in the form of oxides (blue) is presented in the upper row. The fitting of the 2p peaks for iron in its metallic state (green) and in the form of oxide (blue) is presented in the central row. The fitting of the 2p peaks for chromium in its metallic state (green) and in the form of oxide and hydroxides (blue) is presented in the central row.

The extent of Cr oxidation seems to be unchanged over the three Inconel 718 sample of **Figure 25**. The Irradiated and the H_2O_2 solution-exposed samples present 3 and 2.5% more Hematite than the reference one, respectively. Nickel content seems to be the most affected by the experiments, varying from 51% of metallic Ni, 1% of NiO and 48% of $NiOH_2$ on the reference sample, to 59.8% metallic Ni, 4.9% NiO and 35.3% of $NiOH_2$ on the irradiated sample. The surface composition of the sample submerged in the H_2O_2 solution is 57% metallic Ni, and 43% $NiOH_2$. Due to the complexity of deconvoluting NiO and $NiOH_2$ overlapping peaks, it is however not possible to exclude the presence of nickel oxide. As a result of both irradiation and submersion in 1 mM H_2O_2 solution, metallic Ni and Fe oxide (i.e., Hematite) contents on the Inconel 718 samples surfaces are larger. However, strong signals for metallic Ni, Fe and Cr are identified in all the samples, suggesting surface oxide scales in the order of nm and differences between reference and irradiated or H_2O_2-treated samples within 1 nm.

Similarly to Inconel 718, also the XPS spectra of Inconel X-750 samples, shown in **Figure 26**, present only minor differences between as-received and both irradiated and H_2O_2-treated samples.

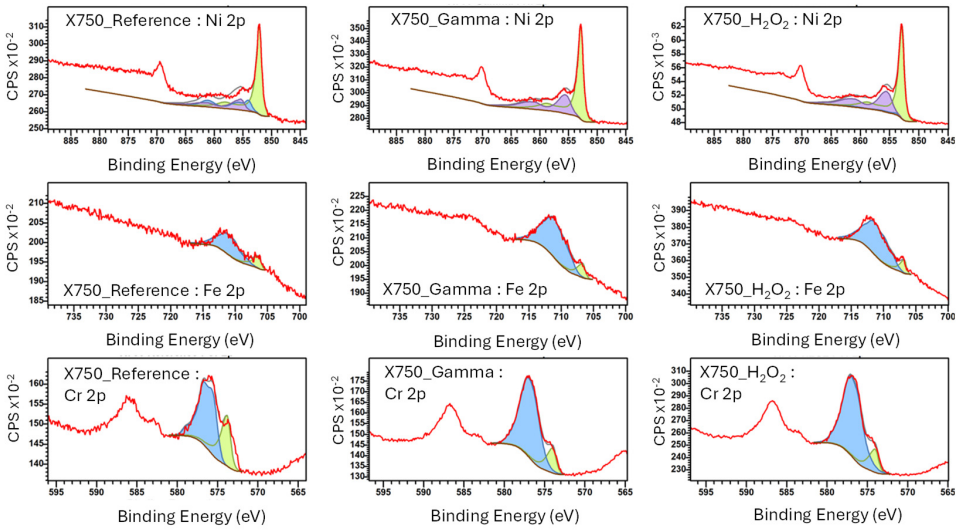


Figure 26: High resolution XPS spectra of Inconel X750 samples. From right to left: as-received, irradiated up to 2.2 MGy in water and submersed for 28 days in a 1 mM solution of H_2O_2. The fitting of the 2p peaks for nickel in its metallic state (green) and in the form of oxides (blue) in presented in the upper row. The fitting of the 2p peaks for iron in its metallic state (green) and in the form of oxide (blue) is presented in the central row. The fitting of the 2p peaks for chromium in its metallic state (green) and in the form of oxide and hydroxides (blue) is presented in the central row.

From the high-resolution XPS spectra of the Inconel X-750 samples shown in **Figure 26**, together with their deconvolutions, the fraction of metallic Ni remains nearly the same for both the as-received specimen and the sample exposed to H_2O_2, whereas it is approximately 6 % higher in the irradiated one. In contrast, the proportions of nickel oxide and hydroxide vary between the reference and the irradiated/H_2O_2-treated samples, though their quantification is challenging, as previously discussed for Inconel 718. Both Fe and Cr exhibit higher relative amounts in their oxidized states (i.e., around 10 % for Fe and 16–17 % for Cr) in the irradiated and H_2O_2-treated samples compared with the as-received material. As observed for the other alloys, the X-750 samples also display pronounced metallic signals, indicating that the overall oxide thickness is in the nm range, while differences between samples likely remain under 1 nm.

XPS investigation of Zircaloy-2 samples highlights virtually no difference between reference and both irradiated and H_2O_2-treated samples, as shown in the high-resolution spectra of **Figure 27.** After deconvoluting all the spectra, the samples display a relative percentage of ZrO_2 above 95 %, while just above 4%, is attributable to metallic Zr. The surface oxides scale seems thicker than the previous materials, reasonably around the detection limit for bulk signal pickup of 5 nm, for all the Zircaloy-2 samples.

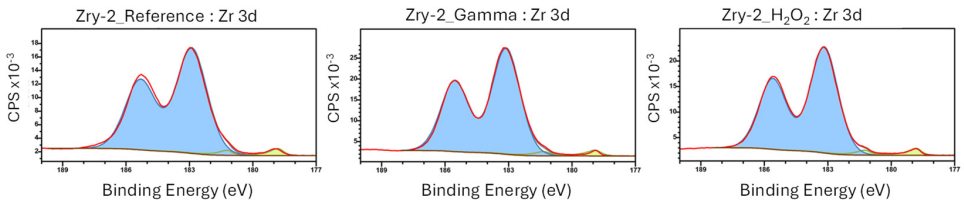


Figure 27: High resolution XPS spectra of Zircaloy-2 samples. From left to right: the fitting of the 3d peaks for zirconium in its metallic state (green) and in the form of oxide (blue) for the as-received, irradiated up to 2.2 MGy in water and submersed for 28 days in a 1 mM solution of H_2O_2.

Only limited differences concerning the relative proportions of metallic species, oxides, and hydroxides present at the surface of as-received, irradiated, and H_2O_2-treated samples are therefore revealed by the XPS. Nonetheless, signals corresponding to the metallic state remain consistently detectable across all samples, confirming the presence of very thin (i.e., nanometers scale range) oxide layers on the surfaces of the examined alloys both prior to and following irradiation or immersion in the 1 mM H_2O_2 solution. The XPS findings therefore do not support the hypothesis of alloy oxidation as the main cause of lowered H_2O_2 contents in the solution containing metallic samples after irradiation.

5.2.4.3 Electrochemical Impedance Spectroscopy

Given the nanoscale thickness of the surface oxides, achieving precise quantitative analysis is challenging with XPS. Therefore, the samples have been investigated employing electrochemical impedance spectroscopy, with the aim of disclosing the actual thicknesses of the surface oxide scale with a fast and scalable method. In fact, during EIS, the impedance and phase responses are collected over a broad frequency range and fitted using equivalent-circuit models. The capacitance extracted from EIS fitting is then used to estimate the thickness of the dielectric oxide layer by using the parallel plate approximation, as later explained.[88], [89], [90]. The EIS measurements were carried out on samples as received, after γ-irradiation (2.2 MGy) and H_2O_2-treated for 28 days. The results, shown in **Figure 28-31** and **Table 3**, are presented as Nyquist and Bode plots.

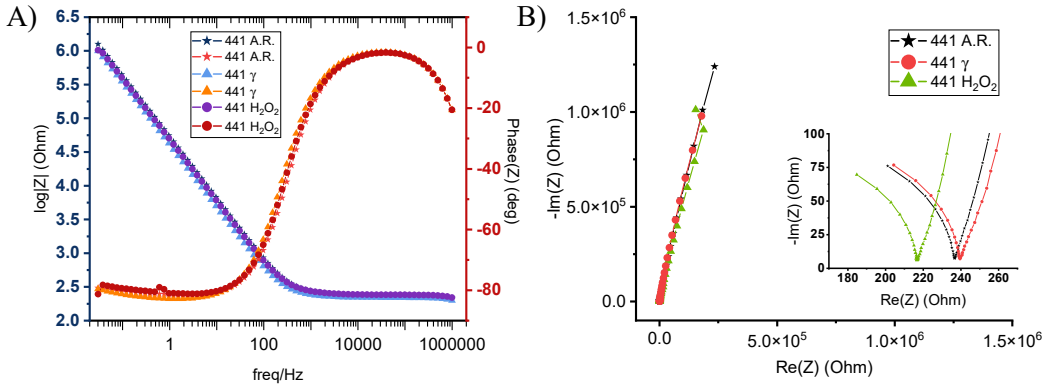


Figure 28: Bode plot (A) and Nyquist diagram (B) of as-received (A.R.), γ-irradiated (2.2 MGy) and H_2O_2-treated AISI 441 samples. The Nyquist diagram (B) also contains a magnification of the first point collected during the EIS investigation.

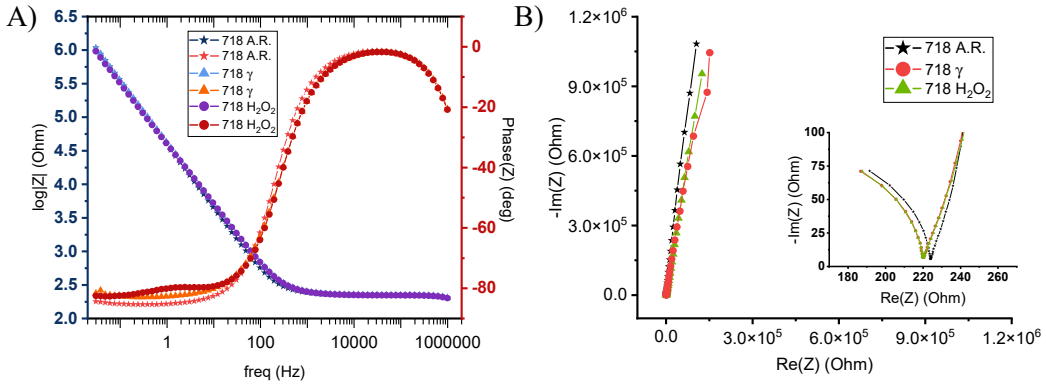


Figure 29: Bode plot (A) and Nyquist diagram (B) of as-received (A.R.), γ-irradiated (2.2 MGy) and H_2O_2-treated Inconel 718 samples. The Nyquist diagram (B) also contains a magnification of the first point collected during the EIS investigation.

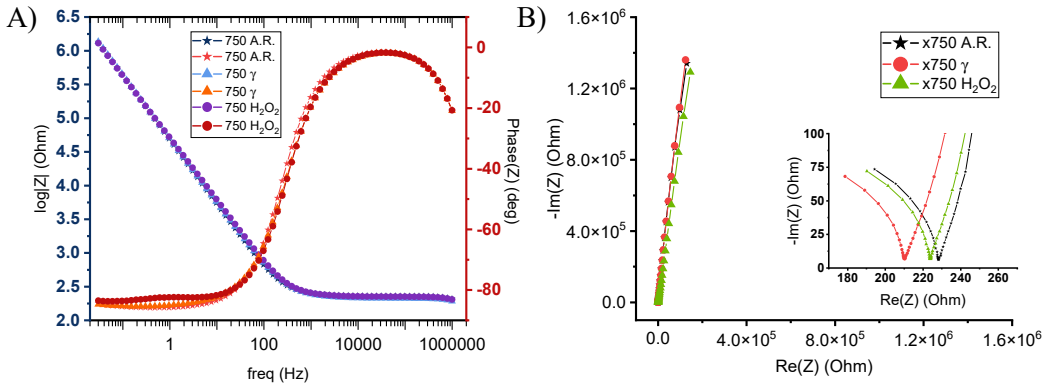


Figure 30: Bode plot (A) and Nyquist diagram (B) of as-received (A.R.), γ-irradiated (2.2 MGy) and H_2O_2-treated Inconel X750 samples. The Nyquist diagram (B) also contains a magnification of the first point collected during the EIS investigation.

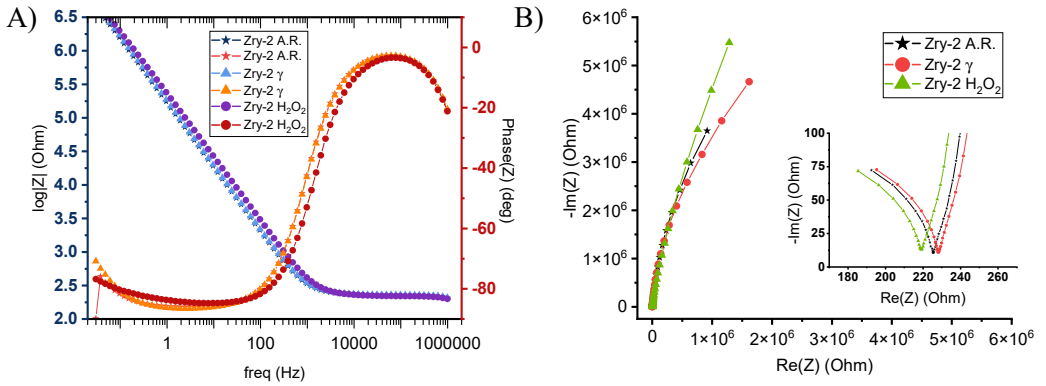


Figure 31: Bode plot (A) and Nyquist diagram (B) of as-received (A.R.), γ-irradiated (2.2 MGy) and H_2O_2-treated Zircaloy-2 samples. The Nyquist diagram (B) also contains a magnification of the first point collected during the EIS investigation.

The EIS spectra presented in **Figure 28-31** indicate a predominantly capacitive response for all the investigated samples, as shown by the Bode plots, where the phase angle remains between 0° and -90° and approaches strongly negative values over a broad frequency range. In parallel, |Z| increases towards low frequencies without reaching a clear resistive plateau. This behaviour is also reflected in the Nyquist plots, which generally display steep, near-vertical branches rather than fully developed semicircular arcs. Such a response suggests that, for both Fe- and Ni-based alloys, the impedance is dominated by passive-film and interfacial capacitive contributions, while a finite charge-transfer resistance is not resolved within the investigated frequency range. The impedance spectra were therefore analysed by equivalent circuit fitting rather than by extracting capacitance at a single frequency. For AISI 441, Inconel 718, Inconel X-750 and 316L stainless steel, the spectra were adequately represented by an $R_s - \mathrm{CPE}$ circuit, since R_{ct} could not be resolved reliably and attempts to include a parallel resistance led to non-physical or poorly constrained values. In these cases, the fitted CPE coefficient Q was

used as an approximation of the effective capacitance, justified by the high CPE exponent values, which indicate near-capacitive behaviour. In contrast, the Zircaloy-2 spectra displayed a resolvable resistive contribution and were fitted using an $R_s - (R_{ct} \parallel \text{CPE})$ circuit. For these samples, the CPE parameters were converted into an effective capacitance using the Brug relation. The oxide thickness, reported in **Table 3**, was then estimated from the resulting capacitance using the parallel-plate approximation. The small deviations observed at the highest frequencies, including the V-shaped inductive loop in the Nyquist plots reproducible among all the samples, were attributed to instrumental and cell-related artefacts, such as wiring, contacts, fixture inductance. Therefore, these high-frequency artefacts were excluded from the fitting procedure. This approach is consistent with standard EIS practice, where equivalent-circuit interpretation should be restricted to the frequency region in which the selected circuit elements have physical meaning[91].

Table 3: Surface oxide estimation *d*, and relative uncertainty *u(d)* in nm, based on the EIS investigation and effective capacitance approximation through equivalent circuit fitting.

	A.R.		**γ-irradiated**		**Submerged in H_2O_2**	
	d (nm)	**u(d)**	**d (nm)**	**u(d)**	**d (nm)**	**u(d)**
AISI 441	0.91	0.23	1.04	0.26	1.20	0.30
Inconel 718	0.97	0.24	0.97	0.24	0.91	0.23
Inconel X-750	1.19	0.29	1.19	0.29	1.20	0.30
Zircaloy-2	4.60	1.15	4.35	1.09	5.34	1.33

The surface oxide estimations shown in **Table 3**, calculated from impedance data collected through EIS, seem to be in reasonable agreement with the observation made from the XPS spectra. AISI 441, and Inconel alloys are all characterized by very thin (i.e., a nanometer or sub-nanometer-thick) oxide layers, with sub-nanometer differences between samples matching remarkably well the XPS data, especially for both nickel-based alloys. As suggested by the analysis of the XPS spectra for Zircaloy-2 samples, the calculated surface oxides are thicker than for the other materials.

5.2.4.4 Analysis of Metal Ions in the Aqueous Phase

In addition to the surface characterizations discussed above, the dissolution of species potentially reactive towards H_2O_2 was studied. The aqueous solution in which the samples, both as-received and ground, were irradiated up to 2.2 MGy were analysed using ICP-MS. The investigation was aimed at all the elements found in the generic composition of the alloys (see **Table 1**) but only those found in detectable quantities are reported in **Table 4**.

Table 4: Concentration (ppb) of the elements identified in the solutions in which both as-received and ground alloys samples were γ-irradiated up to 2.2 MGy. UDL stands for "Under Detection Threshold". Those composition elements not detected for any of the samples have been omitted from the table.

	Ti-48		**Fe-57**		**Ni-60**		**Nb-93**	
	Conc. (ppb)	**SD**	**Conc. (ppb)**	**SD**	**Conc. (ppb)**	**SD**	**Conc. (ppb)**	**SD**
441 A.R.	UDL		26	1	UDL		UDL	
718 A.R.	3	1	5	2	44	1	UDL	
x750 A.R.	16	1	UDL		61	1	10	1
Zry2 A.R	UDL		UDL		0.5	0.1	UDL	
441 ground	0.9	0.7	40	1	1.3	0.1	UDL	
718 ground	4	1	4	1	43	1	UDL	
x750 ground	27	1	UDL		78	2	23	1
Zry2 ground	UDL		2	1	1.2	0.1	UDL	

As can be seen in **Table 4**, only 4 of the 12 elements measured in the irradiated solutions were found in detectable quantities. Aluminium is an exception, as it was found in high concentrations (above 500 ppb) in all samples. Nevertheless, it was omitted from **Table 4** since it is arguably considered a contamination due to the dissolution of the septa's lining by HNO_3 formed by the radiolysis of humid air in the headspace[92]. The ground samples of AISI 441, Inconel X-750 and Zircaloy-2 contain marginally higher levels of the detected elements than the corresponding as-received samples. The observation is consistent with a larger solution–metal interfacial area and a less protective surface oxide on the ground specimens. Notably, Inconel 718 displays no such difference, with the measured concentrations being comparable for both as-received and ground conditions. The AISI 441 specimens show the highest Fe concentrations among the investigated materials, and Fe(II) is known to react readily with hydrogen peroxide[93]. The Fe content in Inconel 718 is second only to that in AISI 441, while its Ni content is second only to that in Inconel X-750. The ICP-MS results are based solely on the liquid phase collected from the irradiation vials (after dilution with HNO_3), so any precipitated or adsorbed material was presumably not accounted for in the analysis. This limitation may be particularly important for Fe^{2+}, which reacts rapidly with H_2O_2 and can form insoluble Fe(III)-hydroxides and oxide. Conversely, nickel released to solution is typically

present as Ni^{2+} and requires strongly oxidizing conditions to undergo further oxidation[94], [95], [96], whereas dissolved titanium and niobium predominantly exist as Ti(IV) and Nb(V) hydrolyzed species, respectively, which correspond to their highest stable oxidation states in aqueous environments[94], [97], [98] and are therefore not expected to undergo further oxidation by radiolytically generated H_2O_2. Nevertheless, a clear correlation is observed: alloys with higher Fe levels in solution display reduced H_2O_2 concentrations under irradiation at higher doses. Given the high stability of H_2O_2 in unirradiated solutions in contact with the same alloys, it can be concluded that the dissolution of Fe responsible for the consumption of H_2O_2 in the irradiated systems must be driven by the radiation. This effect could either be attributed to the action of short-lived aqueous radiolysis products such as the hydroxyl radical or to the direct absorption of the radiation by the metal/metal oxide.

5.3 In-Situ Electrochemical Investigation of 316L in Water Solutions under Intermittent γ Irradiation

5.3.1 Oxidative Response under Intermittent γ Irradiation at Different Dose-Rates

Intermittent gamma irradiation was performed at time intervals of 120 seconds while monitoring the electrical response of the 316L sample at the OCP before irradiation (i.e., chrono amperometry measurement). Two different electrolytic solutions (0.15 mM H_2O_2, 0.125 M Na_2SO_4, and 0.15 mM H_2O_2, 0.125 M Na_2SO_4, 0.2 M tert-butanol, respectively) and three different γ dose rates (blue 0.25, red 0.46 and green 0.57 Gy/s) were tested. The tert-butanol was added as it is a well-known hydroxyl radical scavenger with a rate constant of $6.0 \cdot 10^8$ M^{-1} s^{-1}[99]. Possible differences in the electrochemistry of the two systems could be attributed to hydroxyl radical scavenging. While the original appearance of the unredacted dataset is shown in **Figure 32** and **Figure 33**, the data presented in **Figure 34** and **Figure 35**, which form the basis for the following discussion, have been baseline-corrected to compensate for the large OCP drift, induced by H_2O_2 build-up during the measurements, as later explained.

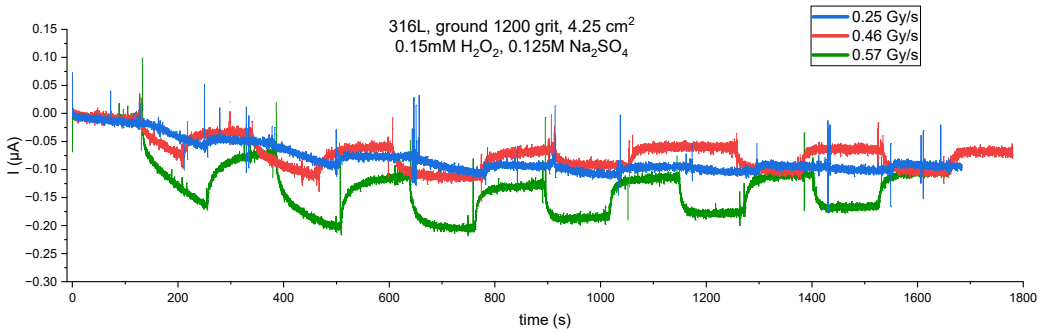


Figure 32: Chrono amperometry measurements of AISI 316L steel in 0.15 mM H_2O_2, 0.125 M Na_2SO_4 electrolytic solution under intermittent γ irradiation at different dose rates, 0.25 Gy/s (blue), 0.46 Gy/s (red) and 0.57 Gy/s (green). No baseline correction or data manipulation was performed.

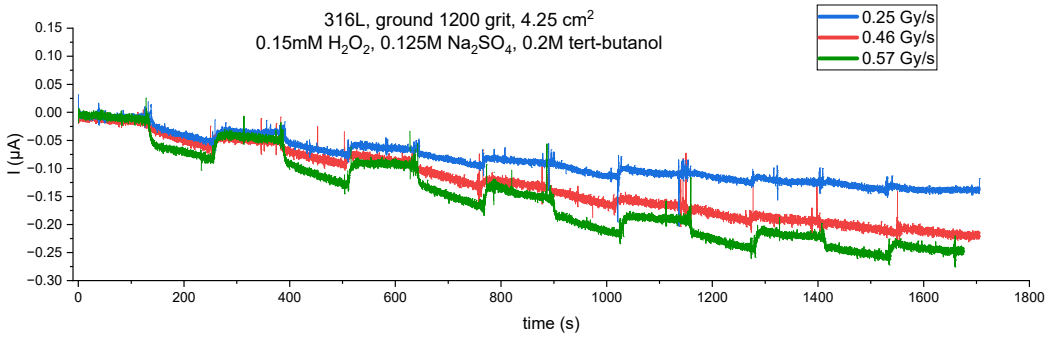


Figure 33: Chrono amperometry measurements of AISI 316L steel in 0.15 mM H_2O_2, 0.125 M Na_2SO_4 and 0.2 M t/BuOH electrolytic solution under intermittent γ irradiation at different dose rates, 0.25 Gy/s (blue), 0.46 Gy/s (red) and 0.57 Gy/s (green). No baseline correction or data manipulation was performed.

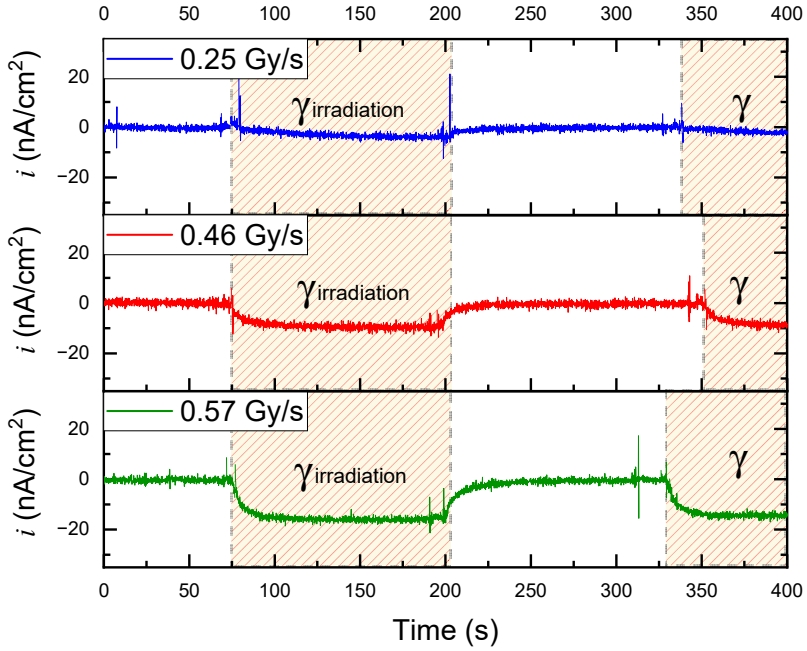


Figure 34: Chrono amperometry measurements of AISI 316L steel in 0.15 mM H_2O_2, 0.125 M Na_2SO_4 electrolytic solution under intermittent γ irradiation at different dose rates. From top to bottom: 0.25 Gy/s (blue), 0.46 Gy/s (red) and 0.57 Gy/s (green). Only a representative segment of the measurement, is presented for clarity. The presented segment was baseline-corrected by subtracting the OCP drift to compensate for gradual changes of the OCP during the measurement.

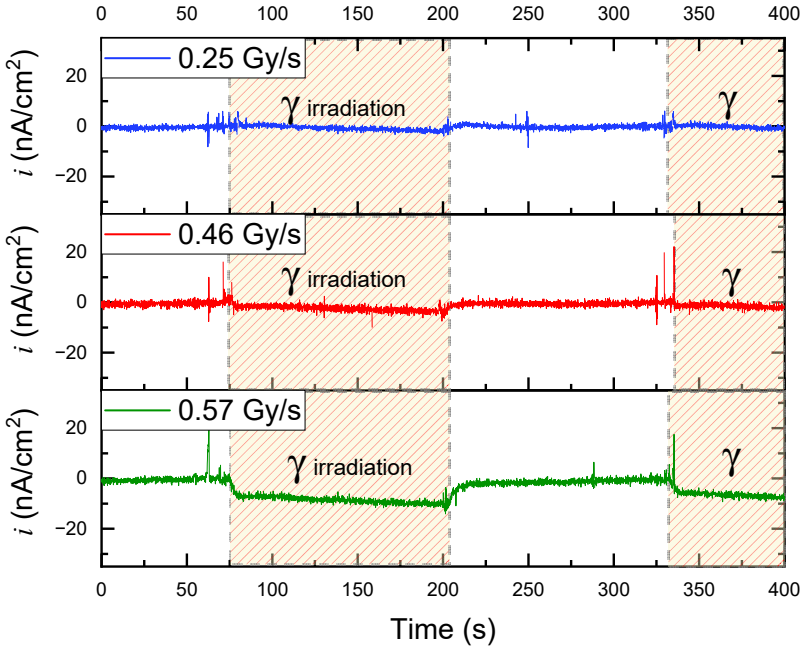


Figure 35: Chrono amperometry measurements of AISI 316L steel in 0.15 mM H_2O_2, 0.125 M Na_2SO_4 and 0.2 M t-BuOH electrolytic solution under intermittent γ irradiation at different dose rates. From top to bottom: 0.25 Gy/s (blue), 0.46 Gy/s (red) and 0.57 Gy/s (green). Only a representative segment of the measurement is presented for clarity. The presented segment was baseline-corrected by subtracting the OCP drift to compensate for gradual changes of the OCP during the measurement.

As can be seen in **Figure 34** and **Figure 35**, all the CA measurements respond to γ irradiation with an immediate increase of the current flowing in the cell when the system is irradiated. The electrical response is built up with the dose rate over a span of c.a. 5 seconds from the moment the chamber has started moving to the irradiation zone (i.e., from the cold to the hot zone) and it goes back to a rest value in a span of 6 to 7 seconds, while the chamber is lifted from the irradiation zone to the upper resting position (i.e., from the hot to the cold zone). The observed current change was negative for all the investigated dose rates and solutions, indicating an overall negative current balance associated with reduction reactions happening at the WE under gamma irradiation. Consequently, OCP shifted toward more positive values under irradiation, reflecting a noble (oxidative) displacement of the corrosion potential, followed by a shift back to less positive values as soon as the irradiation period is terminated. Similar oxidative response was reported by Wang et al., during proton irradiation of 316L under simulated PWR conditions[100]. As reported in **Table 5** and **Table 6**, and graphically represented in **Figure 36** the average amplitude of the electrical response varies proportionally with the dose rate and is generally smaller for the solution containing tert-butanol. The presented values have been calculated on cycles number three to five for each sample.

Table 5: Averaged current density variation under intermittent γ irradiation at different dose rates of 316L samples in the 0.15 mM H_2O_2 and 0.125 M Na_2SO_4 solution.

Dose Rate (Gy/s)	**Δi (nA/cm^2)**	**STD dev. (nA/cm^2)**
0.25	-2.6	0.6
0.46	-8.2	1.0
0.57	-14.5	0.7

Table 6: Averaged current density variation under intermittent γ irradiation at different dose rates of 316L samples in the 0.15 mM H_2O_2, 0.125 M Na_2SO_4 and 0.2 M t-BuOH solution.

Dose Rate (Gy/s)	**Δi (nA/cm^2)**	**STD dev. (nA/cm^2)**
0.25	-1.2	1.0
0.46	-2.1	1.0
0.57	-8.8	1.6

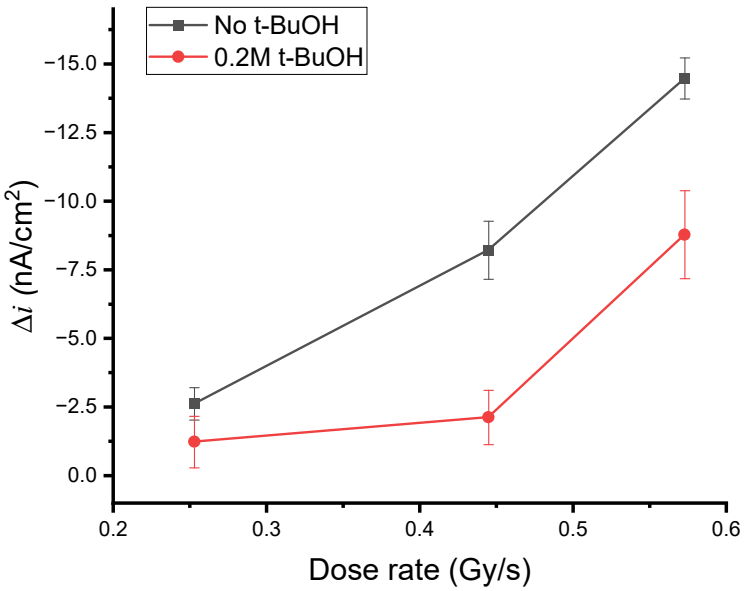


Figure 36: Averaged amplitude of current density response vs dose rate for the 316L samples in the 0.15mM H_2O_2 and 0.125 M Na_2SO_4 solution (black, square symbols) and in the 0.15mM H_2O_2, 0.125 M Na_2SO_4 and t-BuOH solution (red, round symbols.

The amplitude of the intermittent electrical response measured by CA increases almost linearly with the dose rate for the samples irradiated in the solution without tert-butanol, as shown in **Figure 36**. At the two lowest dose rates, the current increase in the 0.2 M tert-butanol solution is very small while for the highest dose rate, there is a significant current increase, which is

however 40% smaller than without tert-butanol (i.e., -8.8 vs -14.5 nA/cm^2). Hence, the electric current response of the alloy shows responsiveness to hydroxyl radical scavenging. Given the intermittent nature of the electrical response and the fact that the amplitude of this response is affected by the dose rate as well as the presence of a well-known hydroxyl radical scavenger in the solution, the most obvious conclusion is that the response is induced by radiolytically produced hydroxyl radicals. Hydroxyl radicals are known to be strong oxidants and H-atom abstractors, and they often add to electron-rich systems. Hydroxyl radicals have also been shown to have fairly high affinity for metal oxides. This has been demonstrated experimentally as well as in computational studies[101]. The interactions between hydroxyl radicals and the surface of the WE change the reactivity of the surface intermittently. However, as soon as the irradiation stops, these changes are reverted. In their experiments under proton irradiation, beside an increased oxidative response at higher fluxes, Wang et al. also observed that the oxidative response was stronger at lower (i.e., 29 mbar) than at higher (i.e., 390 mbar) H_2 partial pressure at 300 °C[100]. Similarly to what we report here, the reason for their observed difference in oxidative response could be scavenging of hydroxyl radicals by H_2. It should be noted that addition of H_2 is used to control the concentration of the oxidants H_2O_2 and O_2 through the formation of $H^\bullet$ in the reaction $H_2 + HO^\bullet \rightarrow H^\bullet + H_2O$. Hence, H_2 is also an efficient scavenger of hydroxyl radicals ($k = 4.27 \cdot 10^8$ $M^{-1}s^{-1}$ at 25 °C[102]. Also, as the fairly large standard deviation values reported in **Table 6** may suggest, and as visible in **Figure 32** and **Figure 33**, the electrical response under γ irradiation gets weaker with increasing number of irradiation cycles, especially for the 0.2 M t-BuOH solutions irradiated at lower dose rates. A progressively less intense oxidative response with ageing (i.e., thermal and cumulative fluence) was reported by Wang et al. as well. Their explanation relied on an induced evolution of the electrochemical properties of the surface[100].

5.3.2 Effect of Intermittent γ Irradiation on Hydrogen Peroxide Build-up and Corrosion Potential

Scavenging of hydroxyl radicals (and $H^\bullet$) also affects the hydrogen peroxide concentration. Hydroxyl radicals react directly with hydrogen peroxide and indirectly by reacting with radiolytically produced H_2 to produce $H^\bullet$, which in turn reacts with H_2O_2 producing more hydroxyl radicals. By reducing the steady-state concentrations of species that consume hydrogen peroxide, the steady-state H_2O_2 concentration will increase. The hydrogen peroxide concentration in the electrolytic solutions was 0.15 mM before irradiation and remained unchanged both after 1.5 hours of resting time and after the repeated EIS and LSV. The concentrations after the intermittent irradiation are reported in **Table 7** and **Table 8**.

Table 7: Variations of H_2O_2 concentration after intermittent γ irradiation at different dose rates of 316L samples in the 0.15mM H_2O_2 and 0.125 M Na_2SO_4 solution.

Dose Rate (Gy/s)	Δ H_2O_2 (μM)	Δ H_2O_2 (%)
0.25	+0	0%
0.46	+2	+1%
0.57	+10	+7%

Table 8: Variations of H_2O_2 concentration after intermittent γ irradiation at different dose rates of 316L samples in the 0.15mM H_2O_2, 0.125 M Na_2SO_4 and 0.2 M t-BuOH solution.

Dose Rate (Gy/s)	Δ H_2O_2 (μM)	Δ H_2O_2 (%)
0.25	+56	+37%
0.46	+73	+49%
0.57	+86	+57%

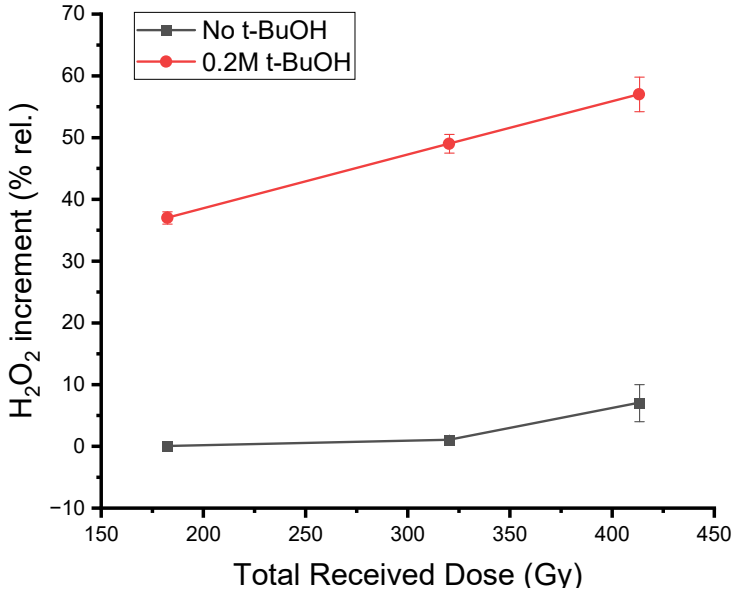


Figure 37: Hydrogen peroxide content increase (in % relative to the original concentration) vs total received dose for the 316L samples in the 0.15mM H_2O_2 and 0.125 M Na_2SO_4 solution (black, square symbols) and in the 0.15mM H_2O_2, 0.125 M Na_2SO_4 and t-BuOH solution (red, round symbols).

From **Table 7** and **Table 8** and **Figure 37** it is obvious that the effect of the intermittent γ irradiation on the H_2O_2 concentration is visibly stronger in the solution containing 0.2 M of tert-butanol than on the solution without. This is well in line with the expected effect of adding a hydroxyl radical scavenger[103]. The total increase in H_2O_2 concentration appears to depend linearly on the absorbed dose. Despite H_2O_2 being therefore largely available, the electrical

response in the form of current change of the samples in the 0.2 M tert-butanol solution is remarkably smaller than in the scavenger-free solution (see **Table 5, Table 6** and **Figure 36**) further supporting the hypothesis of hydroxyl radical-mediated reactions as the cause of the larger electrical current. The increase in H_2O_2 concentration in the solutions without tert-butanol is virtually insignificant. This can be attributed to fact that the initial H_2O_2 concentration is close to the steady-state concentration of pure water.
The increase in H_2O_2 concentration drastically changes the characteristics of the electrolytic solution and thereby the OCP value. In **Table 9** and **Table 10** the increase, in millivolt, of the OCP at rest of the system after the intermittent γ irradiation is reported for both solutions at the three investigated dose rates and total doses.

Table 9: OCP variation after intermittent γ irradiation at different nominal dose rates and total doses received of 316L samples in the 0.15mM H_2O_2 and 0.125 M Na_2SO_4 solution.

Dose Rate (Gy/s)	Total Dose (Gy)	ΔOCP (mV)
0.25	180	+9
0.46	331	+10
0.57	410	+12

Table 10: OCP variation after intermittent γ irradiation at different nominal dose rates and total doses received of 316L samples in the 0.15mM H_2O_2, 0.125 M Na_2SO_4 and 0.2 M t-BuOH solution.

Dose Rate (Gy/s)	Total Dose (Gy)	ΔOCP (mV)
0.25	180	+19
0.46	331	+23
0.57	410	+28

From **Table 9** and **Table 10** we can see that the increase in OCP after the intermittent irradiation is significantly larger for the systems containing tert-butanol than for the systems without. This trend parallels the trend observed for the change in H_2O_2 concentration for the two systems. The shift in OCP toward more positive potentials (ennobling), driven primarily by changes in partial-current kinetics and passive film characteristics, such as the formation of a more uniform, continuous, thicker, or less defective oxide layer, appears to occur independently of the slightly elevated hydrogen peroxide concentrations observed in the system without tert-butanol. Such an evolution (passivation) of the surface is intrinsic of a stainless steel alloy and reasonably promoted by the presence of oxidants, in this case the original 0.15 mM of H_2O_2 in the electrolytic solution. Since this background shift of the OCP cannot be prevented or experimentally distinguished from the contribution of radiolytically produced hydrogen peroxide, the resulting OCP-radiolytically produced H_2O_2 relationship appears nonlinear, particularly for experiments in which the increase in H_2O_2 is small (e.g, 0.25 Gy/s

and 0.46 Gy/s irradiation without tert-butanol). As observed before, the magnitude of the electrical response under intermittent irradiation (i.e., the increased negative current) is proportional to the availability of HO•, suggesting that the cathodic processes occurring on the 316L surface are mediated by hydroxyl radicals.

To assess whether the observed shifts of the OCP values were solely due to the effect of increased H_2O_2 concentration, LSV measurements were carried out before and after intermittent irradiation at 0.57 Gy/s. The intermittent irradiation experiments were conducted under both CA and OCP conditions in separate measurements. Additional LSV measurements were performed before and after the chemical addition of H_2O_2 while continuously monitoring the OCP. The amount of H_2O_2 added was selected to reproduce the concentration measured after intermittent irradiation, as reported in **Table 7** and **Table 8**. Intermittent irradiation experiments were also performed under OCP conditions because, during CA, the working electrode was held at its pre-irradiation OCP. Since irradiation caused the OCP to shift in the positive direction, the working electrode was consequently cathodically polarized during irradiation. This imposed polarization could influence the electrochemical response to radiolytically generated oxidizing species. Measurements under OCP conditions were therefore included to assess the irradiation response without imposing this additional polarization. For this investigation another set of samples was used. The LSV graphs are shown in **Figure 38** and **Figure 39** for the solution without and with 0.2 M tert-butanol, respectively. The relevant data are summarized in **Table 11.**

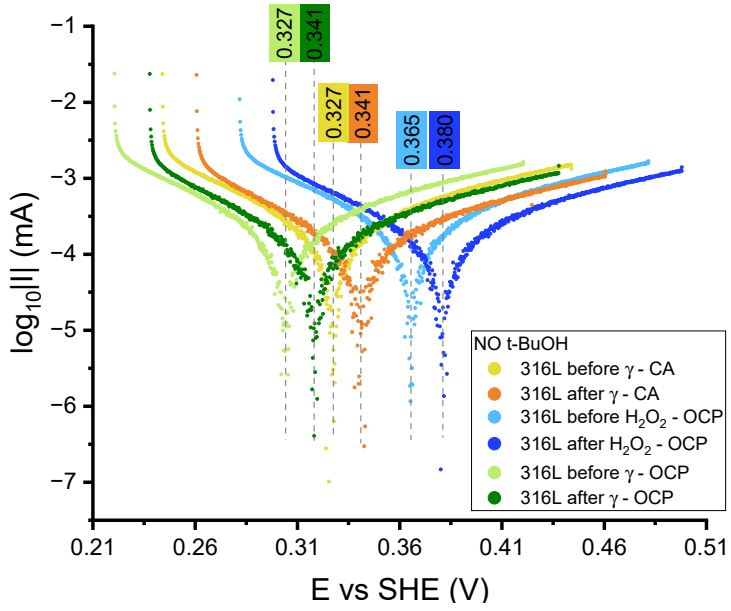


Figure 38: Linear Sweep Voltammetry of AISI 316L alloy in the 0.15mM H_2O_2 and 0.125 M Na_2SO_4 solution. Before (yellow) and after (orange) γ irradiation during CA, before (light blue) and after (dark blue) chemical addition of H_2O_2 during OCP and before (light green) and after (dark green) γ irradiation during OCP. The dose rate used for the γ irradiation was 0.57 Gy/s and the H_2O_2 was adjusted at 0.160 mM.

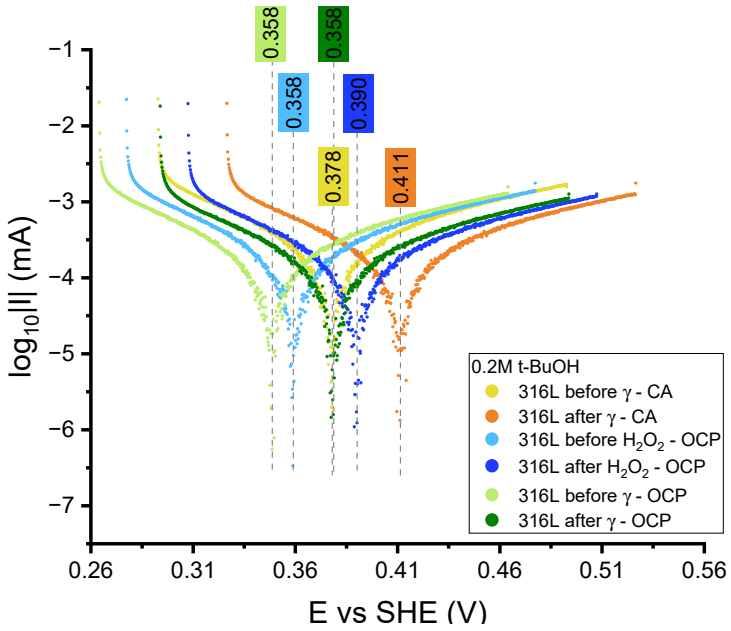


Figure 39: Linear Sweep Voltammetry of AISI 316L alloy in the 0.15mM H_2O_2 and 0.125 M Na_2SO_4 and 0.2 M t-BuOH solution. Before (yellow) and after (orange) γ irradiation during CA, before (light blue) and after (dark blue) chemical addition of H_2O_2 during OCP and before (light green) and after (dark green) γ irradiation during OCP. The dose rate used for the γ irradiation was 0.57 Gy/s and the H_2O_2 was adjusted at 0.236 mM.

Table 11: Hydrogen peroxide concentration variation and respective OCP shifts after gamma irradiation and chemical addition (during CA and OCP measurements) of H_2O_2. Data collected from the LSV measurements reported in **Figure 38** and **Figure 39**. The γ dose rate was 0.57 Gy/s.

Solution	**Δ H_2O_2 Chemically added (μM)**	**Δ OCP After H_2O_2 addition (OCP, mV)**	**Δ OCP After γ irradiation (CA, mV)**	**Δ OCP After γ irradiation (OCP, mV)**
No t-BuOH	+10	+15	+14	+14
0.2 M t-BuOH	+86	+32	+33	+31

As reported in **Table 11**, the chemical addition of H_2O_2 induces almost exactly the same OCP shift as measured for the intermittent irradiation. Observing both **Figure 38** and **Figure 39**, the LSV curves after irradiation and hydrogen peroxide addition seem to preserve their characteristics shapes, indicating no major changes in the properties of the surface. However, considering that the sample were tested shortly after grinding and that the alloy under investigation spontaneously grows a thin (from less than 1 to a few nm) Cr-rich protective film, even minuscules differences in term of uniformity or defectiveness of the surface oxides would affect its nobility and therefore contribute to the observed OCP shift.

5.3.3 Surface Modification after γ Irradiation and Hydrogen Peroxide Addition

To investigate the subtle but potentially significant evolution of the surface oxide layer, EIS measurements were performed on the samples shown in **Figure 38** and **Figure 39** before and after intermittent irradiation or exposure to H_2O_2 as shown in **Figure 40-44**.

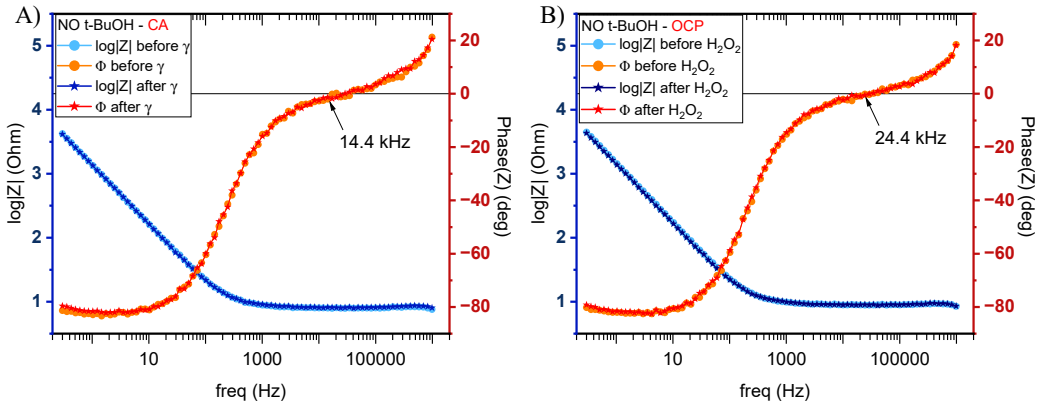


Figure 40: Bode representation of the EIS measurements of A) AISI 316L samples before and after intermittent γ irradiation at 0.57 Gy/s in 0.15 mM H_2O_2, 0.125 M Na_2SO_4 electrolytic solution while performing CA. B) AISI 316L samples before and after addition of H_2O_2 to the 0.15 mM H_2O_2, 0.125 M Na_2SO_4 electrolytic solution while monitoring the OCP.

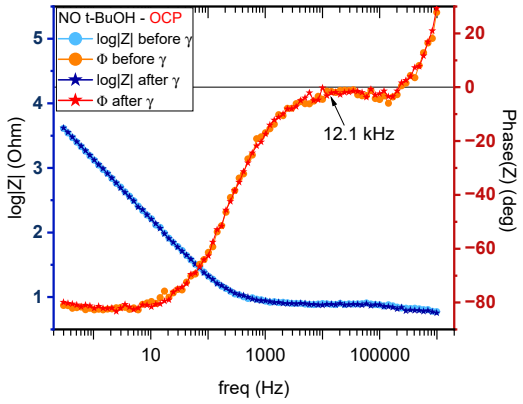


Figure 41: Bode representation of the EIS measurements of AISI 316L sample before and after intermittent γ irradiation at 0.57 Gy/s in 0.15 mM H_2O_2, 0.125 M Na_2SO_4 electrolytic solution while monitoring the OCP.

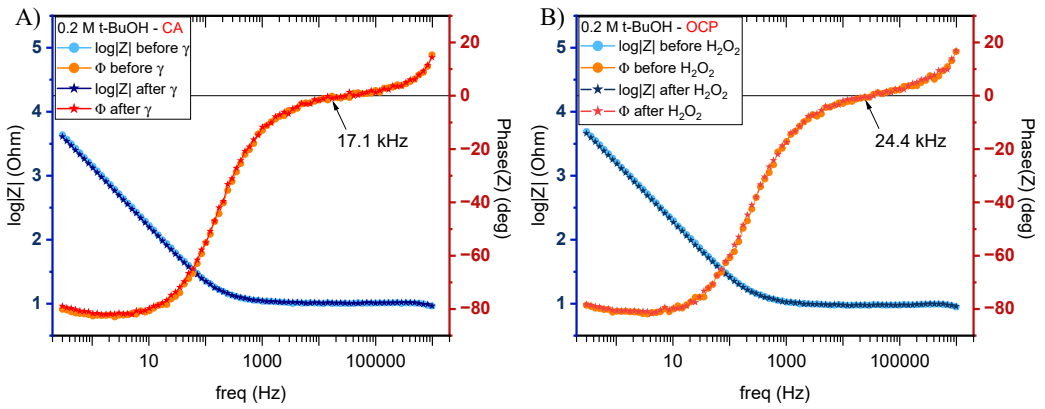


Figure 42: Bode representation of the EIS measurements of A) AISI 316L samples before and after intermittent γ irradiation at 0.57 Gy/s in 0.15 mM H_2O_2, 0.125 M Na_2SO_4, 0.2 M t-BuOH electrolytic solution. B) AISI 316L samples before and after addition of H_2O_2 to the 0.15 mM H_2O_2, 0.125 M Na_2SO_4, 0.2 M t-BuOH electrolytic solution.

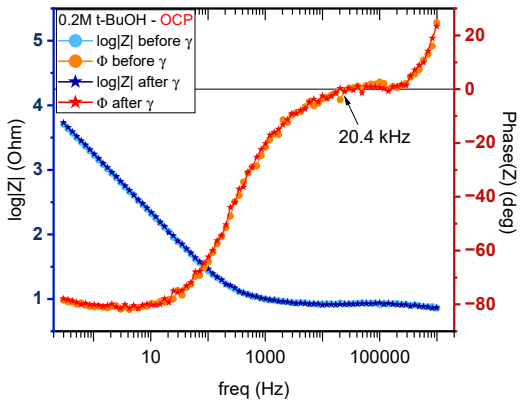


Figure 43: Bode representation of the EIS measurements of AISI 316L sample before and after intermittent γ irradiation at 0.57 Gy/s in 0.15 mM H_2O_2, 0.125 M Na_2SO_4 electrolytic solution while monitoring the OCP.

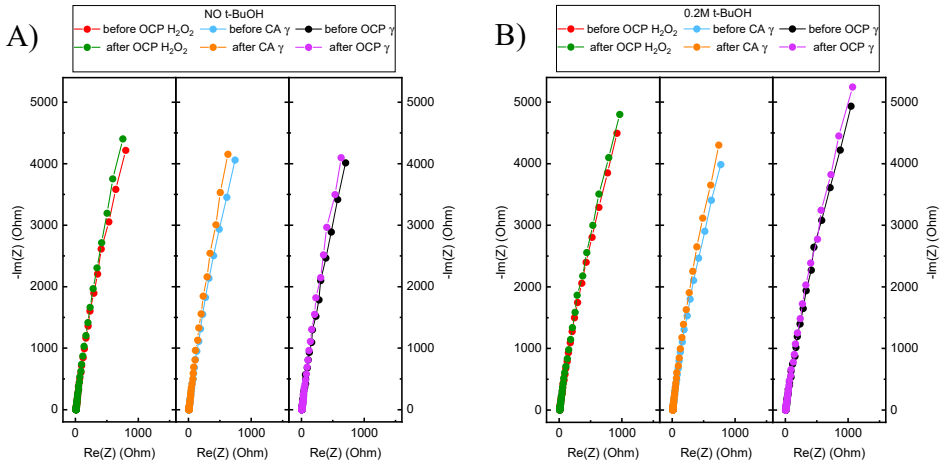


Figure 44: Nyquist representation of the EIS measurements of A) AISI 316L samples before and after intermittent γ irradiation at 0.57 Gy/s (blue and orange) and before and after H_2O_2 addition (green and red) in 0.15 mM H_2O_2, 0.125 M Na_2SO_4 electrolytic solution. B) AISI 316L samples before and after intermittent γ irradiation at 0.57 Gy/s (blue and orange) and before and after H_2O_2 addition (green and red) in 0.15 mM H_2O_2, 0.125 M Na_2SO_4, and 0.2 M electrolytic solution.

The EIS spectra presented in **Figure 40-44** are characterized by dominant capacitive behaviour for all investigated conditions. In the Bode plots, the phase angle remains between 0° and approximately -90° over most of the frequency range, indicative of passive-film and interfacial capacitive processes. A slight positive phase shift is observed at the highest frequencies (approximately 14-24 kHz), which is likely attributable to instrumental or wiring inductance rather than the electrochemical response of the system. Simultaneously, the impedance modulus increases continuously toward lower frequencies without reaching a plateau. Consistent with these observations, the Nyquist plots exhibit steep, nearly vertical branches rather than fully developed semicircular arcs, indicating a strongly capacitive response with non-ideal behaviour. The absence of a complete semicircle within the investigated frequency range suggests that the charge-transfer process is not fully resolved and that the associated charge-transfer resistance may be very large or located at frequencies lower than those measured.

The frequencies above 12 kHz were hence excluded from the equivalent circuit (EC) fitting because, as mentioned, they exhibited positive phase-angle values, which are non-physical for the electrochemical systems under investigation and are typically indicative of instrumental artifacts or limitations in high-frequency measurement accuracy. Since the spectra did not resolve a finite charge-transfer resistance within the measured frequency window, the spectra were fitted using an $R_s - CPE$ equivalent circuit. Although the CPE coefficient Q can be treated as a capacitance when the CPE exponent n is close to unity, direct conversion of Q into an oxide thickness produced few-angstrom values, which are physically unrealistic. This because the fitted CPE response is not solely associated with the dielectric capacitance of a

compact oxide layer, but also includes contributions from interfacial pseudo-capacitance, surface roughness, distributed passive-film properties, and double-layer effects[88], [89], [90]. Consequently, absolute oxide-scale thicknesses were not reported for these samples. Instead, the fitted Q and n values were used to compare the evolution of the passive interfacial response. The equivalent-circuit fitting parameters are summarized in **Table 12**.

Table 12: Parameters of the equivalent circuit fitted to the EIS spectra of AISI 316L alloy samples before and after intermittent γ irradiation and hydrogen peroxide addition. Q, in Fs^{n-1} is the CPE coefficient associable with the capacitance and n is the CPE exponent, dimensionless. The quality of the fitting was assessed through the *normalized* X^2 value which was consistently below 3%.

	Before γ irradiation (CA)		**After γ irradiation (CA)**		**Before H_2O_2 addition (OCP)**		**After H_2O_2 addition (OCP)**		**Before γ irradiation (OCP)**		**After γ irradiation (OCP)**	
	Q (Fs^{n-1})	**n (-)**	**Q (Fs^{n-1})**	**n (-)**	**Q (Fs^{n-1})**	**n (-)**	**Q (Fs^{n-1})**	**n (-)**	**Q (Fs^{n-1})**	**n (-)**	**Q (Fs^{n-1})**	**n (-)**
No t-BuOH	$1.35 \cdot 10^{-4}$	0.922	$1.34 \cdot 10^{-4}$	0.922	$1.30 \cdot 10^{-4}$	0.925	$1.24 \cdot 10^{-4}$	0.928	$1.37 \cdot 10^{-4}$	0.922	$1.36 \cdot 10^{-4}$	0.924
0.2 M t-BuOH	$1.36 \cdot 10^{-4}$	0.925	$1.25 \cdot 10^{-4}$	0.934	$1.20 \cdot 10^{-4}$	0.913	$1.14 \cdot 10^{-4}$	0.915	$1.10 \cdot 10^{-4}$	0.910	$1.05 \cdot 10^{-4}$	0.913

As visible in **Table 12**, all the samples present values very close to each other before/after testing, indicating that the overall electrochemical character of the interface is largely preserved. Nevertheless, all samples consistently exhibit a small decrease of the Q value after both irradiation and H_2O_2 addition. Since Q represents the effective pseudo-capacitive response of the interface in the adopted $R_s - \text{CPE}$ model, this decrease suggests a modest reduction in effective interfacial capacitance, which is consistent with a slightly more blocking interface, which may result from limited thickening, densification, or improved uniformity. The CPE exponent n remains close to 0.91–0.93 for all samples and changes only marginally after treatment. This indicates that the degree of frequency dispersion, and therefore the level of interfacial heterogeneity or non-ideality, is broadly maintained. The slight increase in n observed in most treated samples may indicate a marginally more ideal capacitive response, possibly associated with a more homogeneous or more compact passive interface. Overall, the post-irradiation EIS responses indicate that the final passive-film states were modified only slightly and to a comparable extent under both CA and OCP mode. Moreover, the EIS being also similar to those post chemical addition of H_2O_2, it could be that the OH-sensitive interfacial perturbation is predominantly reversible or insufficient to cause a substantial persistent change in the passive film compared to the continuous exposure to H_2O_2 at concentrations of 0.15 mM or higher and O_2 corresponding to air-saturation, as the minor, stable modifications can be explained by the sole H_2O_2. Therefore, the progressively weaker electrical response observed upon repeated irradiation, similarly to the behaviour reported by Wang at al.[100] may be regarded as a further indication of the changes in the electrochemical properties of the oxide film over time. Without tert-butanol, spontaneous passivation combined with the relatively slow accumulation of H_2O_2 only slightly decreases the reactivity of the surface toward hydroxyl radicals. As a result, the current response exhibits only a minor

decrease after successive irradiation cycles. In contrast, when tert-butanol is present, the more rapid accumulation of H_2O_2 promotes a stronger and faster modification of the surface. Consequently, the surface becomes progressively less reactive toward radiolytic species, leading to a much more pronounced decline in the current response after only a few irradiation cycles.

6 Conclusion

This thesis covers several aspects of radiation-induced phenomena in materials relevant to nuclear power systems, focusing on the effects of direct gamma irradiation and gamma-induced radiolysis on polymers, water, and alloys used in light water reactors, probing the accuracy of H_2O_2 as a chemical surrogate for radiolysis of water.

The study on the influence of septa materials on steady-state H_2O_2 during irradiation of air-saturated pure water (**Chapter 5.1**) was motivated by experimental inconsistencies and reproducibility issues. Aluminium, PTFE, and silicone rubber septa were evaluated with either the headspace or the solution facing the vial interior. When silicone rubber faced the headspace, H_2O_2 concentrations dropped by nearly 90% at absorbed doses above 14.8 kGy. In all other configurations (i.e., aluminium or PTFE facing the headspace, and all materials facing the solution) H_2O_2 increased slightly with dose at high doses. This behavior is attributed to fast reactions between O_2 and Si- and C-centered radicals in the silicone septum, depleting O_2 in the aqueous phase. Because O_2 is a precursor for radiolytic H_2O_2, its depletion lowers the steady-state H_2O_2 concentration. Therefore, for irradiations above 10 kGy, septum material selection and control of experimental geometry are critical, as their effects can outweigh the intended experimental variable.

Gamma irradiation of aerated water in contact with AISI 441, Inconel 718, Inconel X-750, and Zircaloy-2 (**Chapter 5.2**) showed that steady-state concentration of H_2O_2 is influenced by the composition of the alloys. Control experiments with H_2O_2 alone showed only minimal H_2O_2 loss, indicating low reactivity of H_2O_2 toward these alloys in normal conditions. Thus, the irradiated-system trends are dominated by radiation-induced processes: AISI 441 most strongly suppresses H_2O_2, while Zircaloy-2 is neutral or slightly enhancing. XPS revealed nanometre-thick oxide films on all the alloys before and after irradiation or H_2O_2 exposure, with only minor, inconclusive changes. EIS supported these findings by quantifying ultrathin oxide layers. ICP-MS detected only trace alloy-element release, with higher Fe conent in solutions irradiated with AISI 441. Consequently, the lower H_2O_2 levels, especially with AISI 441, are not due to growth of a substantially thicker oxide scale but are more plausibly caused by reactions of H_2O_2 with dissolved Fe released during irradiation.

In situ electrochemical tests on 316L under intermittent γ-irradiation (**Chapter 5.3**) showed an immediate oxidative current response linked to radiolytic reactive species. At 0.25–0.57 Gy/s and fixed potential (OCP before irradiation), the response amplitude scaled with dose rate and was reduced by 40–75% upon adding 0.2 M tert-butanol as HO• scavenger. This response can be attributed to transient hydroxyl radical-driven modification of the electrode surface that enhances reactivity. When irradiation stops, HO• decays rapidly, the passive film returns to its original state and the current returns toward baseline. Scavenging HO• also increased the steady-state concentration of H_2O_2 by hindering HO• from directly reacting with hydrogen peroxide. During 12 min of effective irradiation, H_2O_2 content increased by up to 57% with tert-butanol versus 7% without. Consequently, OCP drifted to more positive values by more than 30 mV in tert-butanol solutions The OCP shift was accurately reproduced by addition of H_2O_2, proving the dominant role of H_2O_2 in affecting the OCP of the systems over longer time.

EIS before/after irradiation and H_2O_2 addition indicated only limited, similar persistent film modifications attributable to H_2O_2, while HO•-related surface changes were largely reversible or negligible.

To conclude, the research conducted in the framework of this thesis corroborates the existence of significant discrepancies in the behaviour of solid/liquid systems exposed to chemically added H_2O_2 and γ irradiation. The irradiation of different alloys revealed substantial differences in the H_2O_2 concentration of aqueous solutions in contact with the investigated materials, effects that were observed only under γ irradiation. Furthermore, electrochemical investigations under intermittent irradiation, while confirming H_2O_2 as the radiolytically-produced oxidant with the greatest long-term impact on the surface of AISI 316L, demonstrated a clear correlation between hydroxyl radicals and surface reactivity under irradiation, perhaps arising from transient surface modifications persistent only under γ irradiation. Lastly, experiments involving the irradiation of water-filled vials sealed by different septa also reported how polymers exhibit completely different behaviour when exposed to prolonged γ irradiation compared with prolonged contact with H_2O_2 solutions, with significant consequences for the chemical environment of the experiment. Overall, despite H_2O_2 being identified as the radiolysis product with the most significant long-term influence on the surface characteristics of the investigated samples, short-lived radiolytic species may play an important role in determining surface reactivity and shaping the overall experimental environment.

Acknowledgements

My sincere gratitude to my supervisor, Professor Mats Jonsson. Despite the distance and your commitments, you always found time for thoughtful scientific discussions. Thank you for your kindness and belief in my work. I like to remember what you called the “ketchup effect”: for a long time, it seems that nothing is happening, and then, all at once, everything starts flowing. Whenever I felt discouraged, it reminded me that sometimes science behaves exactly like a stubborn ketchup bottle, and that perseverance eventually leads to breakthroughs.

Thank you to my co-supervisor, Professor Christian Ekberg, for your trust and for giving me the freedom to explore my own path. Your delightfully enigmatic comments often took time to appreciate, but they never failed to inspire new ideas.

Thank you, Professor Teodora Vollmer, for being there to listen, encourage me and for reminding me to rest as well.

A special thank you to Dr. Alberto Visibile. Working with you laid the foundation for my understanding of electrochemistry, and our aperitivi never failed to restore my curiosity and lift my mood. Your friendship has a value to me that goes far beyond what words can convey.

Gabriele, Alice, Matthieu, Reddy, Valentina. Thank you for welcoming me and making me feel at home. You played a significant role in my decision to pursue a PhD in Sweden.

Special mention to Georgios, Martin, Doğaç, Andrea, Yiğit, Fredrik, and Thomas. Thank you for the good work, the laughter, your support and your friendship. Here’s to many more dinners and laughs together.

To the rest of the KK/IMÅ people, thank you for making our division a great place to work and for enduring my passionate explanations and probably unsolicited lectures on Italian food. You deserve to eat your “creamy bacon (fake) carbonara” in peace now.

Fredrik, your kindness and meticulous approach made working with you incredibly easy. You have been a wonderful travel companion, and the trip to Korea would not have been the same without you.

Mamma, Papà, and Marco, throughout this journey you surrounded me with unwavering love, care, and encouragement, and for that I will always be grateful.

My deepest love and gratitude go to my wonderful wife, Camilla, for standing by me through every challenge, celebrating my achievements even when I could not see them myself, and giving me confidence when I doubted my abilities. Your love and unwavering support have been the foundation of this journey.

To our son, Ingemar, thank you for being the light of our lives. Your smiles and laugher have given meaning to every success and perspective to every setback. Together with your mom, you are my greatest source of happiness and the strength behind all that I do.

This project was entirely funded by the Swedish Centre for Nuclear Technology (SKC).

References

[1] World Nuclear Association, “World Energy Needs and Nuclear Power.” Accessed: Mar. 31, 2025. [Online]. Available: https://world-nuclear.org/information-library/current-and-future-generation/world-energy-needs-and-nuclear-power

[2] I. International Energy Agency, “Electricity 2025 – Analysis,” 2025. Accessed: Jul. 20, 2026. [Online]. Available: https://www.iea.org/reports/electricity-2025

[3] M. Aczel, S. Chamanara, M. Matin, A. Farsi, T. Marwala, and K. Madani, “The Environmental Cost of AI’s Energy Use: Carbon, Water and Land Footprints,” Jun. 2026, doi: 10.53328/INR26RMA002.

[4] I. International Atomic Energy Agency, “REFERENCE DATA SERIES Nuclear Power Reactors in the World,” 2025.

[5] Intergovernmental Panel on Climate Change, “IPCC Sixth Assessment Report,” 2022. [Online]. Available: https://www.ipcc.ch/assessment-report/ar6/

[6] SKGS, “The Swedish Industry’s demand for electricity up to 2035,” Jun. 2024. Accessed: Mar. 31, 2025. [Online]. Available: https://skgs.org/english/aktuellt/new-report-the-swedish-industrys-demand-for-electricity-up-to-2030/

[7] “Forsmark and Ringhals nuclear power plants aim for 80 years of operation of existing reactors - Vattenfall.” Accessed: Jul. 20, 2026. [Online]. Available: https://group.vattenfall.com/press-and-media/pressreleases/2024/forsmark-and-ringhals-nuclear-power-plants-aim-for-80-years-of-operation-of-existing-reactors/

[8] “Sweden - World Nuclear Outlook Report - World Nuclear Association.” Accessed: Jul. 30, 2026. [Online]. Available: https://world-nuclear.org/our-association/publications/world-nuclear-outlook-report/sweden---world-nuclear-outlook-report

[9] “Nuclear Power in Sweden - World Nuclear Association.” Accessed: Jul. 30, 2026. [Online]. Available: https://world-nuclear.org/information-library/country-profiles/countries-o-s/sweden

[10] “Sweden proposes steps to facilitate new nuclear projects - World Nuclear News.” Accessed: Jul. 30, 2026. [Online]. Available: https://www.world-nuclear-news.org/articles/sweden-proposes-steps-to-facilitate-new-nuclear-projects

[11] “Swedish government budgets for nuclear new-build - World Nuclear News.” Accessed: Jul. 30, 2026. [Online]. Available: https://www.world-nuclear-news.org/articles/swedish-government-budgets-for-nuclear-new-build

[12] G. S. Was, “Challenges to the use of ion irradiation for emulating reactor irradiation,” *J. Mater. Res.*, vol. 30, no. 9, pp. 1158–1182, Jan. 2015, doi: 10.1557/JMR.2015.73.

[13] F. Schmidt, P. Hosemann, R. O. Scarlat, D. K. Schreiber, J. R. Scully, and B. P. Uberuaga, “Effects of Radiation-Induced Defects on Corrosion,” *Annu. Rev. Mater.*

Res., vol. 51, no. Volume 51, 2021, pp. 293–328, Jul. 2021, doi: 10.1146/ANNUREV-MATSCI-080819-123403/CITE/REFWORKS.

[14] S. S. Raiman *et al.*, "A facility for studying irradiation accelerated corrosion in high temperature water," *Journal of Nuclear Materials*, vol. 451, no. 1–3, pp. 40–47, Aug. 2014, doi: 10.1016/J.JNUCMAT.2014.03.022.

[15] S. Raiman, P. Wang, and G. Was, "Irradiation Accelerated Corrosion of Stainless Steel and Ferritic-Martensitic Steel in Simulated Primary Water," in *Corrosion 2017*, New Orleans. Lousiana, 2017.

[16] Y. J. Kim, "Analysis of Oxide Film Formed on Type 304 Stainless Steel in 288°C Water Containing Oxygen, Hydrogen, and Hydrogen Peroxide," *Corrosion*, vol. 55, no. 1, pp. 81–88, Jan. 1999, doi: 10.5006/1.3283969.

[17] E. Toijer and M. Jonsson, "H2O2 and γ-radiation induced corrosion of 304L stainless steel in aqueous systems," *Radiation Physics and Chemistry*, vol. 159, pp. 159–165, Jun. 2019, doi: 10.1016/J.RADPHYSCHEM.2019.02.047.

[18] "PRIS Analytics." Accessed: Jul. 30, 2026. [Online]. Available: https://pris-stats.iaea.org/world-statistics

[19] "Power plants: Ringhals - Vattenfall." Accessed: Jul. 30, 2026. [Online]. Available: https://powerplants.vattenfall.com/ringhals/

[20] "Power plants: Forsmark - Vattenfall." Accessed: Jul. 30, 2026. [Online]. Available: https://powerplants.vattenfall.com/forsmark/

[21] "Oskarshamn 3." Accessed: Jul. 30, 2026. [Online]. Available: https://okg.se/en/oskarshamn-3/

[22] K. H. Neeb, "The radiochemistry of nuclear power plants with light water reactors," *The Radiochemistry of Nuclear Power Plants with Light Water Reactors*, pp. 1–740, 1997, doi: 10.1515/9783110812015.

[23] United States Nuclear Regulatory Commission, "Animated Images of Plants PWR and BWR." Accessed: Apr. 04, 2025. [Online]. Available: https://www.nrc.gov/reading-rm/basic-ref/students/multimedia/animated-images-plants-pwr-bwr.html

[24] J. W. T. . Spinks and R. J. . Woods, *An introduction to radiation chemistry*. John Wiley & Sons, 1990.

[25] S. Le Caër, "Water Radiolysis: Influence of Oxide Surfaces on H2 Production under Ionizing Radiation," *Water (Basel).*, vol. 3, no. 1, pp. 235–253, Feb. 2011, doi: 10.3390/w3010235.

[26] A. O. Allen, "Radiation chemistry of aqueous solutions," *Journal of Physical and Colloid Chemistry*, vol. 52, no. 3, pp. 479–490, 1948, doi: 10.1021/J150459A009/ASSET/J150459A009.FP.PNG_V03.

[27] F. Cattant, “The Underestimated Role of the Oxygen on RCS Components Failures,” 2017. [Online]. Available: www.antinternational.com

[28] C. C. Lin, “A review of corrosion product transport and radiation field buildup in boiling water reactors,” *Progress in Nuclear Energy*, vol. 51, no. 2, pp. 207–224, Mar. 2009, doi: 10.1016/J.PNUCENE.2008.05.005.

[29] A. Ferrer, F. Dacquait, B. J. P Gall, and G. Ranchoux, “Modelling of crud growth phenomena on PWR fuel rods under nucleate boiling conditions,” in *International Conference on Water Chemistry of Nuclear Reactor Chemistry*, 2012. [Online]. Available: https://cea.hal.science/cea-04475789v1

[30] H. He, Y. Liu, S. Wang, T. Zhang, X. Chai, and X. Liu, “Review on corrosion-related unidentified deposit of pressurized water reactors,” Sep. 01, 2025, *Elsevier Ltd*. doi: 10.1016/j.nucengdes.2025.114095.

[31] P. Atkins and J. De Paula, *Atkins- Physical Chemistry*, 10th ed. London: Oxford University Press, 2014.

[32] T. Rooth, M. Ullberg, E. Karlsson, and I. Persson, “Hydrogen Peroxide in BWRs: An Experimental Determination of The Actual Level,” in *Conference of Water Chemistry of Nuclear Reactor Systems, Vol. 2*, Bournemouth, UK, 1989, pp. 55–60.

[33] C. D. Bopp and O. Sisman, “RADIATION STABILITY OF PLASTICS AND ELASTOMERS (SUPPLEMENT TO ORNL-928),” Jul. 1953, doi: 10.2172/4412528.

[34] A. Charlesby, “Effect of High-energy Radiation on Long-chain Polymers,” *Nature 1953 171:4343*, vol. 171, no. 4343, pp. 167–167, 1953, doi: 10.1038/171167a0.

[35] A. A. Miller, “EFFECTS OF HIGH-ENERGY RADIATION ON POLYMERS,” *Ann. N. Y. Acad. Sci.*, vol. 82, no. 3, pp. 774–781, 1959, doi: 10.1111/J.1749-6632.1959.TB44957.X.

[36] A. J. . Swallow, *Radiation chemistry of organic compounds*. Pergamon Press, 1960. Accessed: Mar. 24, 2025. [Online]. Available: http://www.sciencedirect.com:5070/book/9780080092973/radiation-chemistry-of-organic-compounds

[37] D. J. T. Hill and A. K. Whittaker, “Radiation Chemistry of Polymers,” *Encyclopedia of Polymer Science and Technology*, pp. 1–58, Nov. 2016, doi: 10.1002/0471440264.PST488.PUB2.

[38] O. Saito, “On the Effect of High Energy Radiation to Polymers I. Cross-linking and Degradation,” *https://doi.org/10.1143/JPSJ.13.198*, vol. 13, no. 2, pp. 198–206, Dec. 2013, doi: 10.1143/JPSJ.13.198.

[39] S. V. Suraci and D. Fabiani, “Radiation-Induced Degradation in Polymeric Materials: Alterations in Physical–Chemical Properties and Their Effects on Electrical Performance of Insulation Systems,” *High Voltage*, vol. 11, no. 1, pp. 150–169, Feb. 2026, doi: 10.1049/HVE2.70071;PAGE:STRING:ARTICLE/CHAPTER.

[40] I. G. Von White, R. Tandon, L. M. Serna, M. C. Celina, and R. Bernstein, “An Overview of Basic Radiation Effects on Polymers and Glasses.,” Sep. 01, 2013.

[41] K. Lunkwitz, H. J. Brink, D. Handte, and A. Ferse, “The radiation degradation of polytetrafluoroethylene resulting in low-molecular and functionalized perfluorinated compounds,” *International Journal of Radiation Applications and Instrumentation. Part C. Radiation Physics and Chemistry*, vol. 33, no. 6, pp. 523–532, Jan. 1989, doi: 10.1016/1359-0197(89)90309-3.

[42] K. Lunkwitz, U. Lappan, and U. Scheler, “Modification of perfluorinated polymers by high-energy irradiation,” *J. Fluor. Chem.*, vol. 125, no. 6, pp. 863–873, Jun. 2004, doi: 10.1016/J.JFLUCHEM.2004.01.020.

[43] A. Charlesby, “Changes in silicone polymeric fluids due to high-energy radiation,” *Proceedings of the Royal Society of London. A. Mathematical and Physical Sciences*, vol. 230, no. 1180, pp. 120–135, Jun. 1955, doi: 10.1098/RSPA.1955.0116.

[44] A. A. Miller, “Radiation Chemistry of Polydimethylsiloxane. I. Crosslinking and Gas Yields,” *J. Am. Chem. Soc.*, vol. 82, no. 14, pp. 3519–3523, Jun. 1960, doi: 10.1021/JA01499A011/ASSET/JA01499A011.FP.PNG_V03.

[45] C. G. Delides, “The protective effect of phenyl group on the crosslinking of irradiated dimethyldiphenylsiloxane,” *Radiation Physics and Chemistry (1977)*, vol. 16, no. 5, pp. 345–352, Jan. 1980, doi: 10.1016/0146-5724(80)90228-9.

[46] J. F. Zack, E. L. Warrick, and G. Knoll, “Radiation Stability of Organosilicon Compounds.,” *J. Chem. Eng. Data*, vol. 6, no. 2, pp. 279–281, Apr. 1961, doi: 10.1021/JE60010A029.

[47] J. A. LaVerne, N. A. I. Tratnik, and A. Sasgen, “Gas production in the radiolysis of Poly(dimethysiloxanes),” *Radiation Physics and Chemistry*, vol. 142, pp. 50–53, Jan. 2018, doi: 10.1016/J.RADPHYSCHEM.2017.01.027.

[48] Pine Research, “Electrochemical Impedance Spectroscopy (EIS) Basics.” Accessed: Apr. 08, 2025. [Online]. Available: https://pineresearch.com/support-article/eis-basics/

[49] A. Visibile, L. Gagliani, E. Ahlberg, J.-E. Svensson, and J. Froitzheim, “An Alternative Method of Measuring Area Specific Resistance of Chromia Scales Using Electrochemical Impedance Spectroscopy,” *J. Electrochem. Soc.*, vol. 170, no. 3, p. 031505, Mar. 2023, doi: 10.1149/1945-7111/acc13e.

[50] P. H. Fang and W. S. Brower, “Dielectric Constant of Cr2O3 Crystals,” *Physical Review*, vol. 129, no. 4, p. 1561, Feb. 1963, doi: 10.1103/PhysRev.129.1561.

[51] J. Liu, J. Li, J. Wu, and J. Sun, “Structure and Dielectric Property of High-k ZrO2 Films Grown by Atomic Layer Deposition Using Tetrakis(Dimethylamido)Zirconium and Ozone,” *Nanoscale Res. Lett.*, vol. 14, no. 1, pp. 1–12, May 2019, doi: 10.1186/S11671-019-2989-8/FIGURES/11.

[52] GW Ceramics, “Electrical properties of zirconia, table.” Accessed: Apr. 08, 2025. [Online]. Available: https://gwceramics.com/materials/zirconia/

[53] FrancoCorradi SAS, “Proprietà Termo-Fisiche dei componenti di Zirconia, Table.” Accessed: Apr. 08, 2025. [Online]. Available: https://francocorradi.it/metalli-e-ceramiche/ceramiche-tecniche/componenti-di-zirconia/

[54] K. V. Rao and A. Smakula, “Dielectric Properties of Cobalt Oxide, Nickel Oxide, and Their Mixed Crystals,” *J. Appl. Phys.*, vol. 36, no. 6, pp. 2031–2038, Jun. 1965, doi: 10.1063/1.1714397.

[55] ASTM International, “Specification for Wrought Zirconium Alloy Seamless Tubes for Nuclear Reactor Fuel Cladding,” Apr. 01, 2022, *ASTM International, West Conshohocken, PA*. doi: 10.1520/B0811-13R22E01.

[56] ASTM International, “Specification for Precipitation-Hardening and Cold Worked Nickel Alloy Bars, Forgings, and Forging Stock for Moderate or High Temperature Service,” Dec. 01, 2023, *ASTM International, West Conshohocken, PA*. doi: 10.1520/B0637-23.

[57] ASTM International, “Specification for Nickel-Iron-Chromium-Silicon Alloys (UNS N08330 and N08332) Seamless Pipe and Tube,” Oct. 01, 2022, *ASTM International, West Conshohocken, PA*. doi: 10.1520/B0535-06R22.

[58] ASTM International, “Specification for Chromium and Chromium-Nickel Stainless Steel Plate, Sheet, and Strip for Pressure Vessels and for General Applications,” Oct. 15, 2024, *ASTM International, West Conshohocken, PA*. doi: 10.1520/A0240_A0240M-24A.

[59] Joseph. Magill, Gerda. Pfennig, Raymond. Dreher, and Zsolt. Sóti, *Karlsruher Nuklidkarte*. Nucleonica GmbH, 2015.

[60] “Ultraviolet absorption spectra of iodine, iodide ion and triiodide ion.” Accessed: Apr. 23, 2025. [Online]. Available: https://www.researchgate.net/publication/7884754_Ultraviolet_absorption_spectra_of_iodine_iodide_ion_and_triiodide_ion

[61] N. L. Hansson, “Oxidative dissolution of UO2 by α-radiolysis,” 2022, Accessed: Apr. 23, 2025. [Online]. Available: https://research.chalmers.se/en/publication/531458

[62] S. Hanawa *et al.*, “Determination of electrochemical corrosion potential along the JMTR in-pile loop-II: Validation of ECP electrodes and the extrapolation of measured ECP data,” *Nucl. Technol.*, vol. 183, no. 1, pp. 136–148, 2013, doi: 10.13182/NT13-A16998.

[63] E. S. A. Hegazy, T. Sasuga, M. Nishii, and T. Seguchi, “Irradiation effects on aromatic polymers: 1. Gas evolution by gamma irradiation,” *Polymer (Guildf).*, vol. 33, no. 14, pp. 2897–2903, Jan. 1992, doi: 10.1016/0032-3861(92)90074-7.

[64] R. L. Clough and S. W. Shalaby, *Irradiation of Polymers: Fundamentals and Technological Applications*, vol. 620. Journal of the American Chemical Society, 1996. Accessed: Feb. 27, 2025. [Online]. Available: https://pubs.acs.org/isbn/9780841233775

[65] B. Liu, Q. Liu, Y. Ao, P. Wang, W. Huang, and H. Chen, "Gamma irradiation-induced degradation of silicone encapsulation," *Mater. Today Commun.*, vol. 31, Jun. 2022, doi: 10.1016/j.mtcomm.2022.103476.

[66] B. Liu, W. Huang, Y. Y. Ao, P. C. Wang, Y. An, and H. B. Chen, "Dose rate effects of gamma irradiation on silicone foam," *Polym. Degrad. Stab.*, vol. 147, pp. 97–102, Jan. 2018, doi: 10.1016/j.polymdegradstab.2017.11.016.

[67] P. C. Wang, N. Yang, D. Liu, Z. M. Qin, Y. An, and H. B. Chen, "Coupling effects of gamma irradiation and absorbed moisture on silicone foam," *Mater. Des.*, vol. 195, Oct. 2020, doi: 10.1016/j.matdes.2020.108998.

[68] N. G. Schnautz and J. C. Thompson, "Volatile radiolysis products of polytetrafluoroethylene," *S.Afr.J.Chem*, vol. 46, pp. 23–25, 1993.

[69] R. E. Florin and L. A. Wall, "Gamma Irradiation of Fluorocarbon Polymers," *J. Res. Natl. Bur. Stand. A Phys. Chem.*, vol. 65A, no. 4, p. 375, Jul. 1961, doi: 10.6028/JRES.065A.038.

[70] K. Schierholz, U. Lappan, A. Petr, L. Dunsch, and K. Lunkwitz, "Temperature influence on the stability and chemical composition of electron beam-irradiated polytetrafluoroethylene," *J. Polym. Sci. B Polym. Phys.*, vol. 37, no. 17, pp. 2404–2411, Sep. 1999, doi: 10.1002/(SICI)1099-0488(19990901)37:17<2404::AID-POLB11>3.0.CO;2-4.

[71] D. M. Pinkerton and B. T. Sach, "The Effects of y-Radiation on The Gas Yields and Crystallinity of Polytetrafluoroethylene," *Aust. J. Chem.*, vol. 23, no. 10, pp. 1947–1961, 1970.

[72] S. Siegel and H. Hedgpeth, "Chemistry of irradiation induced polytetrafluoroethylene radicals: I. Re-examination of the EPR spectra," *J. Chem. Phys.*, vol. 46, no. 10, pp. 3904–3912, 1967, doi: 10.1063/1.1840462.

[73] S. A. Khatipov, E. M. Konova, and N. A. Artamonov, "Radiation-modified polytetrafluoroethylene: Structure and properties," *Russ. J. Gen. Chem.*, vol. 79, no. 9, pp. 2006–2015, Sep. 2009, doi: 10.1134/S1070363209090321/METRICS.

[74] T. Hoffmann, M. Heller, D. Jehnichen, T. Engelhardt, and D. Lehmann, "Influence of absorbing materials on the functionalization of poly(tetrafluoroethylene) during γ-irradiation," *J. Appl. Polym. Sci.*, vol. 130, no. 3, pp. 1787–1793, Nov. 2013, doi: 10.1002/app.39346.

[75] M. G. Ormerod and A. Charlesby, "The radiation chemistry of some polysiloxanes: An electron spin resonance study," *Polymer (Guildf).*, vol. 4, no. C, pp. 459–470, Jan. 1963, doi: 10.1016/0032-3861(63)90059-4.

[76] A. A. Miller, “Radiation Chemistry of Polydimethylsiloxane. I. Crosslinking and Gas Yields,” *J. Am. Chem. Soc.*, vol. 82, no. 14, pp. 3519–3523, Jun. 1960, doi: 10.1021/JA01499A011.

[77] H. Menhofer and H. Heusinger, “Radical formation in polydimethylsiloxanes and polydimethyldiphenylsiloxanes studied by the ESR spintrap technique,” *International Journal of Radiation Applications and Instrumentation. Part C. Radiation Physics and Chemistry*, vol. 29, no. 4, pp. 243–251, Jan. 1987, doi: 10.1016/1359-0197(87)90029-4.

[78] “Radiation protection in irradiated dimethylsiloxane polymers,” *Proc. R. Soc. Lond. A Math. Phys. Sci.*, vol. 273, no. 1352, pp. 117–132, Apr. 1963, doi: 10.1098/RSPA.1963.0078.

[79] H. A. Dewhurst and L. E. St. Pierre, “Radiation chemistry of hexamethyldisiloxane, a polydimethylsiloxane model,” *Journal of Physical Chemistry*, vol. 64, no. 8, pp. 1063–1065, 1960, doi: 10.1021/J100837A025.

[80] I. S. Lazurkin and G. P. Ushakov, “The effect of radiation on the properties of silicone rubber,” *The Soviet Journal of Atomic Energy*, vol. 4, no. 3, pp. 365–371, Mar. 1958, doi: 10.1007/BF01479779/METRICS.

[81] A. S. Palsule, S. J. Clarson, and C. W. Widenhouse, “Gamma irradiation of silicones,” *J. Inorg. Organomet. Polym. Mater.*, vol. 18, no. 2, pp. 207–221, Jun. 2008, doi: 10.1007/S10904-008-9205-0/FIGURES/16.

[82] D. Jeschke and H. A. Stuart, “Diffusion und Permeation von Gasea in Hochpolymeren in Abhängigkeit vom Kritallisationsgrad und von der Temperatur,” *Zeitschrift fur Naturforschung - Section A Journal of Physical Sciences*, vol. 16, no. 1, pp. 37–50, Jan. 1961, doi: 10.1515/ZNA-1961-0109/MACHINEREADABLECITATION/RIS.

[83] S. Ando, S. Sato, and K. Nagai, “Gas Permeation and Barrier Properties of Liquid Crystalline Polymers,” pp. 523–547, 2020, doi: 10.1007/978-3-030-43350-5_67.

[84] R. A. Pasternak, M. V. Christensen, and J. Heller, “Diffusion and Permeation of Oxygen, Nitrogen, Carbon Dioxide, and Nitrogen Dioxide through Polytetrafluoroethylene,” *Macromolecules*, vol. 3, no. 3, pp. 366–371, May 1970, doi: 10.1021/MA60015A020/ASSET/MA60015A020.FP.PNG_V03.

[85] T. C. Merkel, V. I. Bondar, K. Nagai, B. D. Freeman, and I. Pinnau, “Gas sorption, diffusion, and permeation in poly(dimethylsiloxane),” *J. Polym. Sci. B Polym. Phys.*, vol. 38, no. 3, pp. 415–434, Feb. 2000, doi: 10.1002/(SICI)1099-0488(20000201)38:3<415::AID-POLB8>3.0.CO;2-Z.

[86] A. Hiroki, S. M. Pimblott, and J. A. Laverne, “Hydrogen peroxide production in the radiolysis of water with high radical scavenger concentrations,” *Journal of Physical Chemistry A*, vol. 106, no. 40, pp. 9352–9358, Oct. 2002, doi: 10.1021/JP0207578.

[87] L. Gagliani, C. Ekberg, and M. Jonsson, “How septum materials affect H2O2 accumulation under gamma-irradiation of water in sealed vials: A comparative study on

polysiloxane rubber, PTFE, and aluminium," *Radiation Physics and Chemistry*, vol. 238, no. 3, p. 113196, Jan. 2026, doi: 10.1016/j.radphyschem.2025.113196.

[88] M. N. Kakaei, J. Neshati, and A. R. Rezaierod, "On the Extraction of the Effective Capacitance from Constant Phase Element Parameters," *Protection of Metals and Physical Chemistry of Surfaces 2018 54:3*, vol. 54, no. 3, pp. 548–556, Jun. 2018, doi: 10.1134/S2070205118030280.

[89] B. Hirschorn, M. E. Orazem, B. Tribollet, V. Vivier, I. Frateur, and M. Musiani, "Determination of effective capacitance and film thickness from constant-phase-element parameters," *Electrochim. Acta*, vol. 55, no. 21, pp. 6218–6227, Aug. 2010, doi: 10.1016/J.ELECTACTA.2009.10.065.

[90] S. M. Gateman, O. Gharbi, H. Gomes De Melo, K. Ngo, M. Turmine, and V. Vivier, "On the use of a constant phase element (CPE) in electrochemistry," 2022, doi: 10.1016/j.coelec.2022.101133.

[91] M. E. . Orazem and Bernard. Tribollet, *Electrochemical impedance spectroscopy*, 2nd edition. John Wiley & Sons, Inc., 2017.

[92] W. J. Gray and G. L. McVay, "Nitric acid formation during gamma irradiation of air/water mixtures," *Radiat. Eff.*, vol. 89, no. 3–4, pp. 257–262, Jan. 1985, doi: 10.1080/00337578508222509.

[93] L. Wu, Y. Beauregard, Z. Qin, S. Rohani, and D. W. Shoesmith, "A model for the influence of steel corrosion products on nuclear fuel corrosion under permanent disposal conditions," 2012, doi: 10.1016/j.corsci.2012.04.027.

[94] C. F. Baes 1924-, "The hydrolysis of cations / Charles F. Baes, jr., Robert E. Mesmer.," 1976, Accessed: Jul. 28, 2026. [Online]. Available: https://openurl.ebsco.com/contentitem/cat09075a:clpc.oai.edge.chalmers.folio.ebsco.com.fs00001000.f3de9eb1.7880.4bd0.8adf.93a0d2e360bd?sid=ebsco:plink:crawler&id=ebsco:cat09075a:clpc.oai.edge.chalmers.folio.ebsco.com.fs00001000.f3de9eb1.7880.4bd0.8adf.93a0d2e360bd&crl=c

[95] T. E. Graedel and C. Leygraf, "Corrosion Mechanisms for Nickel Exposed to the Atmosphere," *J. Electrochem. Soc.*, vol. 147, no. 3, p. 1010, Mar. 2000, doi: 10.1149/1.1393305/PDF.

[96] R. Karimihaghighi and M. Naghizadeh, "Effect of alloying elements on aqueous corrosion of nickel-based alloys at high temperatures: A review," *Materials and Corrosion*, vol. 74, no. 8, pp. 1246–1255, Aug. 2023, doi: 10.1002/MACO.202213705;WGROUP:STRING:PUBLICATION.

[97] J. Van Sijl, N. L. Allan, G. R. Davies, and W. Van Westrenen, "Solvation of Ti(iv) in aqueous solution under ambient and supercritical conditions," *Physical Chemistry Chemical Physics*, vol. 13, no. 16, pp. 7371–7377, Apr. 2011, doi: 10.1039/C0CP01637C.

[98] M. Filella and P. M. May, “The aqueous solution thermodynamics of niobium under conditions of environmental and biological interest,” *Applied Geochemistry*, vol. 122, p. 104729, Nov. 2020, doi: 10.1016/J.APGEOCHEM.2020.104729.

[99] G. V. Buxton, C. L. Greenstock, W. P. Helman, and A. B. Ross, “Critical Review of rate constants for reactions of hydrated electrons, hydrogen atoms and hydroxyl radicals (·OH/·O− in Aqueous Solution,” *J. Phys. Chem. Ref. Data*, vol. 17, no. 2, pp. 513–886, Apr. 1988, doi: 10.1063/1.555805.

[100] M. Wang, S. Perrin, C. Corbel, and D. Féron, “Electrochemical behaviour of 316L stainless steel exposed to representative chemistry in pressurised water reactors under proton radiation,” *Journal of Electroanalytical Chemistry*, vol. 737, pp. 141–149, Jan. 2015, doi: 10.1016/J.JELECHEM.2014.10.015.

[101] C. M. Lousada, A. J. Johansson, T. Brinck, and M. Jonsson, “Mechanism of H2O2 Decomposition on Transition Metal Oxide Surfaces,” *JOURNAL OF PHYSICAL CHEMISTRY C*, vol. 116, no. 17, pp. 9533–9543, May 2012, doi: 10.1021/JP300255H.

[102] V. L. Orkin, S. N. Kozlov, G. A. Poskrebyshev, and M. J. Kurylo, “Rate Constant for the Reaction of OH with H 2 between 200 and 480 K †,” 2006, doi: 10.1021/jp057035b.

[103] A. O. Allen, C. J. Hochanadel, J. A. Ghormley, and T. W. Davis, “Decomposition of water and aqueous solutions under mixed fast neutron and gamma radiation,” *Journal of Physical Chemistry*, vol. 56, no. 5, pp. 575–586, 1952, doi: 10.1021/J150497A007/ASSET/J150497A007.FP.PNG_V03.

[104] M. C. Biesinger, B. P. Payne, L. W. M. Lau, A. Gerson, and R. S. C. Smart, “X-ray photoelectron spectroscopic chemical state quantification of mixed nickel metal, oxide and hydroxide systems,” *Surface and Interface Analysis*, vol. 41, no. 4, pp. 324–332, Apr. 2009, doi: 10.1002/SIA.3026.

[105] M. C. Biesinger, B. P. Payne, A. P. Grosvenor, L. W. M. Lau, A. R. Gerson, and R. S. C. Smart, “Resolving surface chemical states in XPS analysis of first row transition metals, oxides and hydroxides: Cr, Mn, Fe, Co and Ni,” *Appl. Surf. Sci.*, vol. 257, no. 7, pp. 2717–2730, Jan. 2011, doi: 10.1016/J.APSUSC.2010.10.051.

[106] C. Morant, J. M. Sanz, L. Galán, L. Soriano, and F. Rueda, “An XPS study of the interaction of oxygen with zirconium,” *Surf. Sci.*, vol. 218, no. 2–3, pp. 331–345, Aug. 1989, doi: 10.1016/0039-6028(89)90156-8.

Appendix A – Surface Investigation Techniques

Scanning Electron Microscopy

The surface morphology and composition of the samples were investigated at the Chalmers Materials Analysis Laboratory (CMAL) by means of scanning electron microscopy (SEM) using a FEI Quanta environmental scanning electron microscope (ESEM). Both secondary electron (SE) and backscattered electron (BSE) imaging modes were employed to examine topographical features and compositional contrast, respectively. Complementary energy-dispersive X-ray spectroscopy (EDS) analyses were conducted to evaluate the elemental composition and confirm the homogeneity of the investigated samples.

X-ray Photoelectron Spectroscopy

XPS analysis of the samples was performed at the Royal Technological University, KTH in Stockholm, by a fellow PhD candidate, Fredrik Petersson. The instrument used was a Kratos Axis Supra+, equipped with a monochromatic Al K(alpha) X-ray source at 1.486.6 eV. The investigated spot area was 700 x 300 μm. X-ray Power was set at 5 mA, 15 kV, 75 W for the collection of wide spectra and 15 mA, 15 kV, 225 W for high-resolution core-level spectra. Charge neutralisation was used with the electron flood gun within the spectrometer. All spectra have been charge corrected to the main line of carbon 1s, which was referenced to 284.8 eV. Backgrounds were fit using the Shirley background. Metallic peaks were fit using asymmetric peak shapes, oxides/hydroxides were fit using 70% Gaussian, 30% Lorentzian peak shapes. Peak fitting was based on the instrument database and the following publications for Ni[104], Fe, Ni and Cr[105], and Zr[106].

Appendix B – Solubilised Elements Investigation

Inductively Coupled Plasma Mass Spectroscopy

For the identification of ions in solution, concentrations were determined using an Inductively Coupled Plasma Mass Spectroscopy (ICP-MS) setup (Thermo Scientific®, iCAP Q). The sample solutions were diluted in a 1:2 ratio with 0.5 M HNO_3 (Suprapur, Merck®) containing 2 ppb of Sc-45 and Y-89 as internal standards (diluted from 10 ppm certified standard solutions, CPAchem®). All the measurements were performed in triplicate, in standard mode. Dr. Mustapha Gida Saleh and Dr. Stellan Holgersson provided assistance with the ICP-MS analysis.